NANOSTRUCTURED OXIDES THERMOELECTRIC MATERIALS AND ENERGY HARVESTING DEVICES FOR CIVIL INFRASTRUCTURE APPLICATIONS

by

Yining Feng

A Dissertation

Submitted to the Faculty of Purdue University

In Partial Fulfillment of the Requirements for the degree of

Doctor of Philosophy

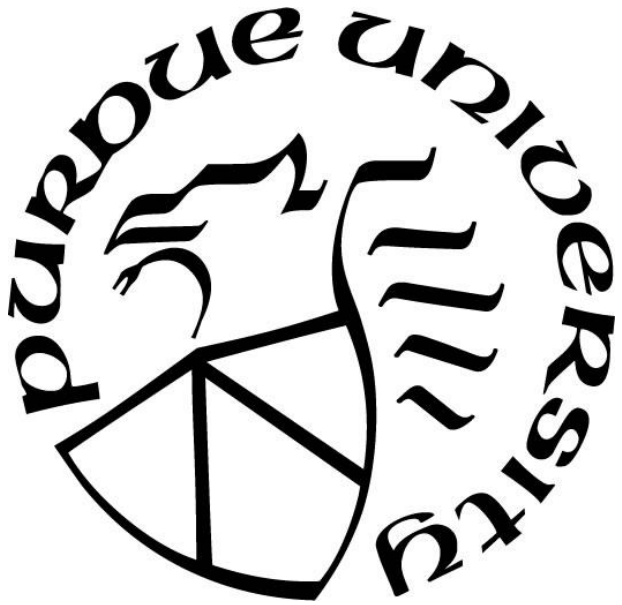

Lyles School of Civil Engineering

West Lafayette, Indiana

December 2020

THE PURDUE UNIVERSITY GRADUATE SCHOOL
STATEMENT OF COMMITTEE APPROVAL

Dr. Na (Luna) Lu, Chair

Lyles School of Civil Engineering

Dr. Mark Lundstrom

School of Electrical and Computer Engineering

Dr. Matthew Lynall

Krannert School of Management

Dr. Alexander Wei

Department of Chemistry

Approved by:

Dr. Dulcy M. Abraham

This dissertation is dedicated to my parents for their unconditional love and support.

ACKNOWLEDGMENTS

I am deeply grateful for many people who have supported and inspired me along this journey. First and foremost, I would like to thank my advisor, Prof. Na Lu, who is not only my role model, but also helped me to discover my own potentials. I really appreciate her support and trust for me as a researcher without any background in this field. She has been the most impactful mentor throughout my Ph.D. program. In addition, I highly appreciate the advice and support from my other Ph.D. committee members, including Prof. Mark Lundstrom, Prof. Matthew Lynall, and Prof. Alexander Wei. I benefited a lot from their guidance of my research and encouragement for the future career path.

Over the past five years, I was fortunate to work with many brilliant researchers at Purdue University and Argonne National Lab. I would like to especially thank their friendship and assistance of all my colleagues in the Luna Group. Also, I am grateful for the funding support from NSF to make the research move forward.

Finally, I would like to express my deep gratitude and appreciation to my parents, who continuous support and encourage me throughout my Ph.D. study.

TABLE OF CONTENTS

LIST OF TABLES

LIST OF FIGURES

ABSTRACT

Thermoelectric generators (TEG) are solid-state devices that can convert thermal energy directly into electricity through the Seebeck phenomenon. Over 2.5 quadrillion BTU/year of energy generated in the US is wasted as a form of heat, which can be reclaimed as electricity using conformal TEG (cTEG) to power electronic devices, such as IoT sensors and other microelectronics. However, the potential impact of TE technology for power generation is hindered by the challenges at both materials and device levels, including toxic materials and manufacturing process. This research aims to explore the possibility of using non-toxic and earth-abundant oxide-based TEG as energy sources for powering IoT sensors and their related applications in civil infrastructure.

The use of nanostructured oxides in TE applications has attracted much interest due to their high performance and long-term stability at elevated temperatures. In particular, $CuAlO_2$ and $PdBi_2O_4$ show great potential for high performance p-type TE materials due to their high thermal stability, simple stoichiometry, and non-toxicity. In this study, the impact of small nanostructure and dopants on the TE properties of these oxides are systematically investigated. Advanced characterization techniques are used to examine the structure-process-property relationship of as-synthesized materials and their related TE performance. $CuAlO_2$ and $PdBi_2O_4$ show high Seebeck coefficient and low thermal conductivity, which are desirable as TE materials. The flat band structure for these materials leads to high Seebeck coefficient due to large density of state effective mass. Phonon scattering contributes to low thermal conductivity for these materials. However, it is necessary to increase their electrical conductivity to achieve high TE efficiency. To better analyze the electrical and thermal properties, a generalized TE quality factor (b-factor) was used to compute the optimized carrier concentration and fermi level for $CuAlO_2$ and $PdBi_2O_4$ to achieve optimum power factor. Fe has been used in this study as an effective dopant to increase electrical property while reduce thermal conductivity of $CuAlO_2$ based on previous literatures. The highest zT value 1.2×10^{-2} was achieved for $CuAl_{0.8}Fe_{0.2}O_2$ at 750K.

In addition, a scalable fabrication process for cTEG device was also developed in this research. To overcome current expensive and discrete device fabrication process, a novel roll-to-roll manufacturing method for cTEG was discussed in detail. The study has further explored the potential application of using cTEG to power IoT sensors in underground pipeline monitoring

system. A simulation work has carried out in this study to guide the experimental design and fabrication of cTEG with a goal of achieving electrical and thermal properties co-optimization. This research has also resulted in a prototype of cTEG using the proposed scalable manufacturing method for energy harvesting for civil infrastructure applications. The produced cTEG prototype with 4 pairs thermocouples in a size of 40×40 mm^2 reaches a power output of 2.02 μW at ΔT =50˚C with a load voltage is 32 mV. It can connect with a DC-DC booster to meet the voltage requirement for powering IoT sensors for underground pipeline monitoring system.

The knowledge gained from this research will advance the understanding of the relationship between structural, electrical, and thermal properties of oxides materials. Also, it explores a scalable cTEG fabrication method, which enables many exciting opportunities of using TE technology for powering IoT sensors in civil infrastructure system.

1. INTRODUCTION

1.1 Background and Motivations

There is an increasing need for clean and renewable energy to fulfill the world's high energy demand. Harvesting waste heat for electricity is one approach to improve sustainability, which can reduce greenhouse gas emissions. It is evident that thermoelectric (TE) technology is an important advancement in the renewable energy field. TE materials have the ability to directly convert heat into electricity for power generation via the Seebeck effect[1]–[3]. It can play a crucial role in renewable energy production since 60% of the energy produced worldwide is waste as the form of heat. Additionally, as a solid-state device, TE technology has many attractive features such as high reliability, environmental friendliness, and no moving parts. Currently, TE devices have been used as power generators in a remote environment (e.g., space) or autonomous sensors[4], [5]. Factories, homes, and even the human body can be used as heat sources for thermoelectric generator (TEG) devices as well. By converting waste heat into electricity, TEG devices can be used for broader applications such as electricity production in rural areas, enhancement of solar panels, energy recovery from the exhaust pipes of cars, and even medical applications[6]–[8]. In civil engineering, TEG devices can be used for providing reliable power source by absorbing waste heat from power plants[9], chemical factories, and monitoring underground piping system.

Despite recent advances in TE research, the potential impact of TE technology for power generations is limited. One of the biggest challenges standing in the way of TEG devices is using suitable materials, which are cost-effective, environmentally friendly, and earth-abundant. Also, the materials with high power factor, an indicator of a large voltage with high current will be generated using TEG devices. Current TE materials are toxic, rare-earth, expensive (e.g. Te and Se) elements, and their low power output. For instance, there are only three major TE material systems commercially available for from low to high-temperature regime including Bi_2Te_3 (300-500K)[10], PbTe (500-600K)[11], and SiGe (600-800K)[12]. Their applications, in particularly Te-based materials, are largely restricted by the toxicity, limited element resources, and material degradation at high temperatures[13], [14]. Since the 1950s, researchers are dedicated to working on the improvement of efficiency using TE materials, however, the cost and toxicity are not the major considerations. As a result, the heavy use of toxic, expensive, and rare earth elements

occurred in the TE community. And the efficiency of TE materials is still relatively low, which limits the applications for TE technology. Until the early 1990s, the researchers in this community re-examined the opportunities for TE technology from a performance standpoint. Two approaches were used for the next generations of TE material: one using bulk TE materials, and the other using low-dimensional materials systems[10]. Bi_2Te_3 is potential TE material used for low-temperature range. SiGe is another TE material for higher temperature range.

The TE materials showed high efficiency, however, the cost and toxicity became considerations for broader applications. Metal oxides, on the other hand, are promising candidates to circumvent these challenges due to their earth abundance, low cost, non-toxic, and high thermal stability[15]. More importantly, their electronic properties can be tuned from insulator behavior to metallic behavior by manipulating their crystal structures, chemical compositions, and doping concentrations[16]. These unique materials properties open an exciting opportunity to obtain high power output in metal oxides. In fact, for TE power generation applications, a material with a high power factor of materials is even more important than having high efficiency since most waste heat sources are free (e.g. waste heat from car exhaust, gas engine) and unlimited (e.g. solar radiations)[17]. To this end, the first part of this thesis is focused on examining the metal oxides potentials for TE power generation with an emphasis on materials with high power factor.

Another challenge limits TE technology is the device geometry and fabrication process. Conventional TEG devices are plate-like and rigid, and unable to fully exploit thermal gradients (ΔT) from curved or nonplanar surfaces, as most heat sources have non-planar surfaces or spatial restrictions. The current TE technology suffers from its rigid device structure, low efficiency, and high cost in both materials and device fabrication processes. Conventional production of TEG devices is a complicated fabrication process which involves many discrete steps and rigid substrates. There are six separate steps which start from high energy ball milling commercial ingot, then compression molding into nano-bulk materials using high temperature and pressure. High-temperature sintering is the next step to achieve high crystallinity, which will be followed by dicing and polishing. The nanobulk materials will then be saw-cutting and polishing into p- and n- legs, which will be then pressed on the ceramic substrates with evaporated metal contacts. This process is very cumbersome, time, and labor-intensive. As such, the cost of fabrication and package of TEG devices counts for more than 70% of the cost. Despite the numerous efforts and advancement in TE materials level, the inefficient device fabrication process has surprisingly not been well

addressed in the TE community. To this end, the second part of this thesis is focused on developing conformal TEG (cTEG) device on a roll-to-roll platform with high performance.

1.2 Objectives and Methodology

The goal of this thesis is to synthesize nanostructured oxides thermoelectric materials and prototype cTEG devices in a niche market in civil infrastructure for energy harvesting. To achieve this goal, four major research objectives are listed in detail below:

1) Investigate small nanostructure effect on TE materials

In this study, the nanosize effect on thermoelectric materials properties is investigated by synthesizing nanoparticles using solid state method. The performance of TE material is measured by power factor (PF) and figure of merit (zT), which depend on three parameters Seebeck coefficient, electrical conductivity, and thermal conductivity. To obtain high zT that we need TE material with high Seebeck coefficient, high electrical conductivity, and low thermal conductivity. However, these three parameters are interdepended as the change of carrier concentration. With the carrier concentration increases, the electrical and thermal conductivity increases but the Seebeck coefficient decreases. To overcome this, we need to control the grain size small enough that it is larger than the electron mean free path and smaller than phonon mean free path. This will scatter more phonons, which will reduce thermal conductivity without deteriorating electrical properties. For power generation applications, the TE materials with higher PF make more contributions. Thus, the effective doping mechanism is necessary to investigate for PF enhancement.

2) Discover cost and performance effective oxides TE materials

Most recently studies on oxides thermoelectric materials such as ZnO, In_2O_3, SnO_2, and $SrTiO_3$ are all used as n-type materials. Na_xCoO_2 and $Ca_3Co_4O_9$ are the potential p-type materials, which stoichiometry of the materials are relatively hard to control. Thus, a simple and stable structure of p-type oxides thermoelectric material is needed for using the TE device for energy harvesting. Two promising candidates for p-type oxides TE materials are $CuAlO_2$ and $PdBi_2O_4$. The nanocrystalline bulk materials were synthesized by the solid-state method pressed by cold pressing for measurement. Different annealing time for materials synthesis is conducted to get high purity of nanocrystalline samples. The high-resolution transmission electron microscopy (HRTEM) and X-ray diffraction (XRD) are used for nanostructure analyzed. Pellets are used for TE properties

measurement. Seebeck coefficient is measured by home-build Seebeck measurement. Electrical conductivity and carrier concentration are measured by using a four-point probe method by Hall equipment. Thermal conductivity is measured by Laser Flash (LFA 467).

3) Design TEG device geometry and structure on its power output

Another import parameter needs to consider for TE technology is the device geometry and structure design. Although the efficiency of the TE device is important, the power output of the TE device is more critical as the heat source is unlimited for specific applications. Thus, the power output indicates how much electricity can be used by converting waste heat. There are several parameters such as fill factor, leg thickness, and temperature difference have impacts on the power output of the TE device. In order to obtain maximum power output, the design to TE structure is important.

4) Prototype conformal TEG device based on a roll-to-roll platform

Nearly all TEG designs are based on the classic Peltier model, in which heat exchange across alternating pillars of p- and n-type semiconductors drives an electrical current in a serpentine fashion. Standard Peltier devices are plate-like and rigid, and unable to fully exploit thermal gradients (ΔT) from curved or nonplanar surfaces that decay rapidly with distance ($\sim 1/d2$ assuming free convection). The impact of conformal contact on thermoelectric efficiency is critical as most of the heat sources have a non-planar surface, therefore a conformal TE device will have direct contact with heat source resulting good thermal path. Additionally, we will use high insulating polymers (i.e. Kapton, PDMS) as the substrate and insulating materials fills between p-n legs to avoid thermal loss. This will provide high efficiency and good mechanical stability to conformal TE device during the temperature cycle and mechanical bending process. The number of p-n pairs will be determined by the required power output for specific applications. The length of p- and n- legs, and the width and thickness of contacts will be determined based on the expected power output, the temperature gradient, and materials thermoelectric performance for specific applications.

1.3 Thesis Structure

The thesis is organized as follows:

In Chapter 2, an extensive literature review includes fundamental of TE, oxides TE materials, TEG device design, and manufacturing process.

In Chapter 3, major experimental procedures of oxides TE nanomaterials are introduced in detail, which include material synthesis, structure characterization, and TE performance characterization. The nanopowders were made by solid-state method followed by cold-pressing that effectively controls the grain size of nanocrystalline bulk materials. Different synthesis conditions were conducted to assure accurate measurement of their TE properties by using both commercial and home-building systems. In addition, strategies about the enhancement of TE properties are discussed in detail. Such analysis is important to understand what the optimum concentration that maximized the TE properties of different materials. The theoretical work effectively guides experimental work.

In Chapter 4, TE device with optimum fill factor, leg thickness, and p-n pairs is design based on the desired power output at a certain temperature range. A novel roll-to-roll fabrication of cTEG device used for underground pipeline monitoring system in civil infrastructure is discussed. A prototype of the cTEG device will be developed at the end. The performance of cTEG device for power output and voltage will be discussed.

In Chapter 5, the summary of current work and plan for future work is included.

2. LITERATURE REVIEW

This chapter contains portions of a previously published manuscript: Y. Feng et al., "Metal oxides for thermoelectric power generation and beyond," Adv. Compos. Hybrid Mater., vol. 1, no. 1, pp. 114–126, Mar. 2018, doi: 10.1007/s42114-017-0011-4

2.1 Fundamental of Thermoelectric

The quality of materials for TE application is described by a dimensionless parameter ZT[18], which is defined as the following:

$$ZT = \frac{S^2\sigma}{\kappa}T \tag{2.1}$$

where *S* is the Seebeck coefficient, σ is the electrical conductivity, *k* is the thermal conductivity. In physics, *k* consists of the electronic part (k_e, due to carrier transport) and lattice part (k_{Ph}, due to phonon transport). The term $S^2\sigma$ is called the power factor (PF). A high PF indicates that a TE power generator can achieve a high power output.

This chapter contains portions of a previously published manuscript

Seebeck coefficient (*S*, in V/K) is an intrinsic materials property, which measures the thermoelectric voltage induced in response to a temperature difference across the material. *S* represents the energy difference between the averaged charge carrier energy versus Fermi energy. It can be expressed as the following:

$$S = (\frac{k_B}{-q})(\frac{E_c - E_F}{k_B T} + \frac{\Delta_n}{k_B T}) \tag{2.2}$$

where E_F is the Fermi level, which the dependence to the temperature (*T*) and the Boltzmann constant (k_B) are made explicit. For Semiconductors, the Seebeck value can be a negative (electron conduction) or positive value (hole conduction), therefore the absolute value is more important. For doped semiconductors, the relationship between the Seebeck coefficient and carrier concentration can be expressed as the following:

$$S = \frac{8\pi^2 {k_B}^2}{3eh^2} m^* T (\frac{\pi}{3n})^{2/3} \tag{2.3}$$

where k_B is the Boltzmann constant, e is the carrier charge, h is Planck's constant, m^* is the effective mass of the charger carrier, and n is the carrier concentration. As can be seen, the lower carrier concentration is desirable for materials to reach a high Seebeck coefficient.

Electrical conductivity (σ) describes the ease of a material conducting charge carrier transport, which is defined as:

$$\sigma = ne\mu \tag{2.4}$$

where n is the carrier concentration, e is the carrier charge, and μ is the mobility. To reach high electrical conductivity, a high carrier concentration is desirable, however, it often degenerates the Seebeck coefficient of materials as governed by equation [3]. Therefore, an optimized carrier concentration of TE materials is often found at 10^{19} -10^{21} cm^{-3}[19]. The electrical conductivity of an ideal TE materials is usually on the order of 10^3 (S/cm), however, the electrical conductivity of metal oxides is often lower, on the order of 10-10^2 (S/cm). Thus, the investigation of effective doping mechanism on improving electrical conductivity without degenerating Seebeck is crucial to enable their applications in TE power generation and related fields.

Thermal conductivity (k), on the other hand, is the parameter that describes how efficiently a material can conduct heat. In the case of semiconductors, the total thermal conductivity (κ_T) consists of contributions from both electron and phonon transport, defined as following:

$$\kappa_T = \kappa_e + \kappa_l \tag{2.5}$$

where κ_e and κ_l are, respectively, the electron and lattice thermal conductivity. κ_l is known as the most important mechanism for heat conduction in semiconductors at temperatures close to room temperature, which normally accounts for 90% contributions in wide bandgap materials.

For good TE materials, a typical value of thermal conductivity is $k_T < 2$ W/mK[20]. Low thermal conductivity can be seen intuitively as an important parameter to maintain a certain temperature gradient across the junctions, which is essential for reaching high ZT in a material system[21]. Otherwise, the temperature gradient would quickly turn into equilibrium and cancels materials TE effect. Therefore, recent efforts in TE materials research have been heavily focused on reducing thermal conductivity to achieve high ZT using various strategies, such as nano-structuring, phonon rattling, and band structuring as reported in previous studies[22]–[24]. To this end, most previous review articles focus on examining various mechanisms to achieve low thermal

conductivity of materials. Very few literatures have discussed mechanisms to reach high power output of TE materials[25], and none of them focused on metal oxides.

In this study, we have systematically examined effective strategies to achieve high power output for potential applications in TE power generation. Much attention is paid to examining the effective dopants of various metal oxides to achieve high electrical conductivity without degrading Seebeck value or vice versa. As such, this review article will pave the road to the development of cost-effective, earth-abundant, and high-performance metal oxides for TE power generation and other thermal-electrical related applications.

2.2 Oxides Thermoelectric Materials

(copyright: This work is part of the publication)

There is a promising opportunity for metal oxides used as TE materials because of their non-toxicity, cost-effective, and high thermal stability compared to conventional TE materials[26]. Also, by altering their crystal structures and chemical compositions, electronic properties can be manipulated from insulator to metallic conductor behavior, which leads to a higher power factor[27]. Waste heat sources are often free and unlimited, so materials with high power factor are more important than the figure of merit for many TE power generation applications[28]. The following sections review the TE properties of the most common n- and p-type of metal oxides materials.

2.2.1 ZnO-based

The direct band gap of Zinc oxide (ZnO) is reported as 3.37 eV, which also shows large exciton binding energy of 60 meV[29]. It is a promising candidate for n-type TE material used in high-temperature energy harvesting[30], [31]. The study showed the PF of bulk ZnO to be about 0.75×10^{-4} W/mK^2 at carrier concentration ($n\sim10^{-17}$ cm^{-3}) at room temperature. The high PF can be attributed to the high crystal quality, which resulted in a favorable Seebeck coefficient (~478 µV/K)[32].

Although pure ZnO already has high Seebeck coefficient, significant enhancement of TE power factor and Seebeck coefficient is reported with Ga[33] and In-Al[34] doping. As shown in Figure 2.1, the maximum power factor value of 12.5×10^{-4} W/mK^2 at 1273 K observed in

$Zn_{0.985}Ga_{0.015}O$ yields zT_{max} of 0.25. Sean *et al*[34] reported that $(ZnO)Al_{0.03}In_{0.02}$ exhibited the best TE properties with a PF of 22.1×10^{-4} W/mK^2 at 975 K. From this study, an electrical conductivity of 5.88×10^2 S/cm and Seebeck coefficient of −220 μV/K has been reported. The PF is three times greater than that of the film without In dopants.

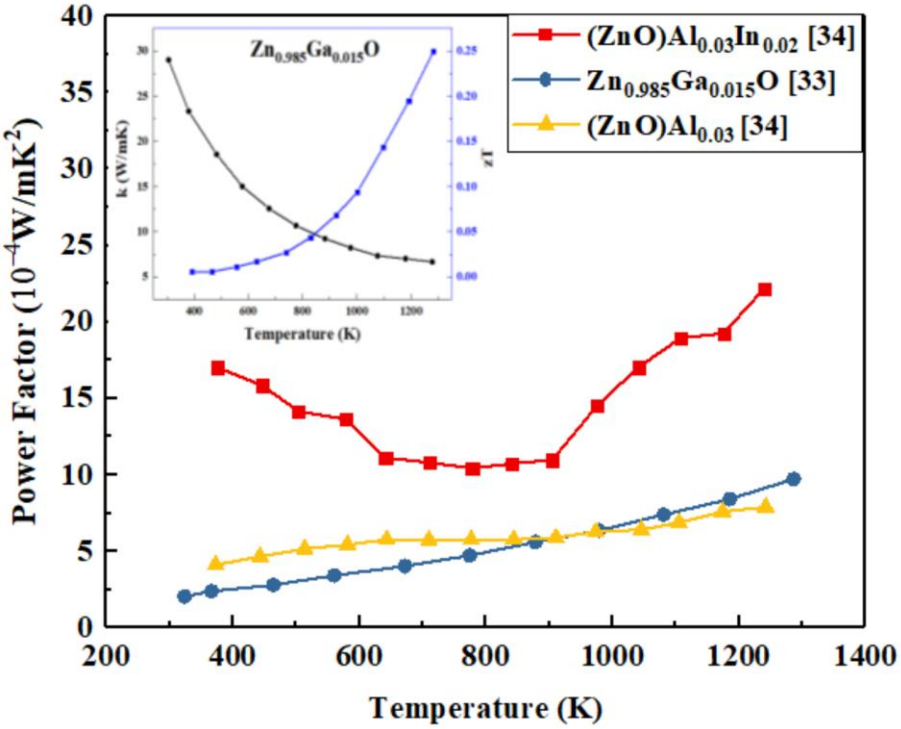

Figure 2.1 Temperature dependence of TE properties of ZnO

P-type doping of ZnO has been found to be very difficult. Ideally, group-I (Li and Na), group V (N, P, As, Sb and Bi), and group IB (Cu and Ag) elements could be p-type dopants. However, it is still very challenging due to the stability and reliability of p-type ZnO[35].

2.2.2 SnO_2-based

Tin Oxide (SnO_2) is a wide band gap (3.6eV) semiconductor that crystallizes in a rutile-type structure[36]. Due to its electrical and optical properties, SnO_2 and impurity-doped SnO_2 are mainly used as an electrode for dye-sensitized solar cell[36], electrochromic devices[37], a catalyst in chemical reactions[38], a varistor[39], and gas sensor[40].

Rubenis *et al.*[41] reported that the TE properties of $Sn_{1-x}Sb_xO_2$ (x=0, 0.01, 0.03, 0.05) synthesized by spark plasma sintering and subsequently air-annealing at 1173K. The addition of

Sb_2O_5 increased the carrier concentration of SnO_2. Thus, the Seebeck coefficient decreased but the electrical conductivity increased up to a maximum of 5.5 times at Sb doping level of x=0.03. The $Sn_{0.99}Sb_{0.01}O_2$ sample has the highest PF value of 4.5×10^{-4} W/mK^2 at 1073 K.

Figure 2.2 shows that $Sn_{0.94}Sb_{0.03}Zn_{0.03}O_2$ reaches the maximum PF of 2.13×10^{-4} W/mK^2 at 1060 K, which is 126% higher than that of the undoped sample. The electrical conductivity increases is due to the carrier concentration caused by an increase in Sb-doping and density of Zn-doping[42]. Moreover, Bi-doped $Sn_{0.97}Sb_{0.01}Zn_{0.01}Bi_{0.01}O_2$ sample has reached the maximum PF of 4.8×10^{-4} W/mK^2 at 1060 K. Yanagiya *et al.*[43] reported that Bi increased electrical conductivity by increasing the number of free electron in SnO_2, where Bi behaves as a donor. Also, the addition CuO of Sb-doped SnO_2 increased the PF at high temperature (T >1000 K). The substitution of Cu for Sn decreased carrier concentration because Cu is divalent but Sn is quadrivalent. As a result, the Seebeck coefficient increased. Also, the addition of the CuO has significantly improved the relative density of SnO_2 ceramics[44]. As such, the electrical conductivity increased with the increased carrier mobility. The Cu and Sb co-doped $Sn_{0.98}Cu_{0.01}Sb_{0.01}O_2$ reached the highest PF value of 7×10^{-4} W/mK^2 at 1073 K. However, Ti and Sb co-doped $Sn_{1-x-y}Ti_ySb_xO_2$ samples had lower PF values due to the electrical conductivity decreases with adding more TiO_2. Because TiO_2 dissolved in SnO_2 that caused the reduction of the mobility, resulting in a decrease of the electrical conductivity[45].

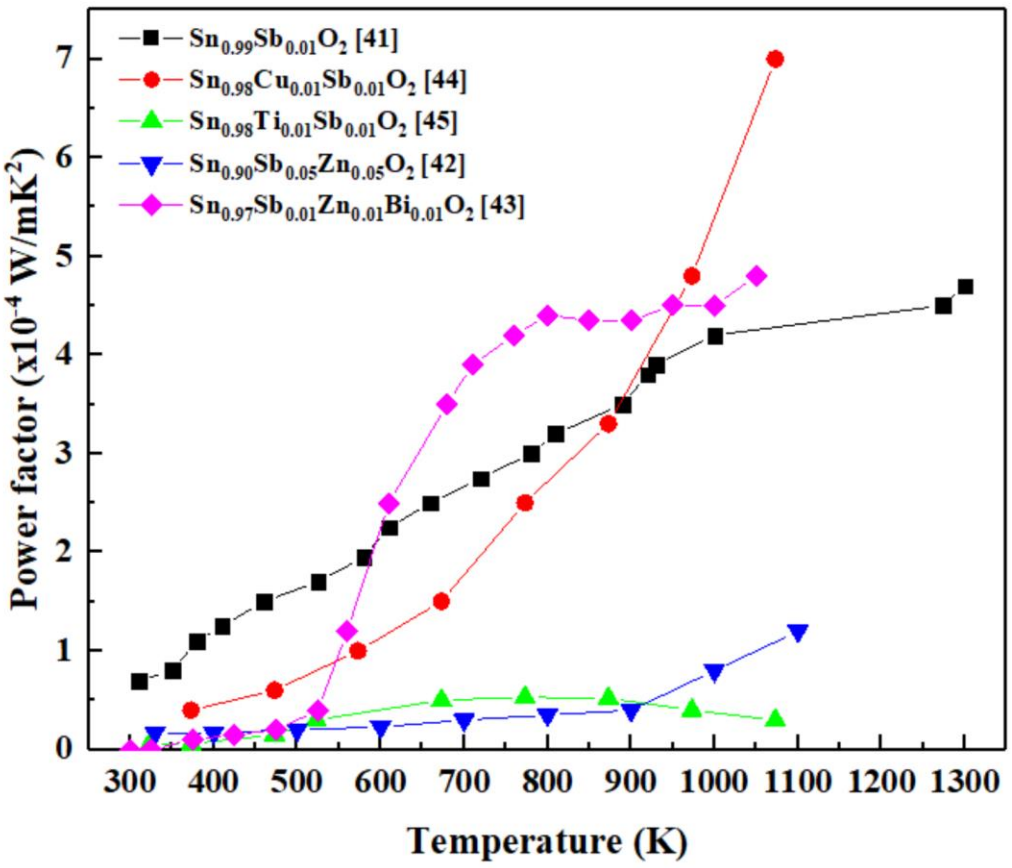

Figure 2.2 Power factor values of doped SnO_2 with various dopants as a function of temperature.

2.2.3 In_2O_3-based

Indium oxide (In_2O_3) is a semiconductor with band gap of 3.6 eV[46], which has recently gained interest as a promising candidate for high-temperature TE applications due to its high stability at air. It has been shown that electrical properties of In_2O_3 can be drastically changed by doping with Sn[47], Mo[48], Zr[49], Ti[50], and W[51].

Figure 2.3 shows that $In_{1.92}(ZnCe)_{0.08}O_3$ nanostructured ceramic exhibits the highest PF of 8.36×10^{-4} W/mK^2 at 1050 K[52]. This is due to the influence of nanostructuring and point defects on TE properties of In_2O_3 system. Point defect hinders the atomic-scale scattering and improves the carrier concentration thereby increasing PF. Utilizing spark plasma sintering process, co-doped polycrystalline In_2O_3 ceramics were fabricated by Liu *et al.*[53] They have achieved high electrical conductivity and Seebeck coefficient, which resulted in PF of 4.53×10^{-4} W/mK^2 at 1070 K for $In_{1.96}Co_{0.04}O_3$. Later, Liu *et al.*[54] prepared single-element Ga-doped In_2O_3 ceramics by spark

plasma sintering to explore their TE properties at high temperatures. The slight change in Seebeck coefficient and a significant enhancement of electrical conductivity (~ 400 S/cm) at 973 K were caused by an increase of carrier concentration through doping Ga, which achieved highest PF of 9.6×10^{-4} W/mK^2 in $In_{1.90}Ga_{0.10}O_3$ at 973 K.

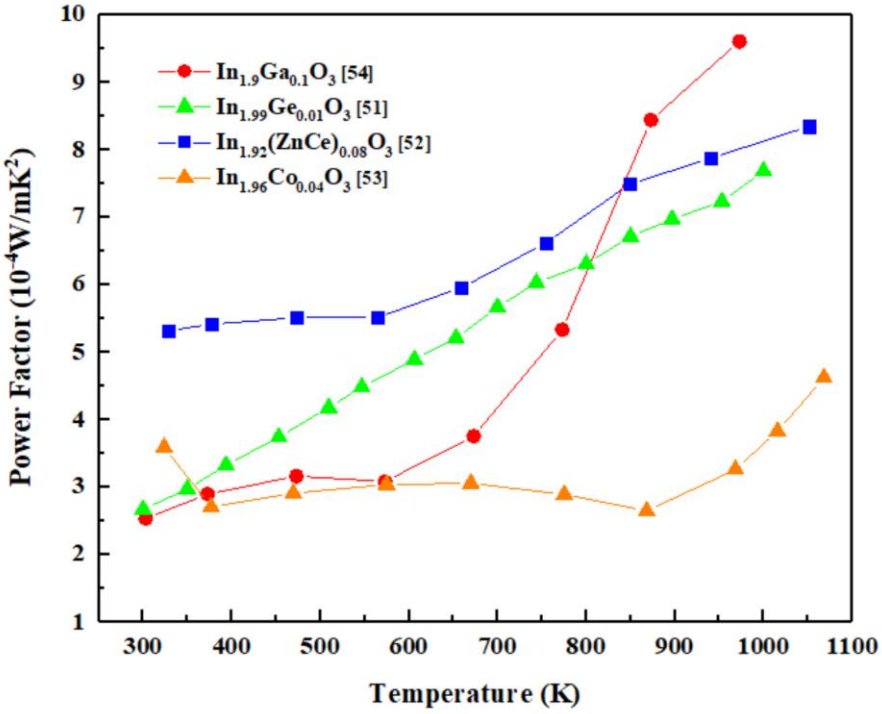

Figure 2.3 Power factor values of doped In_2O_3 with various dopants as a function of temperature.

2.2.4 $SrTiO_3$

Strontium titanate ($SrTiO_3$)-based perovskite oxide materials have shown potential applications as n-type TE materials at low temperature[55]. Nag *et al.* reported that at high doping concentration (n~10^{21} cm^{-3}) and its high electron mobility (10 cm^{2}V^{-1}s^{-1} to 100 cm^{2}V^{-1}s^{-1}) lead to good electrical conductivity[56]. Also, the study showed the large effective mass (m*~2^{-16} m_0)[57], [58] caused by the material's d-band nature and conduction band degeneracy[59], [60]. Additionally, introducing oxygen vacancies or substitutional doping of Sr^{2+} or Ti^{4+} sites with higher valence elements will change the electrical conductivity of $SrTiO_3$ from insulating to metallic behavior[58], [61], [62].

Figure 2.4 shows that $Sr_{0.95}La_{0.05}TiO_3$ reaches a maximum PF of 28×10^{-4} W/mK^2 at 320 K and carrier density of 0.2-2×10^{21} cm^{-3}[60], a value comparable to the PF of the most commonly

used low temperature TE material, Bi_2Te_3. This performance arises from the high Seebeck coefficient (~350 μV/K), which is due to high degeneracy of the conduction band and the high energy-dependent scattering rate. The rare earth elements Sm, Dy, and Y have smaller ionic radii +, which reduce lattice parameter[63]. The La and Dy co-doped $La_{0.08}Dy0.12Sr_{0.8}TiO_3$ has a lower PF owing to the decreased electrical conductivity. The decrease in conductivity which comes from the reduced carrier mobility due to the formation of the second phase ($Dy_2Ti_2O_7$) during the doping mechanism[64].

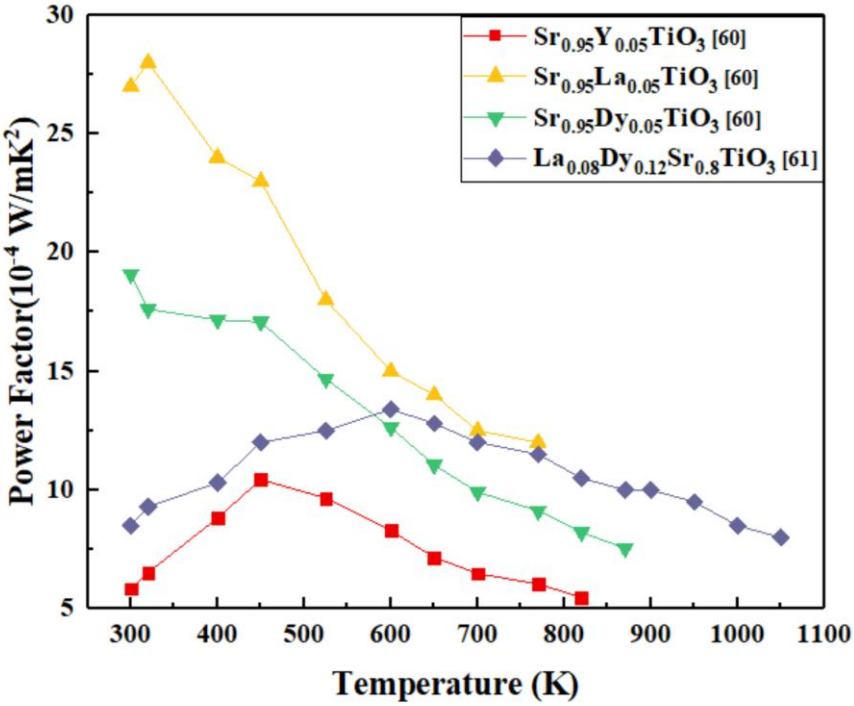

Figure 2.4 Temperature dependence of TE properties of Sr_xTiO_3

2.2.5 Na_xCoO_2

Na_xCoO_2 has a hexagonal layered crystal structure formed by alternating sodium ion (Na^+) and CoO_2 planes along the *c* axis. The structure of this material gives phonons and electrons different transport paths[65]. Electrons and holes pass through the CoO_2 layer during p-type conduction, whereas the disordered Na^+ layer provides the channel for phonon movement. Thus, this type of layered structure will simultaneously provide high electrical conductivity and low thermal conductivity, which is referred to as "phonon glass electron crystal" behavior[44], an ideal combination for TE applications. Therefore, it has been recognized that p-type alkali cobalt oxides

as highly promising oxide TE materials[66]. The study reported polycrystalline $Na_{0.85}CoO_2$ exhibited a high PF of 14×10^{-4} W/mK^2 at 300 K[67].

The effects of different dopants and doping levels have been widely investigated for Na_xCoO_2. Figure 2.5 shows a summary of the effects of various dopants on PF. Ag doping can increase both the electrical conductivity and Seebeck coefficient of Na_xCoO_2, resulting in a high PF value. It was expected the increase in electrical conductivity since Ag is a metal-phase dopant. However, it is not clear that the mechanism of the enhancement of the Seebeck coefficient. One possibility could be caused by the uniformity of Ag doping throughout the sample[68]. With 10% Ag doping, Na_xCoO_2 reached a PF of 18.92×10^{-4} W/mK^2 at ~ 1100 K with a doping concentration of ~10^{21} cm^{-3}[68].

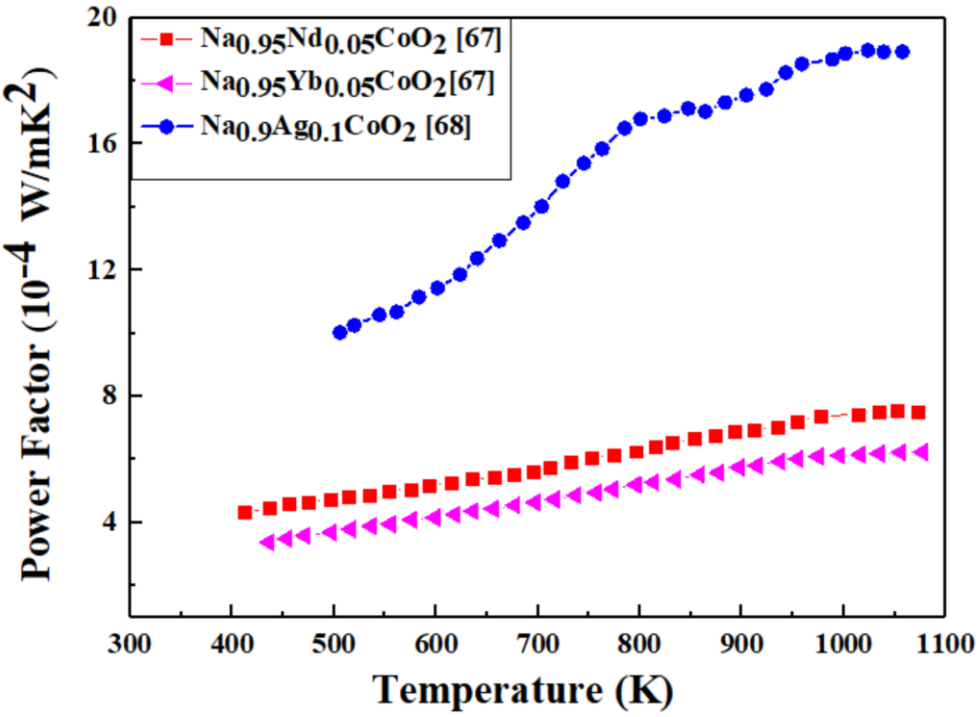

Figure 2.5 Temperature dependence of TE properties of Na_xCoO_2

2.2.6 $Ca_3Co_4O_9$

$Ca_3Co_4O_9$ is also a promising p-type oxide because of good electrical properties[69], [70]. $Ca_3Co_4O_9$ has stacked crystal structure that CoO_2 and Ca_2CoO_3 layers alternating along the *c* axis. The CoO_2 planes are mainly responsible for electrical conduction, and the Ca_2CoO_3 interlayers transfer heat by phonons. Un-doped polycrystalline $Ca_3Co_4O_9$ shows a room temperature Seebeck

coefficient of 150 μV/K, electrical conductivity of 80 S/cm, and PF of 1.5×10^{-4} W/mK^2.[71] However, using nobles metals such as Ag as a dopant at the Ca cationic atom site can both increase thermopower and electrical transport properties, which lead to increased PF values[72]. This can be attributed to more improvement for the Fermi level (E_F) than the valence band energy (E_V) of the crystal materials, which resulting from substituting Ag^+ for Ca^{2+} in $Ca_{3-x}Ag_xCo_4O_9$ ($0 < x < 0.3$)[73]. For TE materials, the Seebeck coefficient is proportional to the difference between the Fermi level and valence band energy (E_F - E_V), which indicates that Ag-doping in $Ca_3Co_4O_9$ can increase the Seebeck coefficient. The PF of $Ca_3Co_4O_9$ is much smaller than that of Na_xCoO_2 at 300K, but $Ca_3Co_4O_9$ is being more commonly used in TE applications. It is more stable with different compositional changes[74].

Figure 2.6 shows the effects of doping $Ca_3Co_4O_9$ with different transition metal elements. The PF increases with temperature for all of the dopants[75], [76]. Substituting transition elements (i.e. Fe, Bi, Mn, Ba, Ga) for Ca or Co is also effective in increasing the PF of $Ca_3Co_4O_9$. The Fe-doped $Ca_3Co_4O_9$ has a significant increase in PF from 2.3×10^{-4} W/mK^2 to 6.10×10^{-4} W/mK^2 at ~1000 K as shown in the figure. This is due to the substitution of Fe ions for Co ions in the CoO_2 layers changes the electronic structure and increases the electronic correlations. Thus, Fe is an effective dopant, which increases both Seebeck coefficient and electrical conductivity[76].

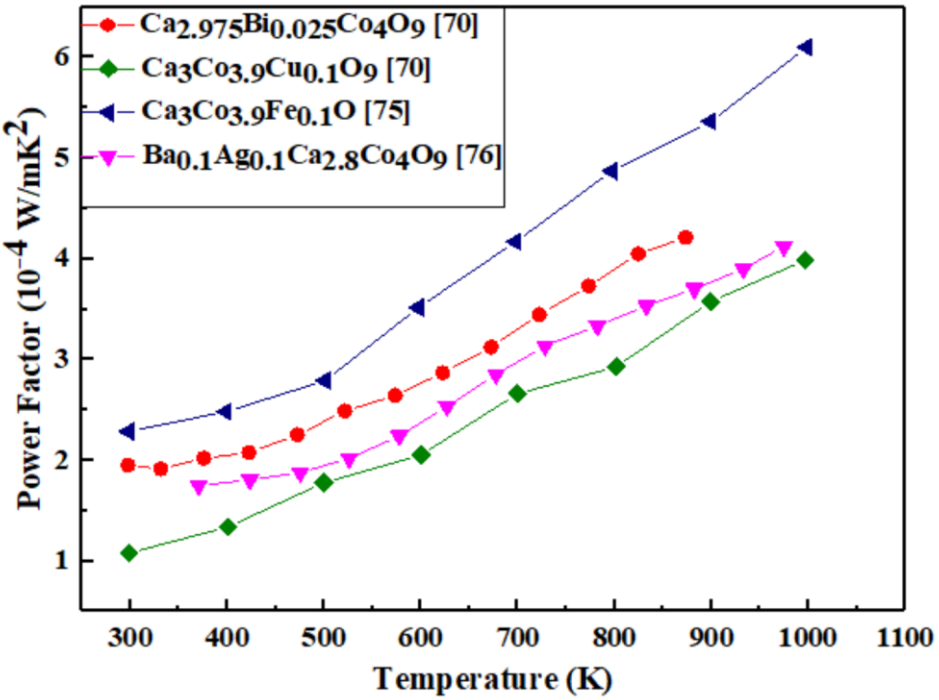

Figure 2.6 Temperature dependence of TE properties of $Ca_3Co_4O_9$

Table 2.1 Thermoelectric properties of metal oxides measured at 800K by different dopants, S is for Seebeck Coefficient, σ is for electrical conductivity, and PF is for power factor.

Material	**Dopants**	**|S| (μV/K)**	**σ (S/cm)**	***k*** **(W/mK)**	**PF (10^{-4}W/mK^2)**	**Ref.**
ZnO	Al	163	839	12	22.29	[77]
	Al, Ga	173	611	6.2	18.29	[78]
	Dy	55	80	-	0.24	[79]
SnO_2	Sb	150	190	11.5	4.28	[19]
	Cu, Sb	70	100	7	0.49	[44]
	Ti, Sb	65	100	2.1	0.42	[80]
	Sb, Zn	150	15	-	0.34	[42]
	Sb, Zn, Bi	125	290	-	4.53	[81]
In_2O_3	Ga	150	375	0.25	8.44	[82]
	Co	203	65	-	2.68	[53]
	Zn, Ge	126	428	3.2	6.79	[52]
Na_xCoO_2	Y	149.5	271.9	1.72	6.08	[83]
	Nd	150.0	280.8	1.43	6.32	[83]
	Sr	156.2	276	1.37	6.73	[83]
	Sm	145.4	271.8	1.38	5.75	[83]
	K	140.0	313	1.35	6.13	[83]
	Yb	139.0	268	1.47	5.18	[83]
	Ag	205.2	392.1	1.34	16.51	[84]
$Ca_4Co_4O_2$	Bi	166.7	145.76	-	4.05	[85]
	Fe	234.7	88.41	1.92	4.87	[76]
	Ga	173.6	114.17	1.52	3.44	[86]
$SrTiO_3$	La	210	250	5.5	11.03	[87]
	Sm	223	126	-	6.27	[87]
	Gd	206	130	-	5.52	[87]
	Dy	200	140	-	5.60	[87]
	La, Dy	159	420	3.46	10.62	[88]

2.3 Conformal Thermoelectric Devices Powered IoT Sensors for Civil Infrastructure Applications

As the demand of Internet of Things (IoT) with integrated wireless sensor networks (WSNs) increases, the sources of powering these sensors are a vital important issue to be addressed. The most common power source is using batteries in the industry. However, it requires extra labor and cost for replacement and maintenance, which will hinder the broader applications for IoT sensors. In order to overcome the limitations of batteries, researchers have explored several novel methods using renewable energy as power sources. While due to the traditional renewable energy sources working conditions and cost, they are not always desirable for WSNs and portable electronics. On the other hand, TEG devices have the advantages of their low maintenance, no moving parts, and easy to be installed. Thus, thermoelectric power generation technique draws more attention as a reliable energy source. As the temperature difference varies from human body to underground piping system, TEG devices are customized with different design. This section is to comprehensively review the research that have been conducted on TEG devices for powering IoT sensors in civil infrastructure applications with different design approaches and manufacturing processes.

2.3.1 Design Approaches

Based on the layout of TE legs on the flexible substrate and heat flow directions through the device, there are three design approaches of TEGs:

a) Lateral/lateral: TEGs with lateral heat flow, lateral TE legs arrangement (Figure 2.7a).
b) Vertical/lateral: TEGs with vertical heat flow, lateral TE legs arrangement (Figure 2.7b)
c) Vertical/vertical: TEGs with vertical heat flow, vertical TE legs arrangement (Figure 2.7c).

The first TEG design uses a lateral TE legs arrangement to convert a lateral heat flow. Printing or deposition technology are common methods for device fabrication. TE legs are printed or deposited on the flexible substrate surface. The device parameters can be controlled by using computer assisted software. In this design, the thickness and length of each TE legs can be manipulated, which allows creating thinner and longer TE legs compared to other types. It provides flexibility for device fabrications based on different applications. What's more, using lengthy TE

legs lead to the thermal resistance increases, which results in a temperature gradient increasing. As a result, a power output voltage is enhancing.

The second TEG design has an advantageous vertical heat flow may be achieved with lateral arrangement of TE legs. The lateral TE legs can be fabricated by using printing or deposition methods, which is earlier compared to conventional TEG device fabrication. By folding the lateral TE legs, it can achieve the heat flow is vertical. The vertical heat flow was achieved by integration of microcavities in the substrate under the TE legs. This device design can save time and cost on the device fabrication and achieve better performance as conventional TEG devices.

The last TEG design, i.e. vertical TEG, is made of TE legs fabricated vertically between the heat source and the heat sink. Thus, the heat is flowing vertically along the device. The device structure is conventional TEG device in the market. As the conventional fabrication method requires intensive labor, a novel fabrication technology is needed to used for this design with thick enough TE legs with high power output voltage.

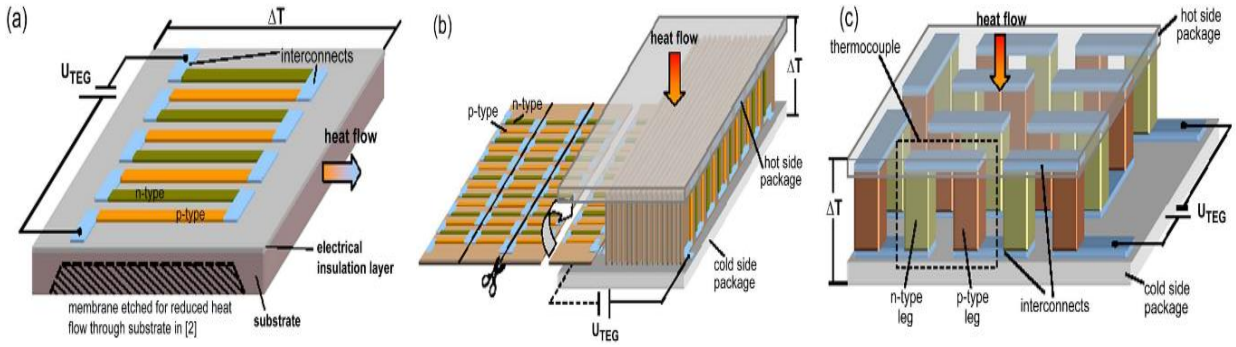

Figure 2.7 Design approaches for flexible TEGs. (a) lateral/lateral (b)vertical/lateral (c) vertical/vertical. (Reproduce from Ref. [89])

2.3.2 Fabrication Technologies

Conventional TEG device fabrication methods are focused on rigid device design; however, these methods are not the most suitable for flexible TEG devices. Research has been conducted on the fabrication methods for flexible TEGs since 2001[90]. There are several different fabrication techniques on flexible TEG, such as lift-off process[91], [92], flash evaporation method[93], [94], photolithography and etching technique[89], [95], [96], thermal evaporation[97], nano-materials[98]–[101], sputtering technique[102]–[104], screen printing[105]–[109], dispenser printing[110]–[113], and inkjet printing[114]–[117]. Among all

these methods, printing technologies are the most common techniques for flexible TEG device fabrication. Thus, this session focuses on screen, dispenser, and inkjet printing.

a) Screen printing

The screen printing is a process where the ink is forced through a mesh screen onto a surface. The pattern is defined by a mask or stencil. A blade or squeegee is used to fill the mesh apertures with the ink in a pattern across the screen[118], shown in Figure 2.8 (a). The advantageous for using screen printing for TEG fabrication is to achieve sufficient thickness. The viscosity of the ink can be up to several thousand cP, which provides the flexibility for TE ink synthesis by using different binders. Also, screen printing can be applied in a roll-to-roll process, which is easier for large scale fabrication.

However, there are still challenges in screen printing technology. As we discussed, screen printing can be achieved sufficient TE material thickness. It requires the ink with adequate viscosity to stand and takes longer time to dry. Another problem arises for the resolution of printed patterns. During the printing process, the volatile solvents in the ink could be dried on the screen-printing mask, which will deteriorate the resolution. Thus, it needs to synthesize TE ink with low vapor pressure formulations to avoid this problem.

Multiple groups have fabricated TEG module with screen printing using hybrid inorganic-organic inks. Navone et. al has developed $(Bi,Sb)_2(Te,Se)_3$-based thermoelectric modules by a screen-printing process. A 100 μm thickness films of n-type $Bi_2Se_{0.3}Te_{2.7}$ and p-type $Bi_{0.5}Sb_{1.5}Te_3$ were fabricated. The screen-printing process followed by the laser annealing for both rigid and flexible substrates. The microstructural and electrical properties of screen printed films of $Bi_2Se_{0.3}Te_{2.7}$ and $Bi_{0.5}Sb_{1.5}Te_3$ were investigated. Under 100 pulses laser sintering process, the films were crack free. The electrical conductivity of film that contains both $Bi_2Se_{0.3}Te_{2.7}$ and $Bi_{0.5}Sb_{1.5}Te_3$ was 800 S/m and Seebeck coefficient was 160 μV/K. The Seebeck coefficient decreased with the pulses number up to 80, where it stabilized at 90 μV/K[105].

A wearable TEG fabricated on a glass fabric by screen-printing process was studied by Kim et. al[109]. The device was thin (~500 μm), lightweight (~0.13 g/cm), and flexible. In order to improve the flexibility, the Cu film embedded in PDMS using the Ni peel-off method. The power output density of 0.38 mW/cm^{-2} at a temperature different of 50K. The flexible TE device can be repeated bending for 120 cycles without any damage on the device performance.

The binder is one of the factors that affected ink performance. Cao et. al studied the effect of two binder systems (A ang B), contacts and post-process for screen printed $Bi_{1.8}Te_{3.2}$ and Sb_2Te_3 based flexible thermocouples. Binder A is an 4,4'-Isopropylidenediphenol-epichlorohydrin based epoxy (3M) and binder B is an epichlorohydrin-polyglycol based epoxy (Dow Chemical). The optimized combination of materials and processes for TEG was $Bi_{1.8}Te_{3.2}$ with binder B, Sb_2Te_3 with binder A, SbTe as electrical contact with cold isostatic pressing assembly process. The BiTe/SbTe based TEG with binder B and SbTe contact electrodes generated an open circuit voltage of 32mV at a temperature different of 20˚C[119].

The studies on improving electrical properties of ink gained much interest in the screen printing community as well. By adding excess tellurium powder in the process chamber significantly improved carrier mobility by increasing the average scattering time of the carrier on the film. Kim et. al studied the TE properties of Sb_2Te_3 thick film with excess power and a subsequent annealing process. The maximum zT was achieved tat 0.32 at room temperature[120].

A similar result was found for screen printed Bi_2Te_3 thick film with optimized annealing process. The results showed the printed Bi_2Te_3 thick film annealed at 500˚C for 15 min in Bi and Te powders ambient, a power factor of 2.1 mW/mK^2 was achieved and a thermal conductivity of 1.0 W/mK. The resulted zT value of 0.61 at room temperature was achieved[121].

Other than telluride-based ink, Rudez et. al studied oxide-based ink using screen printing for TE device fabrication. Both $Ca_3Co_4O_9$ and $(ZnO)_5In_2O_3$ ink prepared by conventional methods. The inks were printed on aluminum substrate with post treatment. The highest electrical conductivity and Seebeck coefficient were 73 S/cm and 156 μV/K for $Ca_3Co_4O_9$. The highest electrical conductivity and Seebeck coefficient were 1.4 S/cm and -176 μV/K for $(ZnO)_5In_2O_3$[122].

Table 2.2 shows the comparison results for TE properties of inks by using screen printing process as below.

Table 2.2 Comparison of TE Properties of Materials and Device Fabricated via Screen Printing (S is for Seebeck Coefficient, σ is for electrical conductivity)

Materials	|S| (μV/K)	σ (S/m)	k (W/mK)	PF (μW/mK2)	zT	Ref.
$Bi_2Se_{0.3}Te_{2.7}$	123	3150	-	47.66	-	[105]
$Bi_{0.5}Sb_{1.5}Te_3$	123	780	-	11.8	-	[105]
Bi_2Te_3	140	55,000	1	-	0.32	[109]
Sb_2Te_3	99	130,000	1.25	-	0.29	[109]
Sb_2Te_3/binder A	134.38	2600	-	141	-	[119]
$Bi_{1.8}Te_{3.2}$/binder B	103.67	19,920	-	215	-	[119]
Sb_2Te_3	90-100	7,2000-120,000	0.9-1.1	-	0.32	[120]
Bi_2Te_3	137.5	2600	0.9-1.1	2100	0.61	[121]
$Ca_3Co_4O_9$	156	7400	-	1.6×10^{-4}	-	[122]
$(ZnO)_5In_2O_3$	176	139	-	1.4×10^{-6}	-	[122]

b) Inkjet printing

Inkjet printing is a type of computer-controlled printing that convert digital image/pattern by driving droplets of ink on to the substrate. It is a solution-based, non-contact, and mask-less deposition process in which materials are deposited at high speed and resolution by defined patterns[123], shown in Figure 2.8 (b). The advantageous of inkjet printing is the precise pattern designed by computer. Also, the substrate can be heated up, which helps the ink evaporate during printing process that improves the resolution of the ink.

Despite the widespread use of inkjet printing technology for portable electronics, there are still some challenges that hinder its applications. The printable ink viscosity is only up to 20cP, which has stricter requirement for choice of binder and synthesis methods. The nozzle clogging is one of the common problems for inkjet printing, thus the nanomaterial and binder need to be fully mixed and stable at room temperature before printing. Compared to screen printing

technology, it is hard to achieve thicker TE legs by using inkjet printing. Also, it may take longer time for inkjet printing process as it can be reached higher resolution.

Several studies demonstrated the feasibility of using inkjet printing for TEG device fabrication. Lu et. al was the first group demonstrated using inkjet printing for thin film TEG in 2014. The p-type $Sb_{1.5}Bi_{0.5}Te_3$ nanoparticles and n-type $Bi_2Te_{2.7}Se_{0.3}$ nanoparticles were synthesized by reacting Bi and Sb or Te and Se based on stoichiometric ratio. Solsperse 46000 was the only dispersing agent that had the ability to achieve both chemical and colloidal stability for the nanoparticles. The printed film that prepared by $Sb_{1.5}Bi_{0.5}Te_3$ nanoparticles showed a power factor of 77 $\mu W/mK^2$ at a temperature of 75˚C, and the $Bi_2Te_{2.7}Se_{0.3}$ film was 183 $\mu W/mK^2$ [114].

Hoong et. al studied TE properties of ZnO and $ZnFe_2O_4$ thin film printed by inkjet printing method. Through controlling the ratio of dopant added and heat treatment temperature, the better performance of printed thin film achieved. ZnO with Al doped at 0.04 reached highest electrical conductivity of 114.1 S/cm with Seebeck coefficient of 49.43 μV/K[124].

Organic TE materials 1,1,2,2,-ethenetetrathiolate(ett)-metal coordination polymers poly[Ax(M-ett)] (A=Na, K; M=Ni, Cu) have shown better TE properties. The polymer composites ink prepared by ball milling process with PVDF. A flexible TEG device with 6 thermocouples was fabricated by inkjet printing and generated a power output voltage of 15mV for temperature difference of 25 ˚C. The maximum power output was 45 nW for a load resistance of 5 kΩ[115].

Table 2.3 shows the comparison results for TE properties of inks by using inkjet printing process as below.

Table 2.3 Comparison of TE Properties of Materials and Device Fabricated via Inkjet Printing (S is for Seebeck Coefficient, σ is for electrical conductivity)

Materials	|S| (μV/K)	σ (S/m)	k (W/mK)	PF (μW/mK2)	zT	Ref.
$Sb_{1.5}Bi_{0.5}Te_3$	177±5	2000	-	77	-	[114]
$Bi_2Te_{2.7}Se_{0.3}$	139±2	6000	-	183	-	[114]
ZnO	49.43	11410	-	-	-	[124]
$ZnFe_2O_4$	31.66	-	-	-	-	[124]
Poly[Cu_x(Cu-ett)]/PVDF/DMSO	53±2	550±100	-	1.6	-	[115]
Poly[K_x(Ni-ett)]/PVDF/DMSO	60±10	520±50	-	1.8	-	[115]

c) Dispenser printing

The dispenser printing refers to filament-extrusion-based deposition pattern generation techniques. The dispenser printer consists of a three-axis stage, a pneumatically controlled syringe head and a heated vacuum chuck stage[125], shown in Figure 2.8 (c). The advantageous for dispenser printing is possible for 3D structures for TE legs with careful control of rheological behavior, ink composition, and printing parameters. Also, it can reach higher density for TE inks, which also reduce the drying-induced shrinkage after post annealing. For dispenser printing of sol-gel and colloidal ceramic inks, it has been demonstrated for printing features down to 250 nm and 200 μm, respectively[126].

As the bulk rheological behaviors of ink are sensitive to particle size, concentration, and the aggregation due to the internal attractive forces, it has limitations on microscale concentrated ink design. The control of ink properties and printing parameters are important for 3D structures, which need to take longer time for prototype development.

Chen et. al fabricated planar TEG using dispenser-printing with thick film. The zT of n-type Bi_2Te_3-epoxy composite was 0.18 and p-type Sb_2Te_3-epoxy was 0.19. A 50-couple TEG device with 5 mm × 640 μm × 90 μm printed dimensions was manufactured on a flexible polyimide substrate. The device generated a power output of 10.5 μW and 171.6 mV for a temperature difference of 20K, which resulted a power density of 75 $\mu W/cm^2$[125].

A novel process for preparing TEG with thick film dispenser printing technique was studied by Madan et. al. The microstructural, electrical, and thermal properties of n-type Bi_2Te_3 and p-type Sb_2Te_3 were investigated. Also, the effects of annealing time on the TE properties of printed film were examined. The maximum zT achieved at 0.41 under annealing temperature of 350˚C for 12h for p-type Sb_2Te_3 composite films. The maximum zT achieved at 0.16 under annealing temperature of 350˚C for 36h for n-type Bi_2Te_3 composite films[112].

Another approach for TEG device fabrication by dispenser printing integrated with a polymer mold was demonstrated. The inorganic-epoxy inks were synthesized with n-type Bi_2Te_3 and p-type $Bi_{0.5}Sb_{1.5}Te_3$ nanoparticles. The annealing temperature for the printed TE device was 250˚C in argon. The zT for n-type Bi_2Te_3 and p-type $Bi_{0.5}Sb_{1.5}Te_3$ were 0.0126 and 0.0615 at room temperature, respectively[127].

Table 2.4shows the comparison results for TE properties of inks by using screen printing process as below.

Table 2.4 Comparison of TE Properties of Materials and Device Fabricated via Dispenser Printing (S is for Seebeck Coefficient, σ is for electrical conductivity)

Materials	|S| (μV/K)	σ (S/m)	k (W/mK)	PF (μW/mK^2)	zT	Ref.
Sb_2Te_3	170	4000	0.24	120	0.19	[125]
Bi_2Te_3	160	3000	0.24	110	0.18	[125]
Bi_2Te_3	275	1700	0.24	150	0.16	[112]
Sb_2Te_3	152	31500	0.54	840	0.46	[112]
$Bi_{0.5}Sb_{1.5}Te_3$	272	1440	0.52	1.07×10^{-4}	0.0615	[127]
Bi_2Te_3	159	800	0.48	0.2×10^{-4}	0.0126	[127]

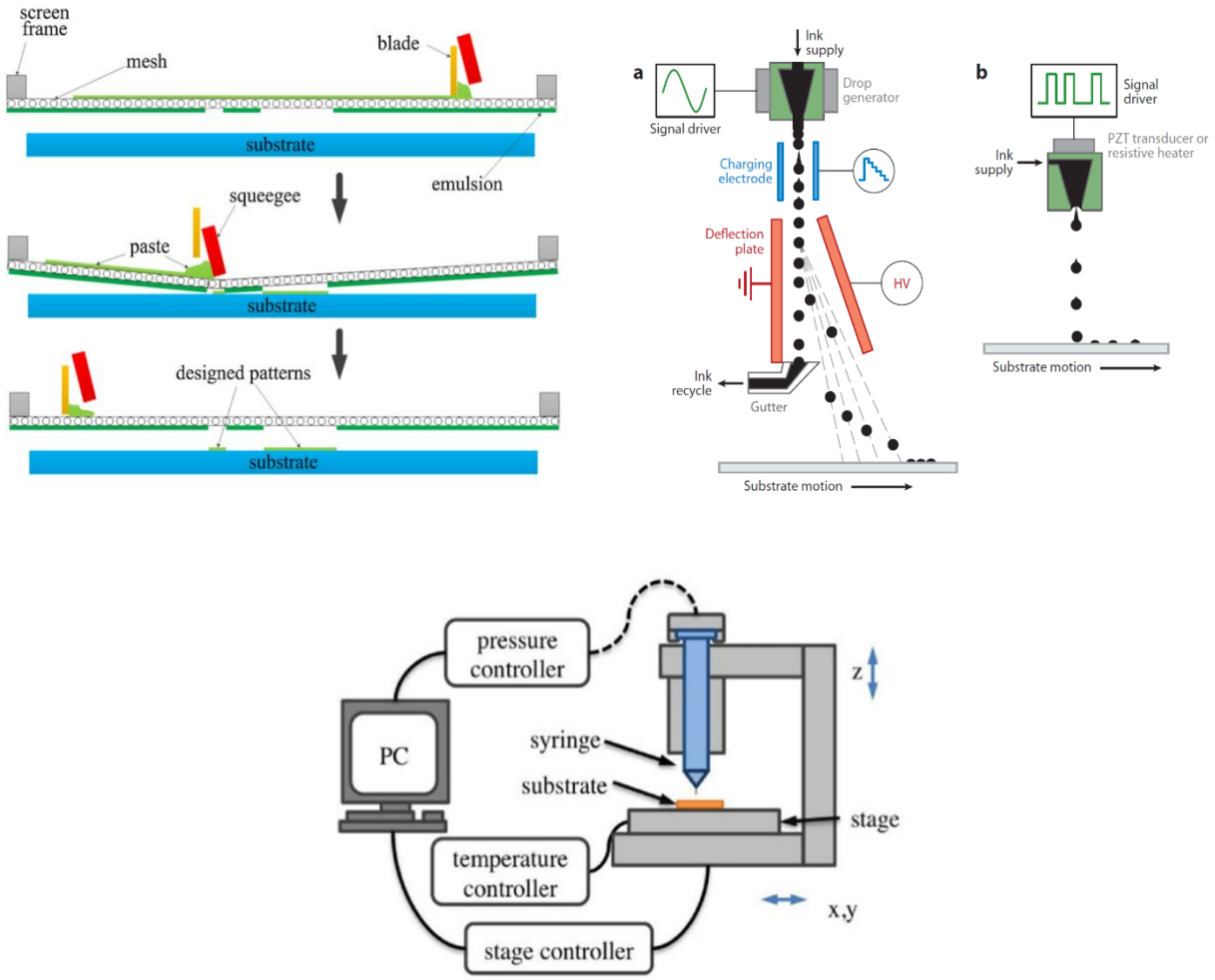

Figure 2.8 (a) Diagram of screen printing. (Reproduce from Ref. [118]). (b) schematic of continuous inkjet printing. (reproduced from Ref. [123]). (c) Schematic of dispenser printing (Reproduce from Ref. [125])

2.3.3 Civil Infrastructure Applications

The safety of civil infrastructure is one of the most important aspects for public health. Using WSNs for measuring corrosion, temperature, flow, and stresses will provide critical data for enhanced safety maintenance. Self-powered WSNs combined with TEGs can be used where heating sources like heat pipe, bridge, and buildings. Kim et. Al 2018[128] fabricated a large area flexible TEG capable of harvesting energy from the heat of a heat pipe. As shown in Figure, the flexible TEG integrated with a flexible heat sink was shaped and tested around an aluminum heat

pipe. In order to simulate the heat generated from a hot fluid, a thin adhesive heater was attached to the inner wall of the pipe. To compensate the increase spreading thermal resistance, a highly orientated graphite sheet was used as the thermal interface materials between the flexible TEG and flexible heat sink, as shown in Figure 2.9.

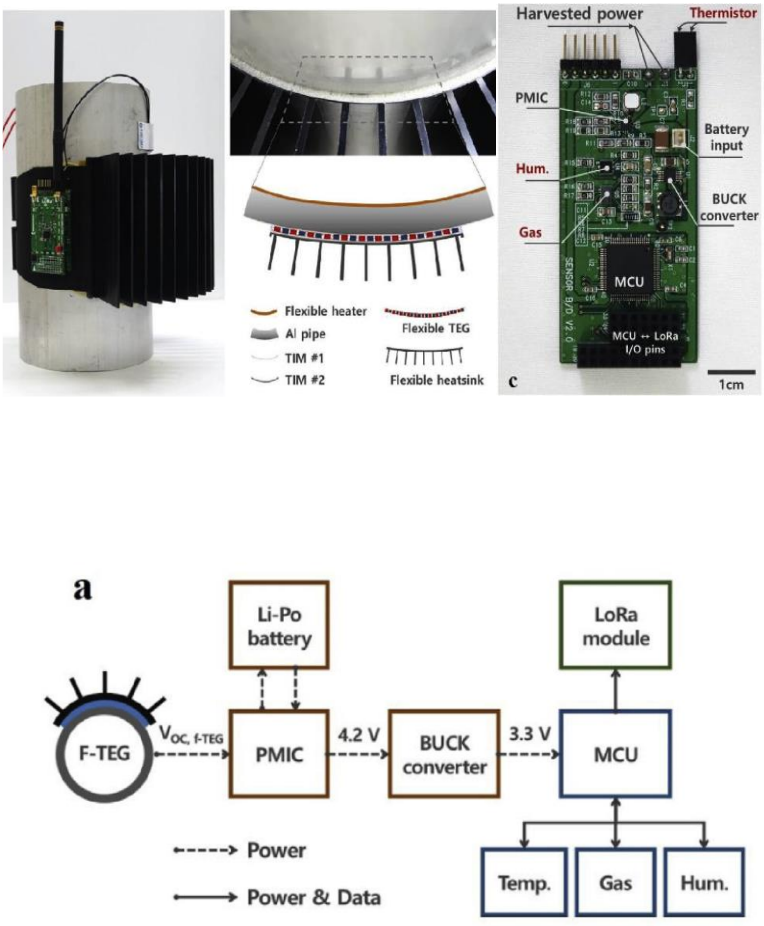

Figure 2.9 (a) Front, (b) side and (c) top view of the front side of the self-powered WSN driven by flexible thermoelectric generator (f-TEG). A schematic drawing of the cross-section of the combined heat pipe/f-TEG/heatsink is shown. (Reproduce from ref. 116)

The study shows that a 140×113mm^2 f-TEG generated 272 mW of energy from a heat pipe at a temperature of 70˚C. A self-powered WSN system with the capability of remote monitoring of the heat pipe temperature, ambient temperature, humidity, CO_2, and volatile organic compound concentrations via LoRa communication. The distances that self-powered WSN system can wirelessly transmit the data are as long as 500m. [116]

Another group also studied flexible TEG for powering wireless sensors on the heat pipe.[129] The TEGs in this work were screen printed from commercial silver ink as p-type material and in-house formulated nickel pastes as n-type material, shown in Figure 2.10. The measured device is vertically installed on a pipe. The output voltage is then connected with a commercial DC-DC converter (LTC 3108) to charge a super capacitor. The charged capacitor can power the WSNs to transmit information to the end user successfully.

Under the optimized internal resistances and device design, this TEG device with 420 junctions can produce 308 μW of power at ΔT= 127K, which is sufficient to power a temperature sensing circuit with wireless communication capabilities.

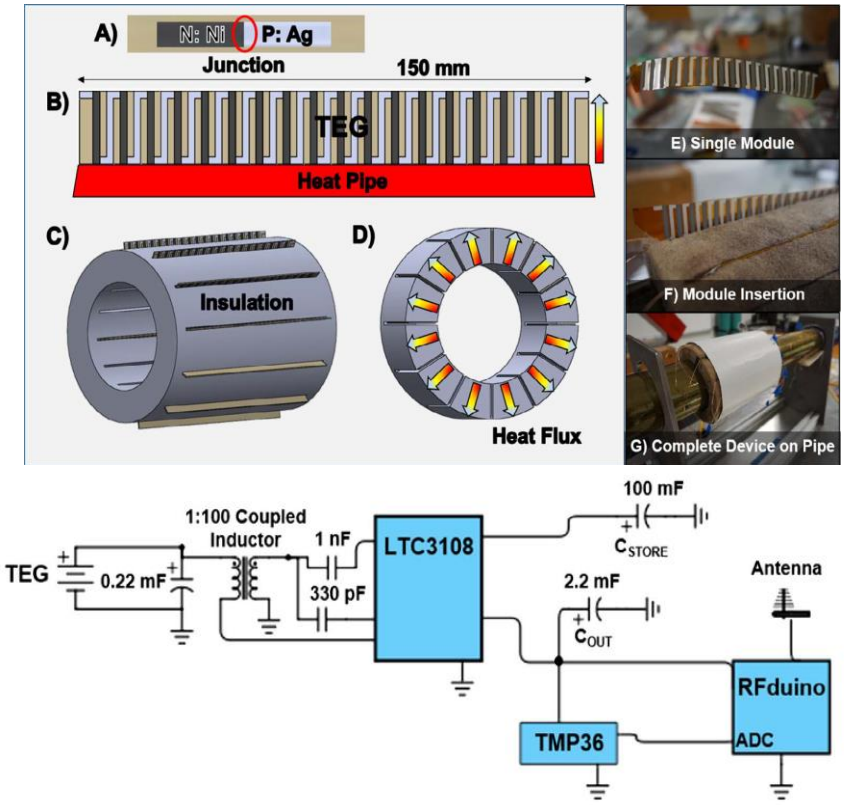

Figure 2.10 Flexible TEG on heat pipe for WSN application. (Reproduce from ref. 117)

3. OXIDES THERMOELECTRIC MATERIALS SYNTHESISI AND CHARACTERIZATION

This chapter contains portions of a previously published manuscript Y. Feng et al., "Temperature dependent thermoelectric properties of cuprous delafossite oxides," Composites Part B: Engineering, vol. 156, pp. 108–112, Jan. 2019, doi.org/10.1016/j.compositesb.2018.08.070

3.1 Copper Aluminum Oxide-$CuAlO_2$

In 1997, Kawazoe *et al*. reported the p-type conductivity of transparent thin film $CuAlO_2$ as 1 S/cm at room temperature[130]. Also, the previous study shows $CuAlO_2$ has a relatively large electronic bandgap (~3.4 eV) and flat band structure[131]. Moreover, Hao *et al*. has conducted a computational-driven TE materials search and identified $CuAlO_2$ is a promising p-type candidate[26]. $CuAlO_2$ has a layered, delafossite structure that can be considered a natural superlattice, which is more stable and easy for synthesis[132]. Superlattice structures show a lot of promise for TE materials[133]–[135]. Other layered oxide materials used for TE, such as $NaCo_2O_4$[65], and $SrTiO_3$[74] have demonstrated relatively large zTs. However, temperature dependent thermoelectric transport properties of $CuAlO_2$ have not been fully exploited in existing literatures.

To fill this knowledge gap, we have conducted a systematic study of TE properties of $CuAlO_2$ with the function of temperatures from 300K to 780K. Solid-state synthesis of $CuAlO_2$ created a material with a nanostructured grain size, which affects electrical and thermal conductivity. Cold-pressed pellets kept powder maintained the grain size during the annealing process. Annealing temperature and time were optimized for microstructure, which will significantly affect thermoelectric properties[136]. The effects of different annealing times for $CuAlO_2$, on resulting microstructure, and related thermoelectric properties of $CuAlO_2$ were studied.

3.1.1 Materials Synthesis

High purity CuO and Al_2O_3 were stoichiometrically mixed with alcohol, and ball milled for six hours using 3mm yittria stabilized zirconia grinding media at a 40:1 ratio. The resulting powder was dried in an oven at 363K, then pressed into pellets with 13 mm diameter and 1.5 mm thick at 394K under 8 Tons for 30 minutes. The pressed pellets were annealed at 1373K for five

hours, eight hours and 12 hours, respectively, in a combination of nitrogen and ambient environments. All samples were furnace cooled.

3.1.2 Sample Characterization

The crystal structure and purity of the samples were analyzed via powder X-ray diffraction (XRD) using a Panalytical Empyrean Powder X-ray Diffractometer at 40kV, 40 mA with Bragg-Brentano mode with Cu Kα radiation. The diffraction patterns were collected from 10-80˚ for five times. The average crystalline size of the powders was calculated according to Scherrer's equation. A high-resolution transmission electron microscope (FEI Tecnai F20ST) was used to investigate the crystal structure of annealed powders. Seebeck coefficient was determined through a home-built measurement system that applies a temperature gradient through the sample and measures the resulting voltage output as described elsewhere[137][138]. The Seebeck coefficient was calculated from the slope of temperature vs voltage. Electrical conductivity was directly measured by the four-probe hall measurement system (Ecopia AHT55T5). The thermal conductivity was determined using the transient time-dominant method from the thermal diffusivity and specific heat measured by laser flash method (LFA 467, NETZSCH, Germany). All the thermoelectric properties were measured from 300K to 780K in a nitrogen environment.

3.1.3 Crystal Structure

Figure 3.1 shows the results of powder x-ray diffraction patterns for $CuAlO_2$ powder with varying annealing times at 1373K. It can be seen that higher purity of $CuAlO_2$ powder was obtained annealing at 1373K for 12 hours, due to the complete reaction between CuO and Al_2O_3. The main reactions for the formation of $CuAlO_2$ are:

$$CuO + Al_2O_3 \rightarrow CuAl_2O_4 \quad 3.1$$

$$CuAl_2O_4 + CuO \rightarrow 2CuAlO_2 + 1/2\ O_2 \quad 3.2$$

There will be a formation of $CuAl_2O_4$ at annealing temperature between 1173K and 1273K. The following reactions will result in impurities of $CuAlO_2$:

$$CuAlO_2 + O_2 \rightarrow 1/2\, CuAl_2O_4 + 1/2\, CuO \quad 3.3$$

$$CuAl_2O_4 \rightarrow CuAlO_2 + 1/2\, Al_2O_3 + 1/4\, O_2 \quad 3.4$$

As shown in XRD pattern with CuO and Al_2O_3 peaks. The crystalline structure of the annealed $CuAlO_2$ bodies is rhombohedral, $R\bar{3}m$, a = 2.8567 Å and c = 16.943 Å (JCPDS Card File: 00-035-1401).

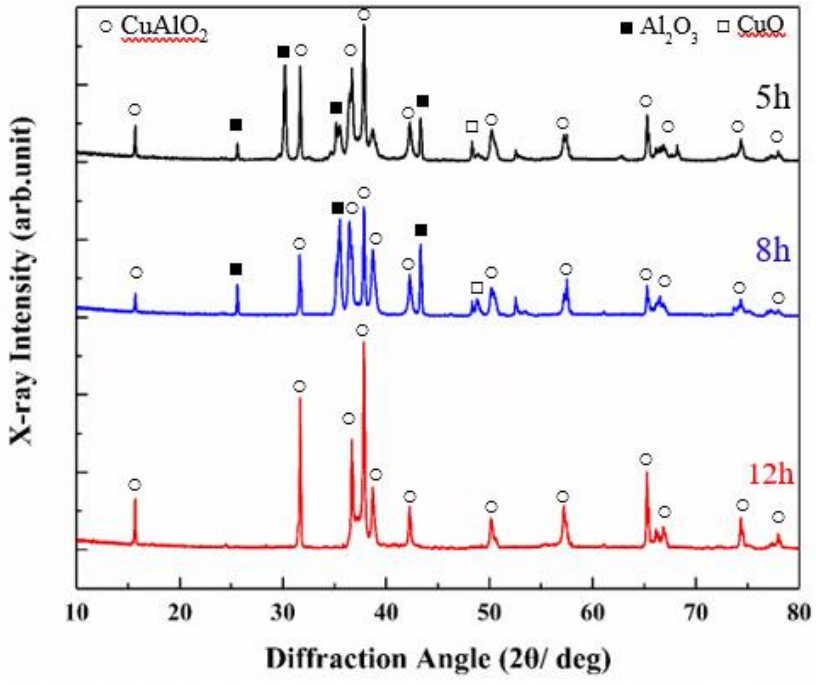

Figure 3.1 The XRD patterns of $CuAlO_2$ powder with different annealing time at 1373K

Further investigation on the microstructure of annealed $CuAlO_2$ powder is done by using a high-resolution transmission electron microscope (HRTEM). Clear lattice fringes of $CuAlO_2$ is observed as shown in Figure 3.2 (a), which indicates a high quality of crystal structure. Furthermore, using a Fast Fourier Transform (FFT) image obtained by Digital Micrograph software the d-spacing of the lattice orientation was calculated. The d-spacing of the lattice fringes (Figure 3.2 b) was found to be 2.47 Å, which corresponded to the reported d-value (2.4474 Å) of $(10\bar{1}1)$ plane of r-$CuAlO_2$ (JCPDS Card File: 00-035-1401). The FFT image as shown in Figure

3.2 (c) indicates the rhombohedral structure. The HRTEM results are confirmed with an XRD pattern of the crystalline structure of r-$CuAlO_2$.

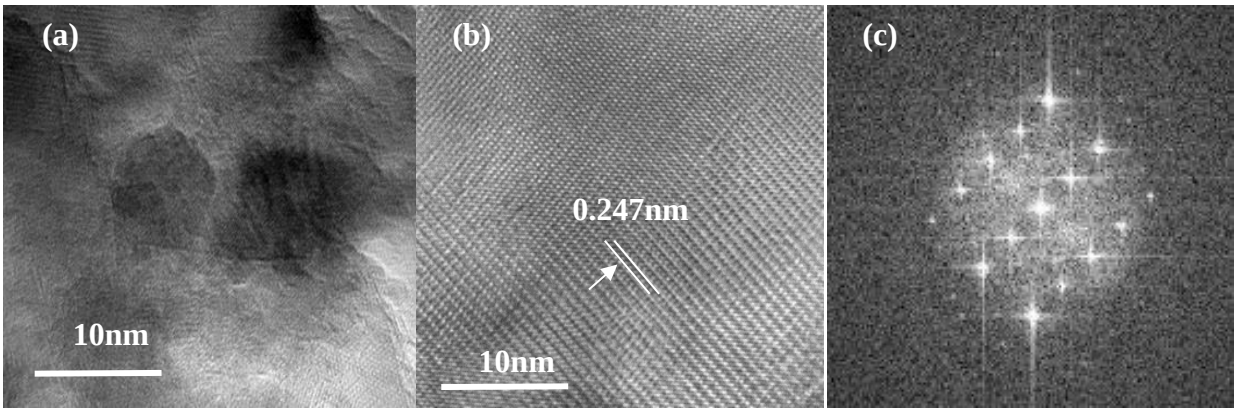

Figure 3.2 (a)The HRTEM image of $CuAlO_2$ powder annealing at 1373K; (b) HRTEM image of an individual grain and (c) FFT pattern

3.1.4 Thermoelectric Properties

Thermoelectric properties strongly depend on the microstructure of the materials. Figure 3.3 shows the temperature-dependent Seebeck coefficient of $CuAlO_2$ powder annealing at 1373K for 12 hours. The Seebeck coefficient shows a positive sign over the measured temperature range indicating p-type conductor behavior, which is due to the behavior of hole majority carriers. The Seebeck coefficient increases with the increase of temperature and the highest Seebeck coefficient reaches 665μV/K at 780K. No bipolar effect was observed due to the large band gap of $CuAlO_2$ (~ 3.4eV) [131]. Lu et.al reported the Seebeck coefficient value as 460 μV/K at 780K for $CuAlO_2$ pellets prepared by SPS method[139], which is lower due to the crystal defects i.e., impurity. Also, the grain size will grow during SPS pressing, which leads to more complicated electron scattering mechanisms. This will affect the electrical properties of materials. However, the overall values of Seebeck coefficient for $CuAlO_2$ samples are relatively high.

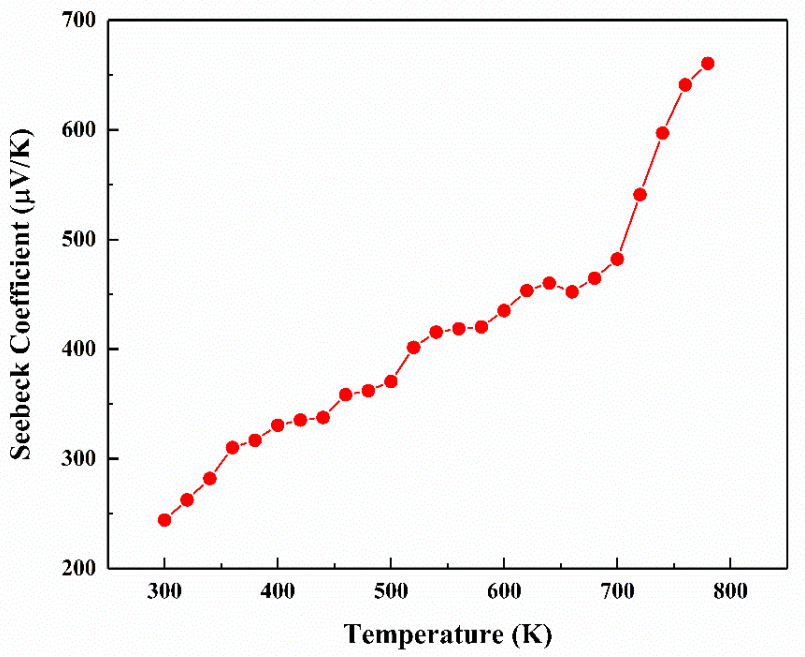

Figure 3.3 Temperature-dependent Seebeck coefficient of $CuAlO_2$ powder annealing at 1373K for 12h

Seebeck coefficient is an intrinsic material property, which measures the thermoelectric voltage induced in response to a temperature difference across the material. High effective mass of the charge carriers will lead to high Seebeck coefficient. The high hole effective mass will increase the density of states at an energy E in the valence band as shown below:

$$g_v(E) = \frac{m_p^* \sqrt{2m_p^*(E_v - E)}}{\pi^2 \hbar^3}, \qquad E \leq E_v \tag{3.5}$$

For semiconductors, the relationship among Seebeck coefficient, effective mass, and carrier concentration can be expressed below:

$$S = \frac{8\pi^2 k_B^2}{3eh^2} m^* T \left(\frac{\pi}{3n}\right)^{2/3} \tag{3.6}$$

where k_B is the Boltzmann constant, e is the carrier charge, h is Planck's constant, m^* is the effective mass of the charger carrier, and n is the carrier concentration. Seebeck coefficient reflects the average entropy transported per charge carrier and thus decreases with the increasing carrier

as shown in equation (3). Thus, high effective mass and low carrier concentration of the materials are desirable to reach high Seebeck coefficient as shown here.

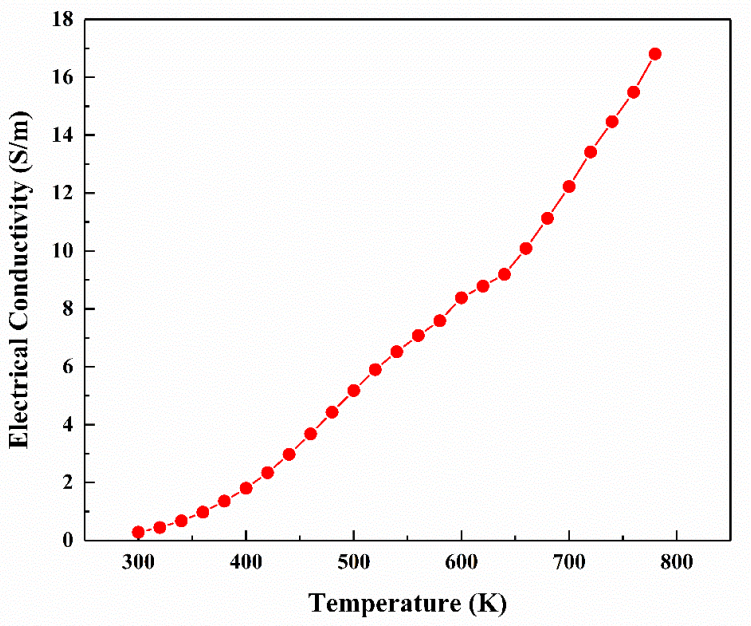

Figure 3.4 Temperature-dependent electrical conductivity of $CuAlO_2$ powder annealing at 1373K for 12h

The Seebeck coefficient is directly related to the density of states, whereas the electrical conductivity can be limited by electronic and morphological defects[140]. Figure 3.4 shows the electrical conductivity increases with the temperature increase, which indicates semiconductor behavior. With the increasing temperature, thermal energy excites free electrons from the valence band to the conduction band resulting in increased electrical conductivity. The highest electrical conductivity reached is 17 S/m at 780K. For p-type transparent conductivity oxides (TCOs), those bands are very flat due to the localized oxygen p-type nature of the valence band[141]. P-type TCOs have high hole effective mass. Thus, it is very challenging to reach high electrical conductivity for $CuAlO_2$.

The relationship between electrical conductivity and effective mass is shown below:

$$\sigma = \frac{ne^2\tau}{m^*} \qquad 3.7$$

As can be seen that high effective mass will result in low mobility, thus the electrical conductivity decreases. To reach high electrical conductivity, higher carrier concentration and lower effective mass are desirable, however it often degenerates the Seebeck coefficient of materials. Thus, the investigation of an effective doping mechanism for improving electrical conductivity without degenerating the Seebeck coefficient is crucial to increasing electrical properties of p-type TCOs materials for applications of thermoelectric power generation.

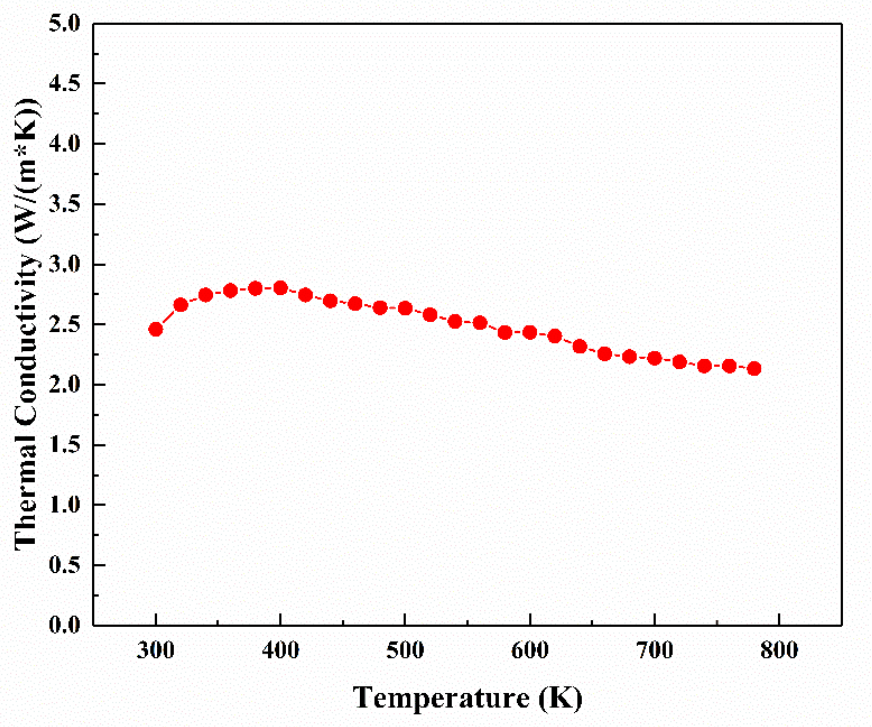

Figure 3.5 Temperature-dependent thermal conductivity of $CuAlO_2$ powder annealing at 1373K for 12h

For thermoelectric applications, thermal conductivity (*k*) is a very important parameter as it determines the efficiency of heat flow through materials and system. Figure 3.5 shows the temperature dependent thermal conductivity of the $CuAlO_2$ annealing at 1373K for 12 hours. The value of thermal conductivity is 2.134 W/mK at 780K. The trend of thermal conductivity increases and then decreases with the temperature increase.

The total thermal conductivity (κ_T) consists of contributions from both electron and phonon transport, defined as following:

$$\kappa_T = \kappa_e + \kappa_l \quad 3.8$$

where κ_e and κ_l are respectively, the electron and lattice thermal conductivity. κ_l is known as the most important mechanism for heat conduction in semiconductors at temperatures close to room temperature, which normally accounts for 90% contributions in wide bandgap materials.

At lower temperatures the thermal conductivity of $CuAlO_2$ is low. Energy and phonon vibrations increase with a temperature increase, which results in an increase of group velocity that enhances thermal conductivity. However, with the temperature increases, more phonon scattering is observed from point defect scattering contributions due to mass disorder and bond length disorder at higher temperature, and phonon-phonon Umklapp scattering. These phenomena typically lead to a decreased thermal conductivity with the temperature increased as we observed in this study. Thus, one way to decrease the lattice thermal conductivity is to decouple electron and phonon transport using nano-structures to scatter phonons more effectively than electrons, which decreases thermal conductivity without significantly disrupting the electrical conductivity. To achieve this goal, we used the cold pressing method to maintain the small nano-grain size (~ 80 nm) of the ball milled powder, which reduces lattice thermal conductivity without compromising electrical properties as shown in this work.

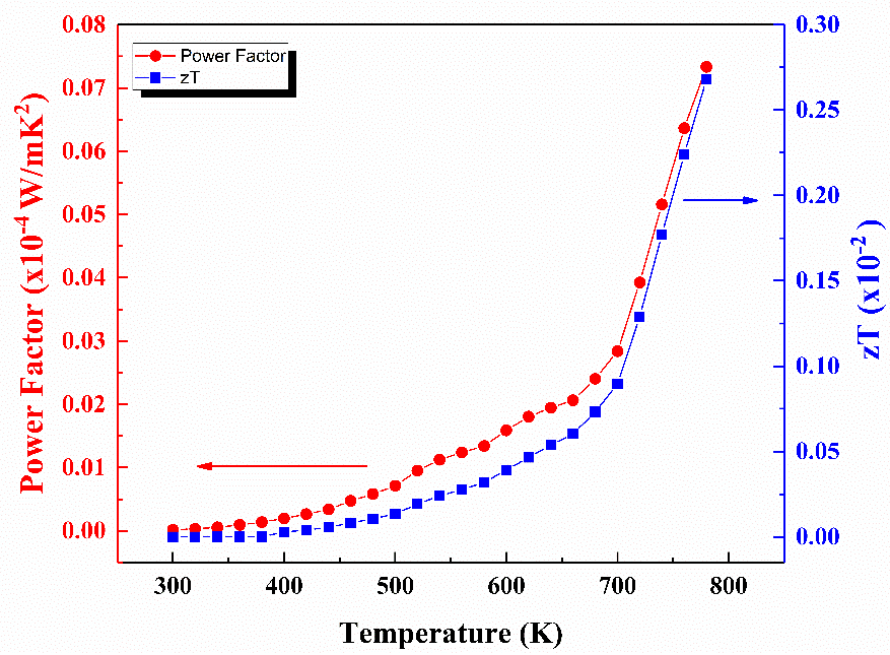

Figure 3.6 Power factor and Figure of Merit of $CuAlO_2$ powder

The power factor ($PF=S\sigma^2$), which is calculated from the data in Figure 3.3 and Figure 3.4, represents the electrical performance of thermoelectric materials, as shown in Figure 3.6. The power factor increases as the temperature increases up to 780K. The value of the power factor at 780K for $CuAlO_2$ samples is 0.78×10^{-5} W/mK^2. The value of the power factor is indicative of a thermoelectric materials ability to generate electricity, which increases with the temperature.

The quality of materials for TE applications is described by a dimensionless figure of merit, zT. The calculated zT values are shown in Figure 3.6. Both electrical and thermal properties will affect materials figure of merit. There are two strategies to improve $CuAlO_2$ zT: (1) to improve the power factor, which requires optimized dopants for $CuAlO_2$ that increases both electrical conductivity and Seebeck coefficient; (2) to reduce the thermal conductivity by using small-nanostructure-size (SNS) limit[26] that requires optimum nanostructure size *a* is larger than electron mean free path but smaller than phonon mean free path, which results in the increase of phonon scattering without deteriorating electron transport. Thus, lattice thermal conductivity will decrease, and electrical conductivity will maintain high values to reach a high zT.

3.1.5 Conclusions

In this work, we have investigated the temperature dependent thermoelectric properties of $CuAlO_2$ with a focus on optimization of annealing process for improved thermoelectric properties. Both XRD patterns and HRTEM results show high purity and a rhombohedral structure of $CuAlO_2$ powder obtained when annealed at 1373K for 12 hours. The annealing time is one of the key factors for the formation of 3R delafossite phase in $CuAlO_2$. The resulting nanocrystalline $CuAlO_2$ has been characterized both electrical and thermal properties. The value of the Seebeck coefficient is positive over the measured temperature range, which shows p-type behavior, and it increases with the increase of temperature. The electrical conductivity increases as the temperature increases, indicating semiconductor behavior. The high Seebeck coefficient and relatively low electrical conductivity are due to the high effective mass of the charge holes in $CuAlO_2$. Small nano grains in our samples have led to scattering more phonons without deteriorating electrons, which results in low thermal conductivity. The figure of merit is reached at 0.27×10^{-2} at 780K.

$CuAlO_2$ is a desirable material for mid-high temperature range due to the stability and high Seebeck coefficient, which has a square effect on the power factor. However, the low electrical

conductivity limits the broader applications in the thermoelectric field. Thus, an effective doping mechanism for r-$CuAlO_2$ is necessary for future work.

3.2 Palladium Bismuth Oxide-$PdBi_2O_4$

Bi_2O_3 is the one of common constituents in thick film materials that used for manufacturing high performance electronic ceramics[142]. The interaction of Pd and Bi_2O_3 is very important for enhancement of electrical properties, which obtained much interest in oxides TE materials studies. Bettahar *et.al* reported the electrical conductivity of $PdBi_2O_4$ that exhibited relatively high conductivity (σ~10 S/cm) and low activation energies (~0.02 eV)[143]. As for most oxides TE materials, the high lattice thermal conductivity and low electrical conductivity have significantly limited their applications to date.

He *et. al* predicted $PdBi_2O_4$ to be a highly efficient hole-doped TE material with low lattice thermal conductivity and high power factor by using first-principles calculations[144]. As a result, Bi^{3+} $6s^2$ long pair electrons show strong anharmonicity, which leads to low lattice thermal conductivity. The flat-and-dispersive valence band structure with high degeneracy indicates a large power factor (high Seebeck coefficient and high electrical conductivity).

To confirm the theoretical study, we have systematically conducted TE properties of $PdBi_2O_4$ with a function of temperature from 300K-773K. The microstructural, electrical, and thermal properties of the material were investigated. We also compare the theoretical results with experimental results to explore the feasibility of using $PdBi_2O_4$ as p-type TE material.

3.2.1 Sample Characterization

A high-resolution transmission electron microscope (FEI Tecnai F20ST) was used to investigate the crystal structure of annealed powders. The Seebeck coefficient was determined through a home-built measurement system that applies a temperature gradient through the sample and measures the resulting voltage output as described elsewhere[137][138]. The Seebeck coefficient was calculated from the slope of temperature vs voltage. Electrical conductivity was directly measured by the four-probe hall measurement system (Ecopia AHT55T5). The thermal conductivity was determined using the transient time-dominant method from the thermal diffusivity and specific heat measured by laser flash method (LFA 467, NETZSCH, Germany). All the thermoelectric properties were measured from 300K to 700K in a nitrogen environment.

3.2.2 Crystal Structure

Figure 3.7 shows the crystal structure of $PdBi_2O_4$. $PdBi_2O_4$ has a tetragonal crystal structure, P4/ncc (No. 130). Pd^{2+} is connected with two neighboring BiO_6 octahedra neighbors. Along the *c* axis two neighbors are edge-sharing and along the *ab* plane by corner-sharing. The BiO_6 octahedra shows strong asymmetric distortion, which indicates strong anharmonicity. HRTEM shows the size of nanoparticles is around 80 nm with clear crystalline.

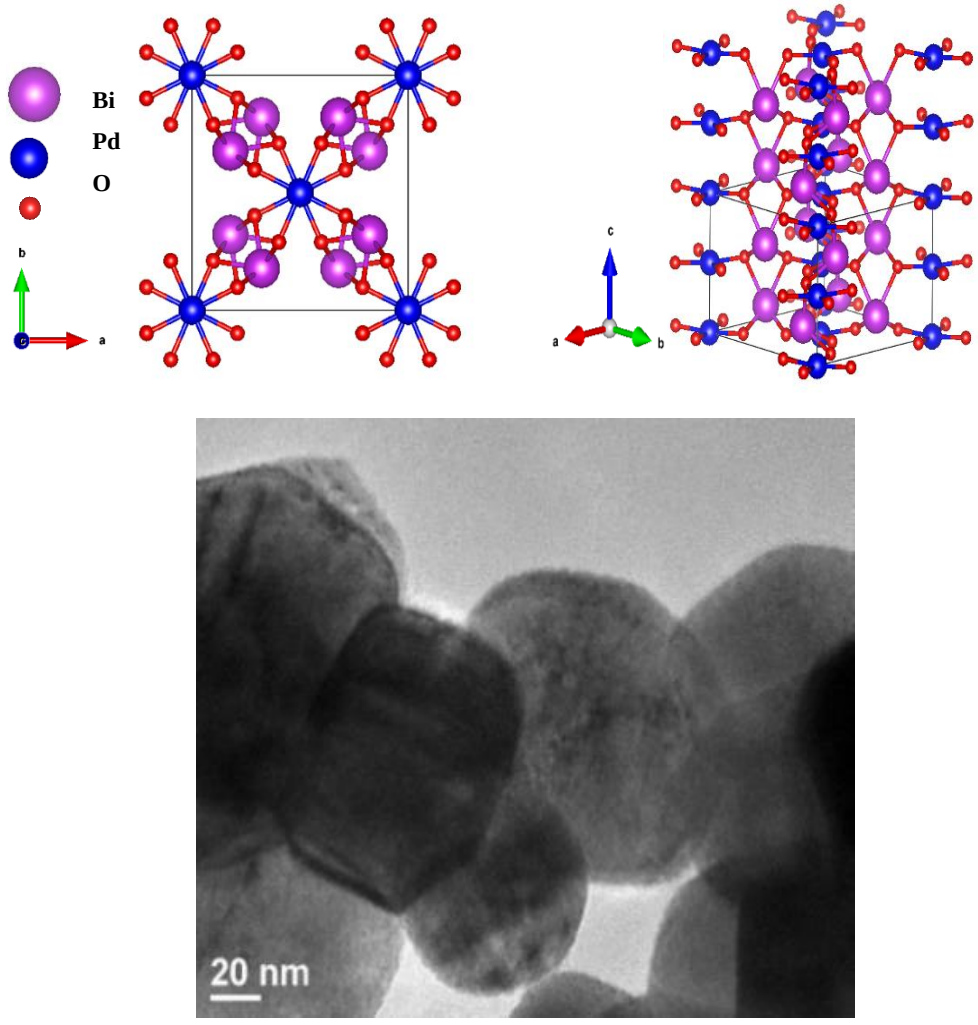

Figure 3.7 Crystal structure and HRTEM image of $PdBi_2O_4$

3.2.3 Thermoelectric Properties

The comparison between experimental and theoretical results on the temperature-dependent Seebeck coefficient of $PdBi_2O_4$ is shown in Figure 3.8. With the temperature ranges from 300K to 770K, the Seebeck coefficient has a positive sign that shows p-type behavior. Both experimental and theoretical results show the increasing trend, where a maximum Seebeck coefficient of 1000 μV/K at 700K is reached at a carrier concentration of 5E16 cm^{-3}. The high Seebeck coefficient is due to the low carrier concentration of the material. Also, the band structure of $PdBi_2O_4$ is relatively flat in the *ab* plane[144]. A flat band affords a high density of states, which indicates a high effective mass of the material. Based on the equation, high effective mass and low carrier concentration result in a high Seebeck coefficient. With increasing carrier concentration, the Seebeck coefficient drops as shown in the comparison data in Figure 3.4**.**

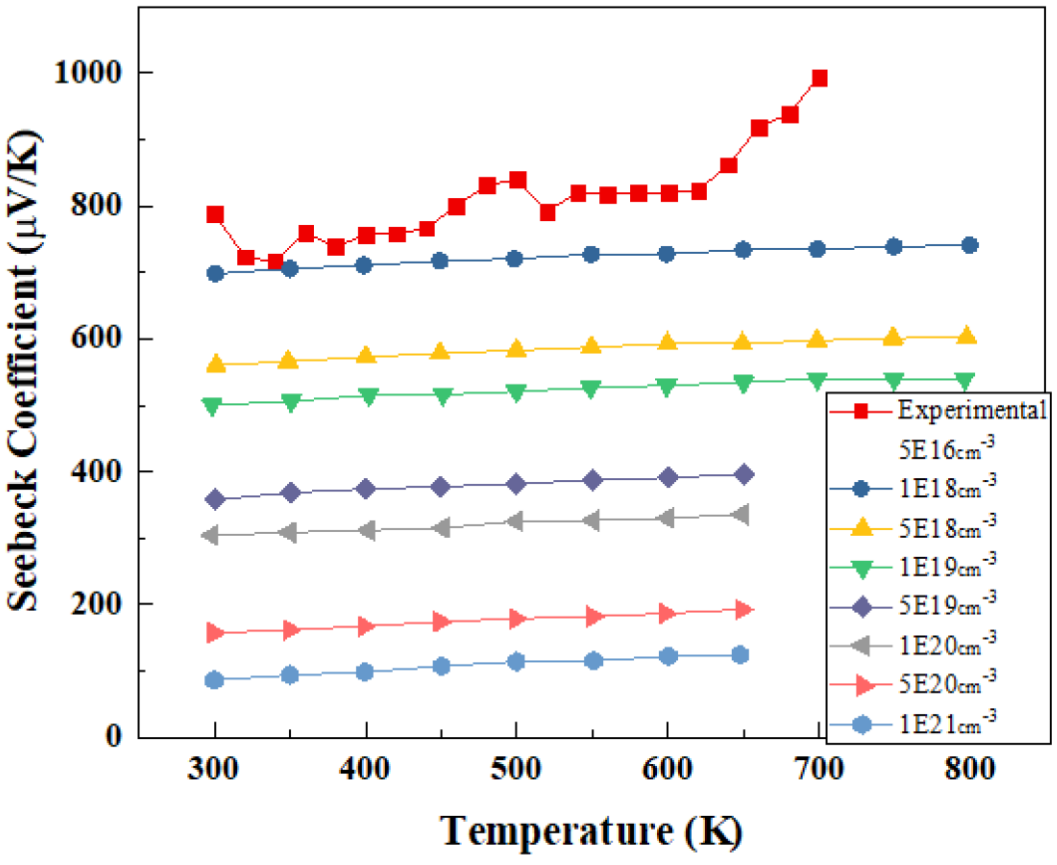

Figure 3.8 Seebeck coefficient of $PdBi_2O_4$ experimental result vs. theoretical result

Figure 3.9 shows the temperature dependent electrical conductivity of the material. With increasing temperature, the electrical conductivity increases showing semiconductor behavior. At temperatures around 700K, the electrical conductivity reaches 3.06 S/m. This is an undoped material that leads to a low carrier concentration.

The relationship between electrical conductivity and effective mass is shown in Equation 3.7. As can be seen, a high effective mass will result in low mobility, thus the electrical conductivity decreases.

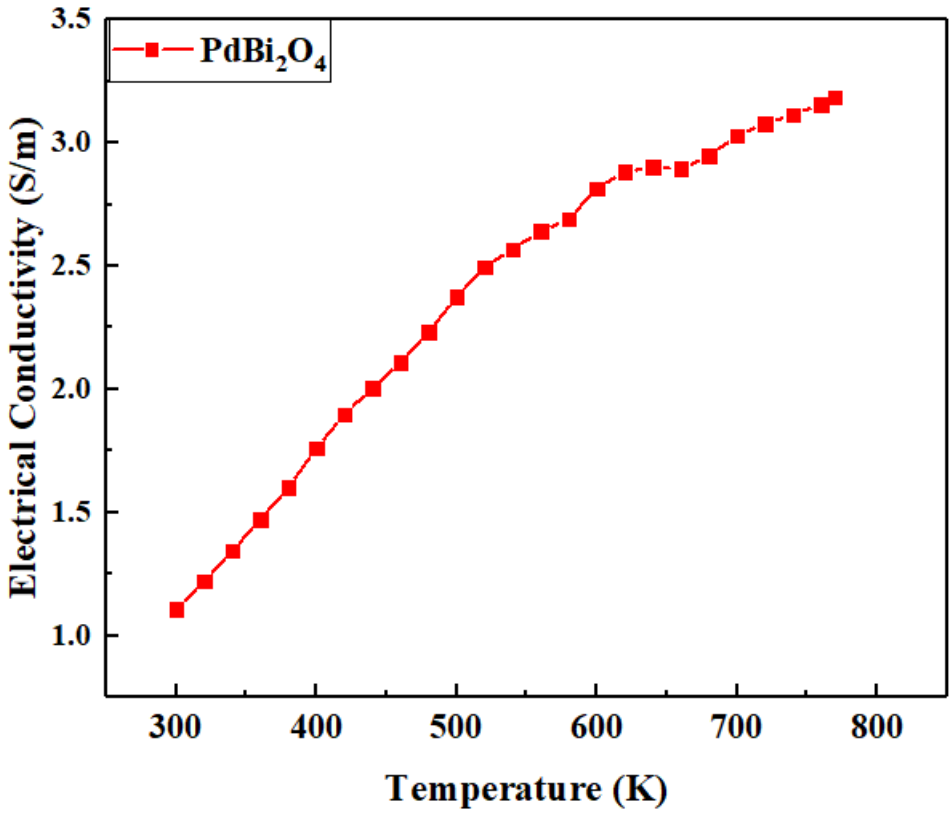

Figure 3.9 Temperature-dependent electrical conductivity of $PdBi_2O_4$

Thermal conductivity of $PdBi_2O_4$ shows a trend of increasing and then decreasing with increases temperature, shown in Figure 3.10**.** At lower temperatures the thermal conductivity of $PdBi_2O_4$ is low. Energy and phonon vibrations increase with a temperature increase, which results in an increase of group velocity that enhances thermal conductivity. However, as the temperature keeps increasing, more phonon scattering is observed from point defect scattering contributions, due to mass disorder and bond length disorder at higher temperature, and phonon-phonon Umklapp

scattering. These phenomena typically lead to decreased thermal conductivity with increasing temperatures as we observed in the figure. Theoretical work shows the decreasing trend with low lattice thermal conductivity. Due to the large anharmonicity caused by asymmetric distortion of BiO_6 octahedral, more phonons are scattered that significantly reduce thermal conductivity. Compared to the most common TE oxide material $Na_xCoO_{2-\delta}$ (~19 W/mK)[145], the lattice thermal conductivity of $PdBi_2O_4$ is almost two orders of magnitude lower.

The power factor and zT values are shown in Figure 3.11. Effective dopants are needed, such as Pb, for improving electrical properties of $PdBi_2O_4$ used as TE materials[146]. Although the current values are low, the structure of the material shows promise for use as a high performance p-type TE material.

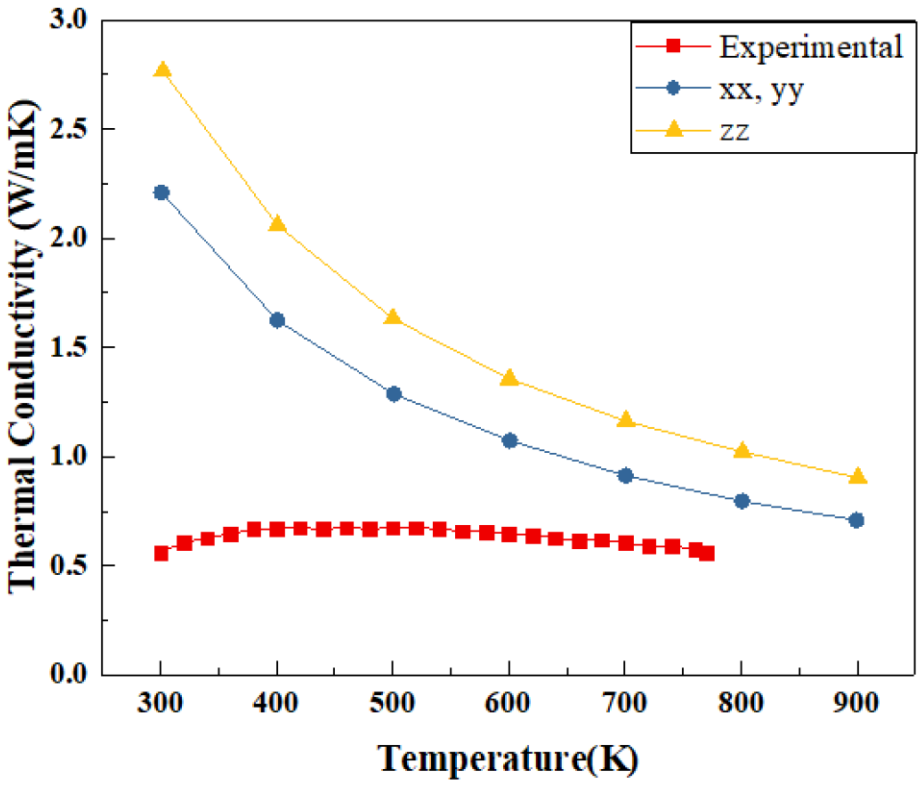

Figure 3.10 Temperature dependent thermal conductivity of $PdBi_2O_4$ experimental result vs. theoretical result

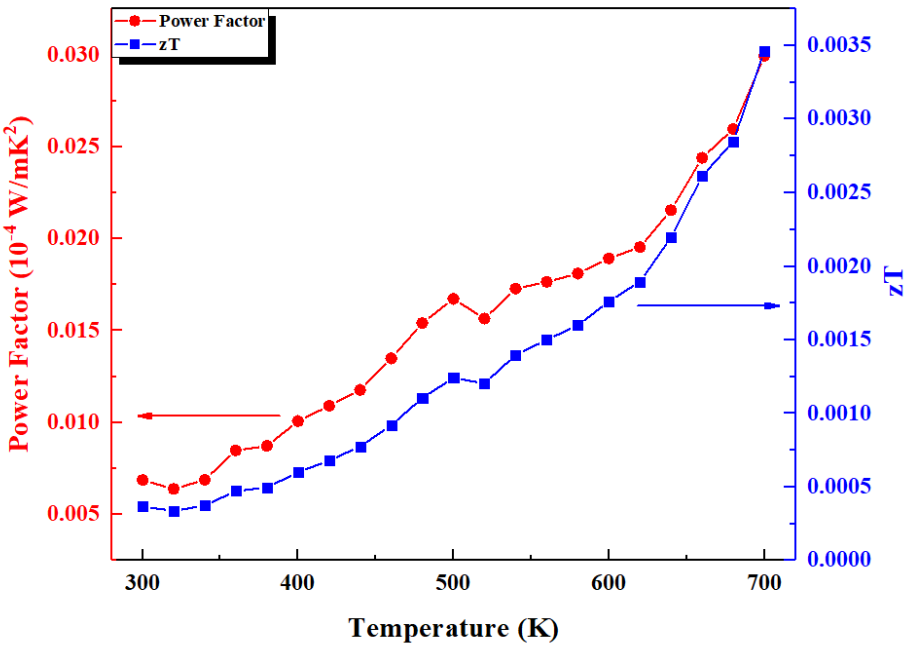

Figure 3.11 Temperature-dependent power factor and zT of $PdBi_2O_4$

3.2.4 Conclusions

In this work, we have investigated the temperature dependent thermoelectric properties of $PdBi_2O_4$ with a focus on the relationship between crystal structure and thermoelectric properties. The value of the Seebeck coefficient is positive over the measured temperature range, which shows p-type behavior, and it increases with the increase of temperature. The electrical conductivity increases as the temperature increases, indicating semiconductor behavior. The high density of states leads to a large Seebeck coefficient, however, the lower mobility and carrier concentration results in low electrical conductivity. The power factor based on Seebeck coefficient and electrical conductivity is reached at 3×10^{-6} W/mK^2 at 700K. Small nano grains in our samples have led to more phonon-phonon scattering without deteriorating electron transport, which results in low thermal conductivity.

$PdBi_2O_4$ has potential as a TE material if optimized dopants can be found. Also, the structure of this material has a high impact on its properties. Further investigations are needed for exploration of $PdBi_2O_4$ TE applications.

3.3 Strategies for Enhancement of Oxides Thermoelectric Properties

As discussed in previous two sessions, the current zT value for both oxides materials is still lower than expected. To reach to optimized zT, we need to know the doping/carrier concentration. A generalized b-factor approach[147], [148], using the experimentally measured Seebeck, electrical and thermal conductivities, carrier concentrations, and assuming a power law scattering exponent, r, given by Equation 3.9

$$l(E) = l_0\left[\left(E - E_C\right)/k_B T\right]^r \qquad 3.9$$

and a "total" b-factor given as,

$$b_{tot} \propto \frac{sT}{k_e + k_L}\left(k_B/q\right)^2 \qquad 3.10$$

An estimation for the doping/carrier concentration and fermi level that it's necessary to maximize zT for each sample (all samples in theory "should" fall on the same curve, however experimental realities prohibit this). The results are shown in Figure 3.12 and Figure 3.13, we assume acoustic deformation potential (ADP) scattering mechanism for all samples, r = 0.

All the experimental data (red circles) for $CuAlO_2$ at different temperature are left of the universal curve (dotted dashed line through blue circles), the blue circles represent maximum zT of the materials. The samples are under doped. The optimum fermi level ranges between 0.65 kT below and -0.5 kT above the valence band edge. The effective mass of $CuAlO_2$ is reported m^*=2.6 m_o[149]. The calculated optimum carrier concentrations range from 8.1E+17 cm^{-3} to 3.1E+18 cm^{-3} from temperature 300K-770K. The next step for improve zT for $CuAlO_2$ is looking for optimized dopants such as Fe_2O_3.

Similar trend is observed in Figure 3.13, all samples are under doped. The optimum fermi level ranges from 0.65 kT to -0.50 kT. To get the optimized carrier concentration, we need effective mass of $PdBi_2O_4$, which currently is not available since not many groups work on this. Further studies on this material will be needed for thermoelectric applications.

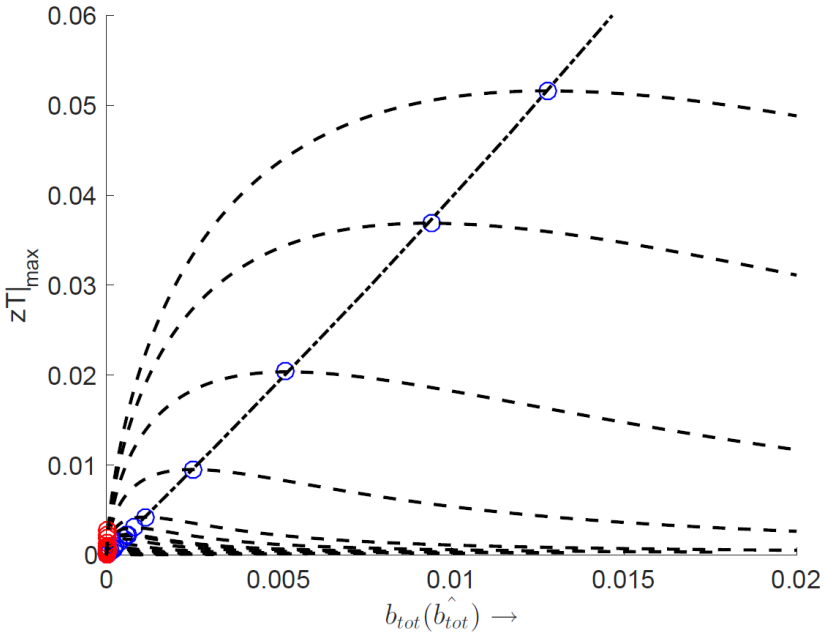

Figure 3.12 The experimental zT values (red circles) versus the total b-factor for ADP scattering at temperature 300K-770K for $CuAlO_2$. The optimum zT curve is shown as a dotted-dashed line in both plots, with the optimum zT value for each sample shown with blue circle on the optimum zT curve. The dashed line for each sample corresponds to the zT value if only the Fermi level is varied.

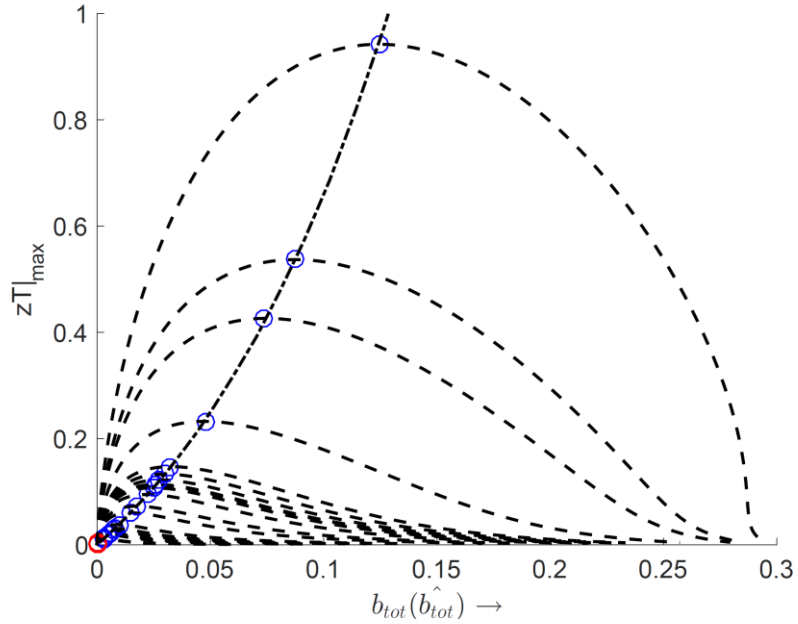

Figure 3.13 The experimental zT values (red circles) versus the total b-factor for ADP scattering at temperature 300K-700K for $PdBi_2O_4$

3.4 Fe doped Copper Aluminum Oxide-$CuAl_{1-x}Fe_xO_2$

Doping is one of the effective approaches for improving the TE efficiency of $CuAlO_2$ alloys by enhancing its electronic properties or reducing lattice thermal conductivity via additions of the point defects[150]–[153]. Several studies have investigated using different dopants to further enhance the TE properties of $CuAlO_2$ alloys. $CuAlO_2$ with partially Mg doping presented an improved electrical conductivity and lower thermal conductivity before the formation of highly insulating spinel phases. However, it was hard to control the doping level using solid-state methods such as hot pressing and pulsed electric current sintering techniques[154]. Sakulkalavek et. al reported an enhancement on electrical conductivity of p-type $CuAlO_2$ by Ag_2O addition caused by the increased carrier density[155]. As the interdependence of electrical and thermal conductivity, high electrical conductivity will lead to a increase of thermal conductivity. However, large value of thermal conductivity limited the broader application in thermoelectric. The Ca substitution in $CuAl_{1-x}Ca_xO_2$ up to x=0.1 showed an increased power factor contributes from both electrical conductivity and Seebeck coefficient[156]. Lack of the thermal conductivity study remains an uncertainty to conclude the effectiveness using Ca dopant. Another study on Cr substitution has been predicted to increase the density of states at the top of the valence band through DFT simulations, which showed the promise on electronic properties improvement[157]. Co-doping of two different substituents was also investigated to further increase the electrical conductivity. It was found that the power factor was substantially improved by the addition of both Ag and Zn that reaches a value of 1.26×10^{-4} $Wm^{-1}K^{-2}$ 1060K [158]. The result is similar to the study on the effects of Fe addition. Park et al. reported that Fe addition up to x = 0.1 significantly increased power factor because of significant increase in electrical conductivity. The highest value measured was 1.1×10^{-4} W/mK^2 for x = 0.1 at 1140K[159]. Also, several other studies on Fe doping showed the feasibility in the enhancement of power factor caused by increased carrier density[160]–[162]. However, most were only studied on materials synthesis and electronic transport properties. The systematical study on both electrical and thermal properties of Fe-doped $CuAlO_2$ is still missing in this area.

Thus, we have conducted experiment of TE properties of Fe-doped $CuAlO_2$ with the function of temperatures from 300K to 780K. Using similar materials synthesis method as $CuAlO_2$ to produce $CuFe_xAl_{1-x}O_2$ (x=0.05, 0.1, 0.2). The effects of different annealing temperature and time for $CuFe_xAl_{1-x}O_2$ on resulting microstructure, and related thermoelectric properties were

studied. Also, we used b-factor results as a guidance to compare optimized carrier concentration for achieving maximum power factor.

3.4.1 Materials Synthesis

Fe-doped samples of $CuAl_{1-x}Fe_xO_2$ (x=0.05, 0.1, and 0.2) were stoichiometrically mixed using Al_2O_3, CuO, and Fe_2O_3 powder with alcohol using solid-state method by ball milling. The ball milled blurry were dried at 100˚C overnight then annealed at different temperature and duration in air. The resultant powders were cold pressed into pellets with 13mm diameter and 2mm thickness.

3.4.2 Sample Characterization

The phase composition of as-annealed powders was analyzed via powder X-ray diffraction (XRD; Panalytical Empyrean) using Cu Kα radiation with Bragg-Brentano mode at 40kV and 40mA. The microstructure of as-annealed powders was investigated by a scanning electron microscope (SEM; FEI Nova NanoSEM). The elements dispersion of the $CuAl_{0.9}Fe_{0.1}O_2$ sample was observed by energy dispersive X-ray spectrometer (EDS).

The details of temperature dependent Seebeck coefficient was determined through a home-built measurement system in a vacuum chamber as described in our previous publications[163], [164]. The S was calculated from the slope of temperature vs voltage. Temperature dependent electrical conductivity was directly measured by hall effect using Van der Pauw method (Ecopia AHT55T5). The thermal conductivity was calculated via $\kappa = \rho C_p D$, where $C_p$is the measured specific heat and D is the measured thermal diffusivity by laser flash method (LFA 467, NETZSCH, Germany) using transient time-dominant method. All the TE properties were measured from 300K to 780K in a nitrogen environment. The uncertainty of each measured transport property is about 5%.

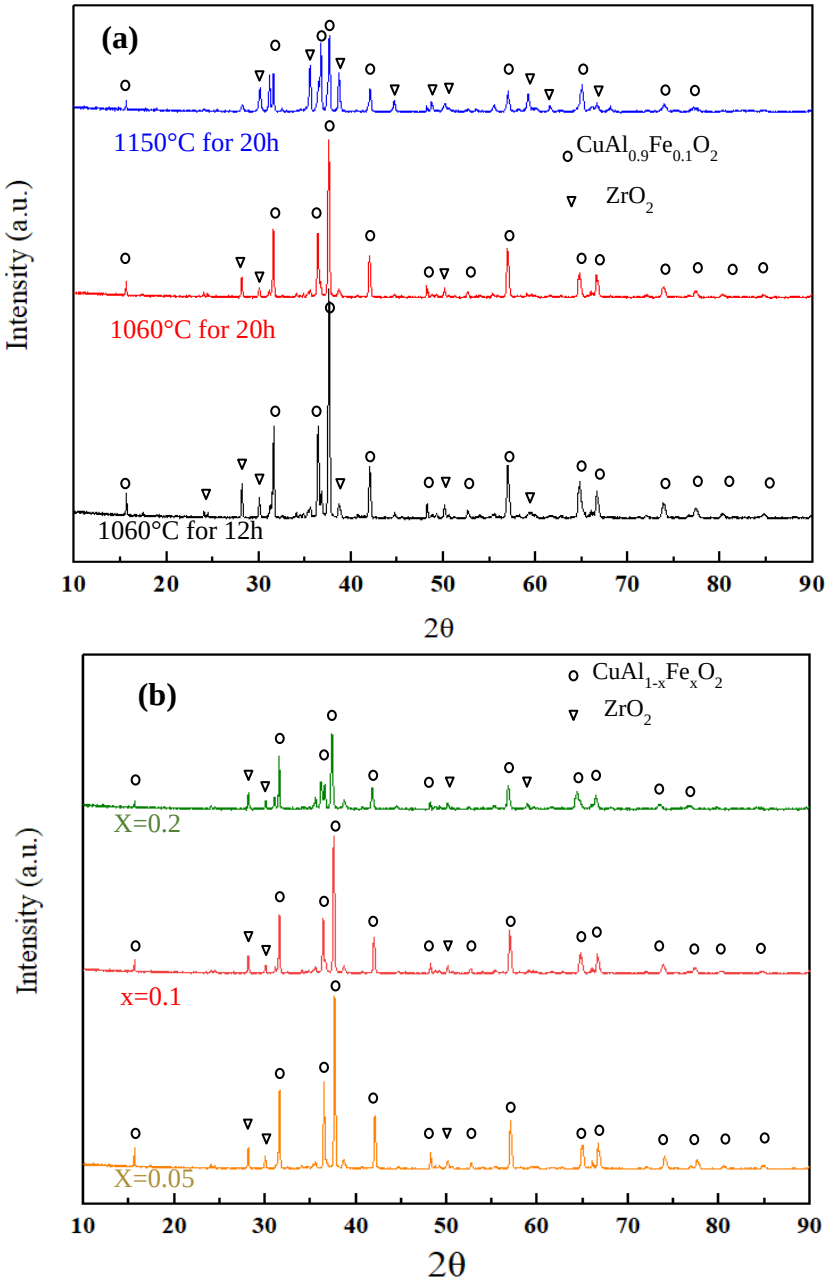

Figure 3.14. XRD patterns of phase composition and crystal structure study for $CuAl_{1-x}Fe_xO_2$ powders. (a) $CuAl_{1-x}Fe_xO_2$ under different annealing temperature and time; (b) stoichiometric $CuAl_{1-x}Fe_xO_2$ powders annealed under 1060°C for 20h in air.

The experiments on different annealing temperature and time have been conducted in order to determine the optimized growth conditions for $CuAl_{1-x}Fe_xO_2$ samples. The crystallinity of as-annealed $CuAl_{0.9}Fe_{0.1}O_2$ powders is investigated by XRD. All the samples are polycrystalline as patterns shown in Figure 1 (a). The main peaks in samples could be indexed to rhombohedral phase (Space group of *R3m*). The measured lattice parameters are in good agreement with the computational results for this material[159]. Monoclinic baddeleyite (ZrO_2) is detected as a unique zirconia phase in all composite samples, in accordance with the phase diagrams. Annealing at 1060°C for 12 hours leads to the raw materials are not fully reacted, on the other hand, annealing at 1150°C for 20 hours results in secondary phase in the samples, as shown in Figure 3.14 (a) back and blue line, respectively. High phase purity of the sample is obtained by annealing the materials at 1060°C for 20 hours in air, as shown in red line, Figure 3.14 (a).

The different Fe doped $CuAl_{1-x}Fe_xO_2$ powders have been synthesized followed the stoichiometric equation as shown below. The powders with different Fe doping concentration have been annealed at 1060°C for 20h in air for enhanced phase purity. The resulted XRD patterns are shown in Figure 3.14 (b). All the main peaks agree well with the rhombohedral structure that indicated high phase purity. The width of XRD peaks decreases with the increase of Fe doping concentration. This is due to the grain size grows as the addition of Fe_2O_3. The optimized Fe doping concentration will be determined by measuring materials thermoelectric properties.

$$CuO + (1-x)/2\, Al_2O_3 + x/2\, Fe_2O_3 \rightarrow CuAl_{1-x}Fe_xO_2 + 1/4\, O_2 \qquad 3.11$$

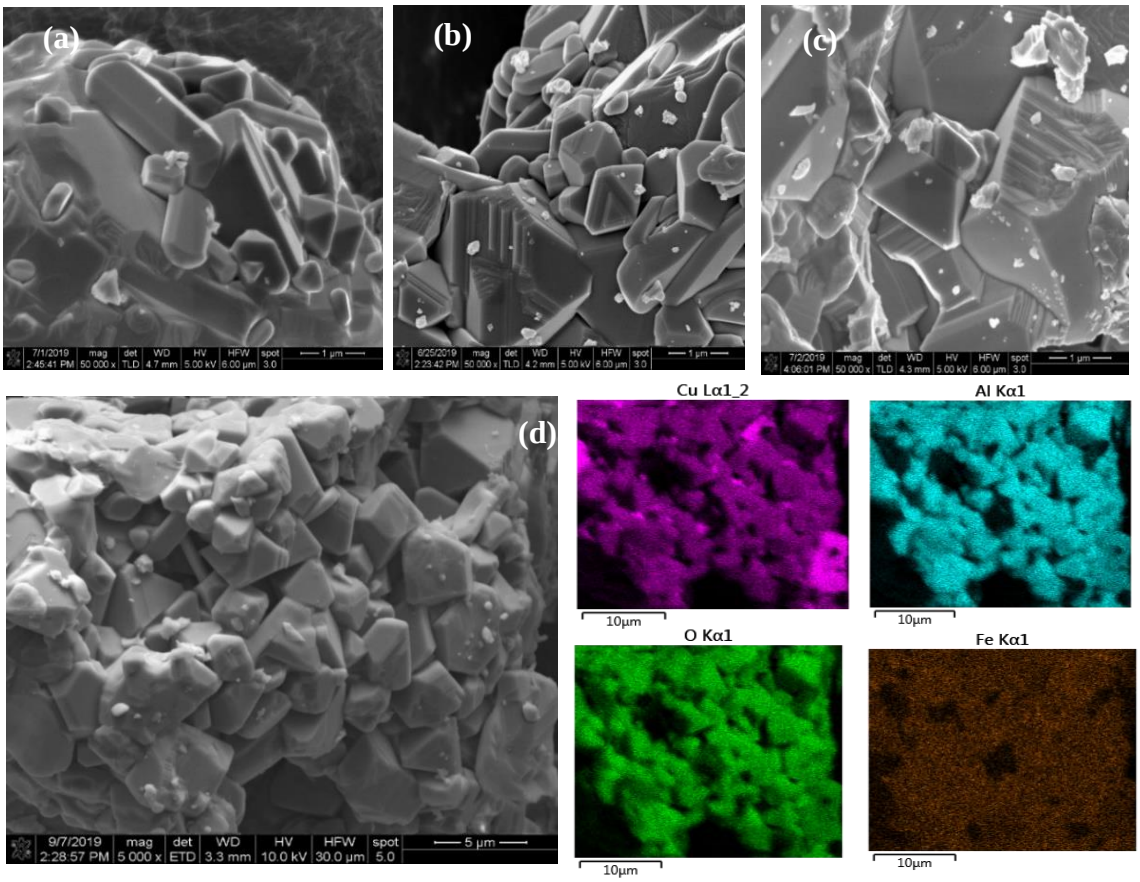

Figure 3.15. SEM micrographs of stoichiometric $CuAl_{1-x}Fe_xO_2$ powders annealed under 1060°C for 20h in air (a) $CuAl_{0.95}Fe_{0.05}O_2$; (b) $CuAl_{0.9}Fe_{0.1}O_2$; (c) $CuAl_{0.8}Fe_{0.2}O_2$; (d) EDS element maps for as-annealed $CuAl_{0.9}Fe_{0.1}O_2$ powder.

Figure 3.15 shows SEM micrographs of powder sample $CuAl_{1-x}Fe_xO_2$. The grain size increases from 0.8 μm to 2.5 μm as the amount of Fe in the $CuAl_{1-x}Fe_xO_2$ samples increases. When x=0.2, the grain size is much larger compared to others as shown in Figure 3.15 (c), which agrees with the XRD results as discussed above. There are few small particles attached on the surface of $CuAl_{1-x}Fe_xO_2$ powders that are ZrO_2 residuals during ball milling process as observed in SEM images. It is also observed ZrO_2 peak in XRD results. The phase composition of annealed $CuAl_{0.9}Fe_{0.1}O_2$ powder was analyzed by SEM/EDS, as shown in Figure 3.15(d). The element mapping of the sample shows uniformly distributed in the annealed powders, presented high phase purity of the samples. The atomic ratio for Cu: Al: O = 1:1:4.

3.4.3 Thermoelectric Properties

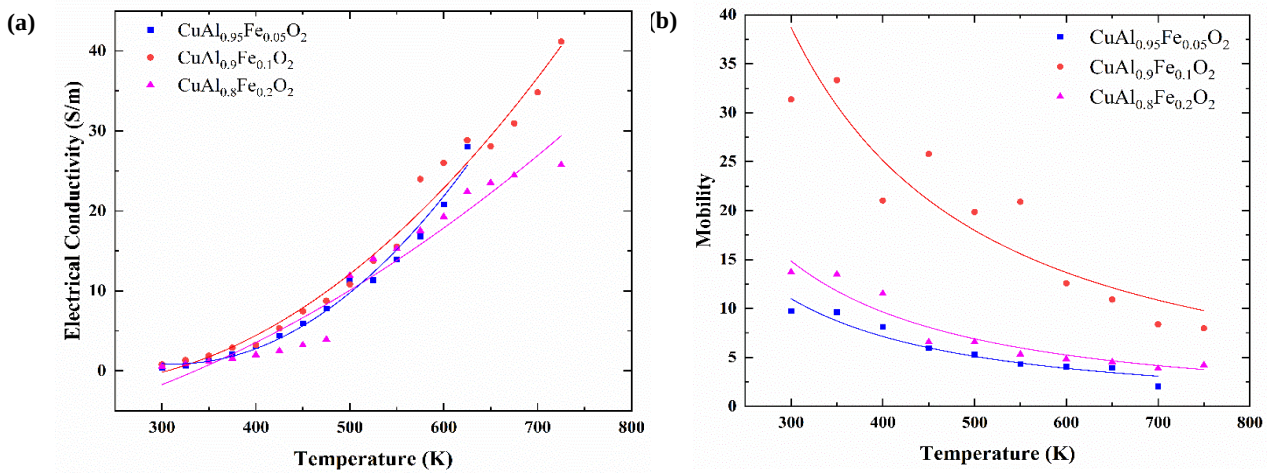

Figure 3.16 Temperature dependent (a) electrical conductivity (σ) and (b) mobility (μ) of $CuAl_{1-x}Fe_xO_2$ (x=0.05, 0.1, and 0.2)

The electronic transport properties of pressed pellets have been conducted by Hall measurement using four-point probe method. Temperature dependent electrical conductivity and mobility results of $CuAlO_2$ with different Fe doping concentration are shown in Figure 3.16 (a). Overall, electrical conductivity increases with the increase of temperature showing semiconductor behavior. With the increasing temperature thermal energy excites more free electrons hopping from the valence band to the conduction band resulting in the enhanced electrical conductivity. Compared to the electrical conductivity of undoped $CuAlO_2$ is about 17 S/m at 780K[164], Fe doping $CuAlO_2$ shows nearly three times higher value ~45 S/m at same temperature. The addition of Fe dopant effectively increases free electrons that enhances the carrier concentration, which contributes to the higher electrical conductivity. It is notable to see that Fe doping composition at 0.1 is the optimized doping concentration that reach high electrical conductivity over the temperature. This may be due to the higher value of the mobility as shown in Figure 3.16 (b). The relationship between electrical conductivity and mobility is shown in Equation 2.4.

With the addition of Fe up to x=0.1, the increase of the density makes a more significant contributions in the reduction of scattering process that enhances the mobility. To understand the different scattering mechanisms, the scattering factor can be obtained from the relationship between hall mobility and temperature, as shown below:

$$\mu \propto T^{-3/2+r} \qquad 3.12$$

In Figure 3.16 (b), temperature dependent mobility for $CuAl_{1-x}Fe_xO_2$ shows a rough trend of $\mu \sim T^{-1.5}$ over the entire temperature range. This indicates that acoustic deformation potential scattering (ADP) with r= 0 has dominated scattering mechanism. However, the electrical conductivity of $CuAl_{0.8}Fe_{0.2}O_2$ is lower. This is due to the fact that Fe_2O_3 has low electrical conductivity. The addition of Fe content is greater than 0.2, the overall electrical conductivity will decrease due to the low mobility.

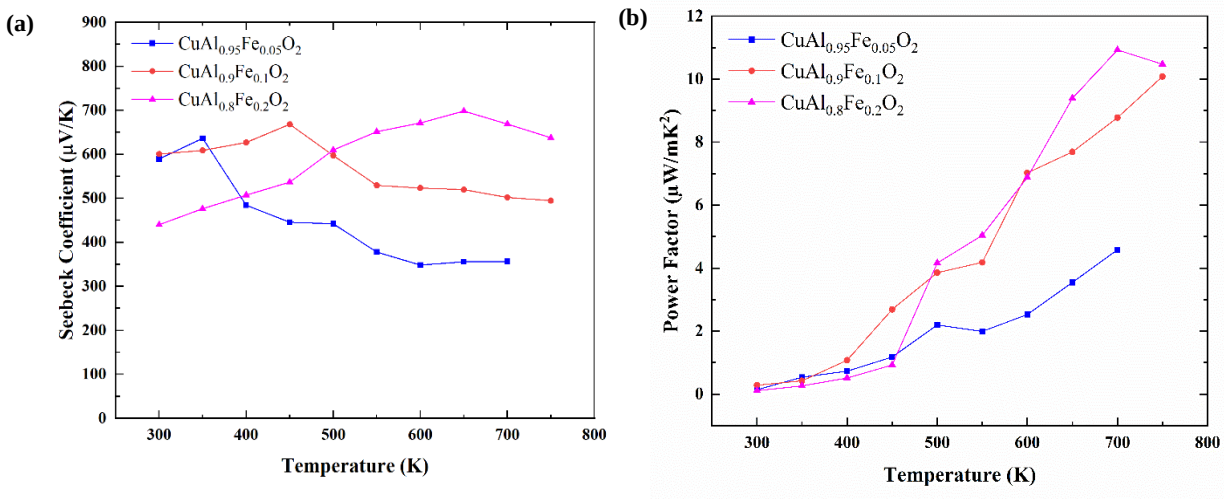

Figure 3.17 Temperature dependent (a) Seebeck coefficient (*S*) and (b) power factor (PF) of $CuAl_{1-x}Fe_xO_2$ (x=0.05, 0.1, and 0.2)

Due to the interdependence nature of all TE parameters (S, σ, k), high electrical conductivity does not guarantee better TE performance as the Seebeck coefficient may be deteriorated. Figure 3.17 shows the temperature-dependent Seebeck coefficient of $CuAl_{1-x}Fe_xO_2$ (x=0.05, 0.1, and 0.2). The sign of the Seebeck coefficient is positive, indicating majority carriers are holes and present p-type behavior. The Seebeck coefficient values of $CuAl_{1-x}Fe_xO_2$ (x=0.05, 0.1, and 0.2) increases with the increasing temperature and then decreases. In general, the value of the Seebeck coefficient decreases due to the increase of carrier density.[165] An increase of carrier concentration leads to an increase in electrical conductivity, but a decrease in Seebeck coefficient. The relationship between the Seebeck coefficient as a function of carrier concentration and scattering factor is shown as:

$$S \approx r - \ln n \qquad 3.13$$

where r is the scattering factor and n is the carrier concentration.

The increasing carrier concentration by doping Fe enhances the electrical conductivity but simultaneously deteriorates the Seebeck coefficient. The Seebeck coefficient value of $CuAl_{0.9}Fe_{0.1}O_2$ is higher than $CuAl_{0.8}Fe_{0.2}O_2$ and $CuAl_{0.95}Fe_{0.05}O_2$ below 500K due to the low carrier concentration (n =5×10^{16} cm $^{-3}$). In addition the value of the Seebeck coefficient for $CuAl_{0.8}Fe_{0.2}O_2$ is higher above 500K owing to a large amount of second phase Fe_2O_3 formed in high temperature with a large Seebeck coefficient.

The PF is found to increase with increasing temperature, as shown in Figure 3.17(b). For power generation applications where the heat source is unlimited, PF of the TE materials may be more important parameter than the zT. $CuAl_{0.8}Fe_{0.2}O_2$ shows highest PF value of 11 μW/mK^2 at 700K, which is one order magnitude higher than undoped $CuAlO_2$ in previous study[164]. Adding Fe dopants increases electrical conductivity without degrading Seebeck coefficient too much that contributes to high PF of $CuAl_{0.8}Fe_{0.2}O_2$. High purity of the samples and annealing process as we discussed above are critical steps to ensure the high electrical performance of the TE materials.

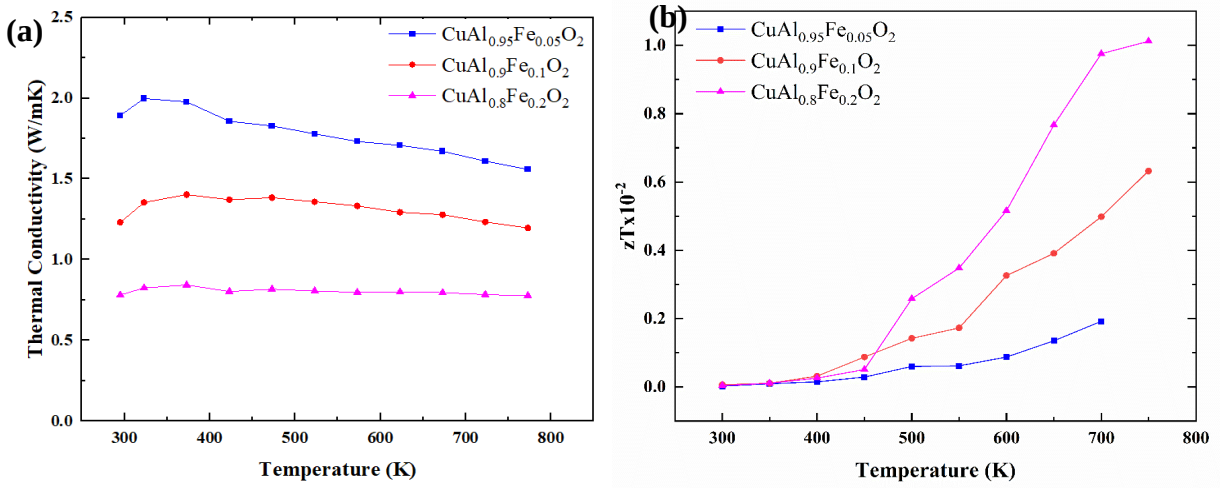

Figure 3.18 Temperature dependent (a) thermal conductivity (k) and (b) figure of merit (zT) of $CuAl_{1-x}Fe_xO_2$ (x=0.05, 0.1, and 0.2)

One of the strategies to enhance the efficiency of TE materials is to minimize thermal conductivity. Total thermal conductivity (κ_T) consists of the contributions from both electron and phonon transport, defined as follow:

$$\kappa_T = \kappa_e + \kappa_l \quad 3.14$$

where electronic contribution can be approximately estimated by $\kappa_e = L\sigma T = ne\mu LT$, L is the Lorenz factor (2.45×10^{-8} J^2 K^{-2} C^{-2}) and lattice contribution κ_l. Owing to a low κ_e, κ_T largely comes from the lattice contributions for bulk semiconductor materials.

Temperature dependent total thermal conductivity of $CuAl_{1-x}Fe_xO_2$ (x=0.05, 0.1, and 0.2) is shown in Figure 3.18(a). For different Fe concentration, samples show similar trend on temperature dependent thermal conductivity. At low temperature, the thermal conductivity increases due to the group velocity enhancement caused by lattice vibrations. At higher temperature, more scattering occurs as phonon-phonon Umklapp scattering may dominate process. It shows the decrease trend of thermal conductivity. With the Fe incorporation increasing, lattice thermal conductivity reduces over the entire temperature range. As the mass difference exists between Al and Fe, the phonon scattering can be intensified by the alloys and defects. Thus, $CuAl_{0.8}Fe_{0.2}O_2$ presents the lowest thermal conductivity ~0.776W/mK at 773K. This value is much lower than conventional thermoelectric material such as BiSbTe.[166] This ultra-low thermal conductivity shows the feasibility for $CuAl_{0.8}Fe_{0.2}O_2$ using as p-type thermoelectric material.

The zT values for $CuAl_{1-x}Fe_xO_2$ (x=0.05, 0.1, and 0.2) are shown in Figure 3.18 (b). It is found that zT increases with the temperature increasing. Because Fe doping can enhance the power factor and lower thermal conductivity of $CuAlO_2$, the sample $CuAl_{0.8}Fe_{0.2}O_2$ has the maximum zT value of 1.2×10^{-2} at 750K. This value is one order magnitude improvement than that of undoped $CuAlO_2$ reported previously.[164] Further strategies for the zT enhancement: (1) using simulation tool to predict the optimized doping concentration for $CuAl_{1-x}Fe_xO_2$ as the guidance for experiments. The predicted power factor can be used as a baseline to compare; (2) further control nanostructure of the sample to ensure the thermal conductivity will remain as low as possible. Thus, higher zT will be reached by optimizing carrier concentration with high power factor and low thermal conductivity.

3.4.4 Conclusions

In this work, thermoelectric properties of Fe doped $CuAlO_2$ are systematically investigated. Both XRD patterns and SEM/EDS results reveal that high purity and uniformly distributed $CuAl_{1-}$

$_xFe_xO_2$ samples with a rhombohedral structure obtained when annealed at 1060°C for 20 hours in air. The addition of Fe is x=0.2 has improved power factor contributes from high Seebeck coefficient. Also, it results in an ultra-low thermal conductivity of 0.776W/mK at 773K due to the enhanced phonon scattering mechanism. As a result, the highest zT value 1.2×10^{-2} was attained for $CuAl_{0.8}Fe_{0.2}O_2$ at 750K. Fe doping method was effective for enhancing thermoelectric properties of $CuAlO_2$.

4. CONFORMAL THERMOELECTRIC DEVICE DESIGN AND FABRICATION

This chapter contains portions of a previously NSF report with project title: Developing a self-powered pipeline sensing and monitoring system. Federal grant number: 1919191.

4.1 Thermoelectric Device Design

4.1.1 Co-optimization of TEG Device Electro-thermal Properties

The TEG device performance (power output and efficiency) relies on the materials zT enhancement also works as a system that affected by heat transfer from heat source to heat sink. It works as the whole energy conversion system that need to be electrically and thermally optimized. Yazawa et. al has developed electro-thermal co-optimized TEG modeling that can be used as a guideline for this study [167]. There are two ways to look into the performance of TEG, either maximum output power or highest efficiency. This depends on different applications, such as for power generations where the heat source is continuous and unlimited, the maximum power output is more important than efficiency. On the other hand, higher efficiency is important for cooling as it needs convert more heat into the electricity. For modeling optimization, the highest output corresponds to the highest power delivered to a load. The highest efficiency corresponds to the highest ratio of electrical power delivered to load to the amount of heat flux from the hot reservoir to the cold reservoir.

As the electrical and thermal properties are interdependent, it is important to analyze the electrical current flow and heat flow simultaneously. The system diagram that includes both thermal resistance and electrical circuit as shown in Figure 4.1.

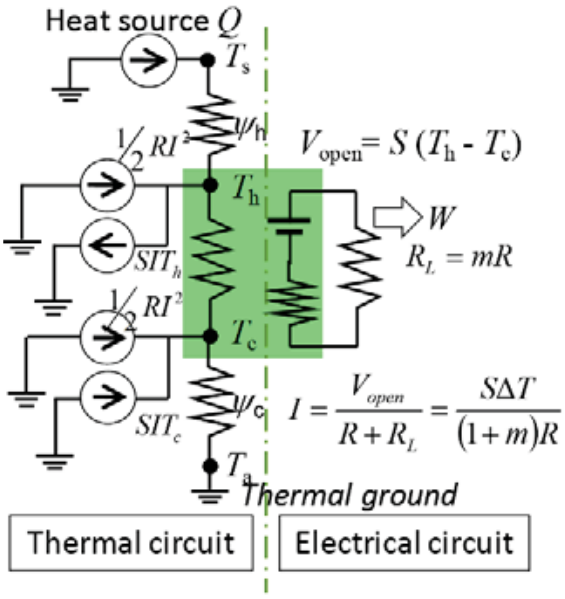

Figure 4.1 Electro-thermal resistance network model. The green block represents the thermoelectric material (leg) and the upper and lower side of the region represent the electrical and thermal contacts. ψ_h and ψ_c are the thermal resistances for the heat transfer on the hot side and cold side, respectively. q_h is the heat flux supplied by the hot reservoir at temperature T_s (fixed). q_c is heat flux which flows into the cold reservoir is reduced from q_h depending on the energy conversion efficiency [168].

The equations at two nodes are based on the energy conservation, T_h and T_c are the temperatures at the hot side and the cold side of the thermoelectric legs.

$$q_h = \frac{\beta}{d}(T_h - T_c) + SIT_h - I^2R/2 \tag{4.1}$$

$$q_c = \frac{\beta}{d}(T_h - T_c) + SIT_c + I^2R/2 \tag{4.2}$$

where, β is the thermal conductivity, S is the Seebeck coefficient, I is the electrical current, and R is the thermoelectrical internal (electrical) resistance. Both hot and cold junctions dissipate half of the total power as the Joule heating happens in TE leg. The out power delivered to the load per unit area of the heat source w [W/m^2] is found as[167]:

$$w = I^2mR = \frac{m\sigma S^2}{(1+m)^2 d}(T_h - T_c)^2 \tag{4.3}$$

where, $w = q_h - q_c$ by energy conservation, σ is the electrical conductivity of the leg, and m is the ratio of the internal resistance to the external load resistance, i.e., $R_L = mR$.

The maximum power output as a function of T_s and T_a can be calculated as[167]:

$$w = \frac{mZ}{\alpha^2(1+m)^2}\frac{\beta}{d_{opt}}(T_s - T_a)^2 \qquad 4.4$$

where $\alpha = (T_s - T_a)/(T_h - T_c)$, d_{opt} is the optimum leg length. If the TE legs are thin and long, it can hold a large temperature different. However, the electrical resistance increases for long legs and the power output will decrease. Thus, there is an optimized leg length that yield a maximum power output, where the ratio of internal and external resistance $m = \sqrt{1+zT}$.[168]

4.1.2 Design Parameters Optimization

In general, the TEG conversion efficiency is the essential measure of performance. However, for power generation application where the waste heat is unlimited, it is rather important to maximize the power output for device performance. Thus, we focus on using cTEG for underground pipeline monitoring system in this study. Figure 4.2 shows the diagram of using TEG for powering underground steam pipe The conformal TEG was wrapped around the exterior of a steam pipe. The steam temperature is fixed at 200˚C and the ambient temperature is 27 ˚C.

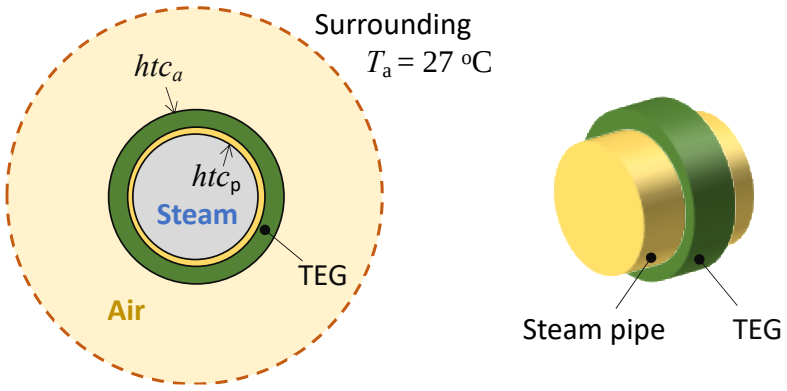

Figure 4.2. Diagram of the TEG powered underground steam pipe in cross-section view and the overview of the structure. (Reproduce from NSF report).

As we discussed in the previous section, the optimized power output can be determined by optimum leg thickness and fill factor. The fill factor F refers to the ratio of the active TE material area to the total device area, which represents as:

$$F = \frac{N \times A_{leg}}{A_{sub}} \qquad 4.5$$

where N is the pairs of TE legs, A_{leg} is the area of TE legs, and A_{sub} is the total area of TE module substrate.

The simulated optimum fill factor and power output versus leg lengths are shown in Figure 4.3. The cold side is not connected with heat sink in this result. The fill factor and leg length show linear relationship under optimized power output condition. For flexibility of the cTEG in this application, we set a maximum module thickness of 5 mm as the threshold, which indicates that the maximum fabricated the leg length is 5 mm. The fill factor is 0.061 when the leg length is 5mm as shown in Figure 4.3. The power output increases and then reaches threshold with the increase of leg length. Under certain range of the fill factor, the longer leg length, the larger power output can be generated from the device. However, the longer leg length of the thermal elements, the larger resistance of the device with higher fill factor. Thus, the power output reaches maximum results as shown in green curve.

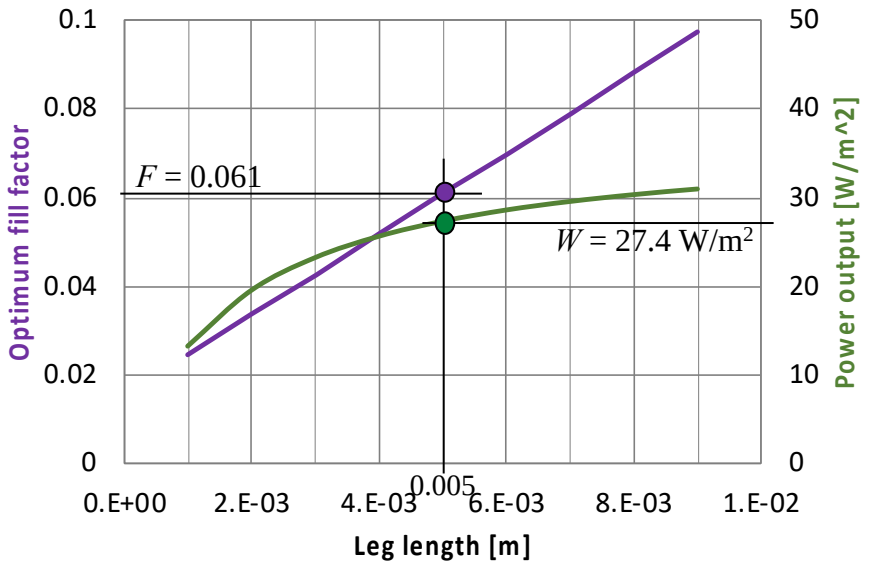

Figure 4.3. Power output and optimum fill factor as the functions of leg length with no heat transfer enhancement on the cold side (Reproduce from NSF report).

Figure 4.4 shows the comparison simulated results for power output under different leg length. With optimum leg length as shown in blue curve, the power output increases with the enhancement of the fill factor. The maximum power output can be reached up to 48 W/m^2 with a pin-fin enhancement of cTEG. However, if we fixed a leg length of 5mm, the power output increases and then decreases with the increase of the fill factor. The peak power output is 35.6 W/m^2 with a pin-fin enhancement of cTEG. The fill factor is 7.15%. On the hand, without treated surface of cTEG, the maximum power output is 27.4 W/m^2 with fill factor of 6.1% as shown in green dotted curve. From manufacturing standpoint, it is very challenging to maintain electrical and thermal contacts under small fill factor. Thus, this simulated results only provide the baseline for cTEG prototype development and the fill factor will be adjusted based on real manufacturing process that will be discussed in the next section.

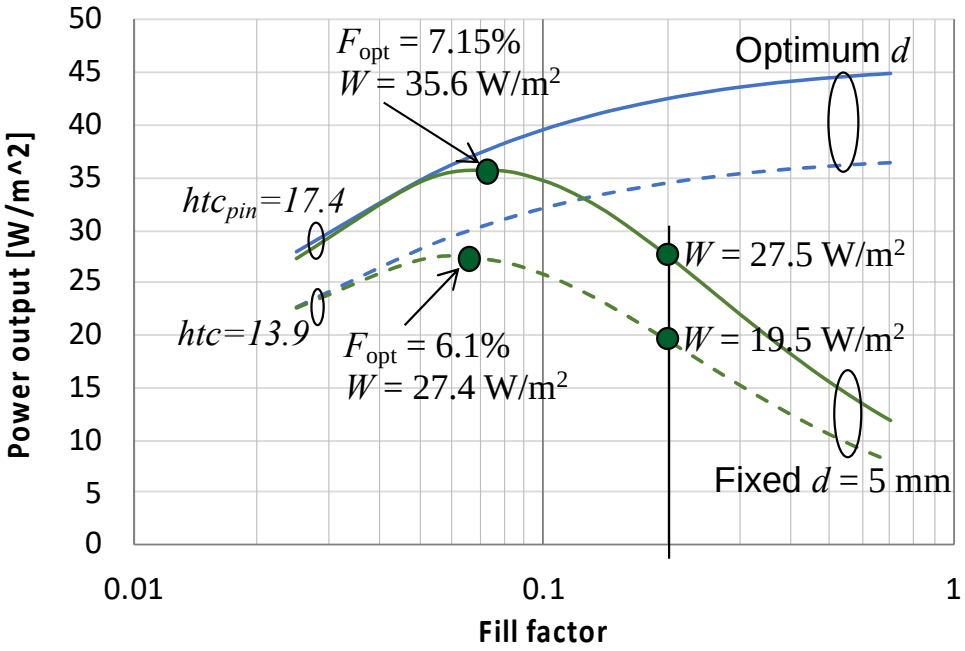

Figure 4.4. Power output as function of fill factor for the cases of fixed leg length (5mm) and variable leg length optimum for the maximum power output. The dotted curves show untreated surface (heat transfer coefficient of htc = 13.2 W/m^{2}K), and the solid curve shows the case with a pin-fin enhancement (heat transfer coefficient of htc = 17.4 W/m^{2}K) (Reproduce from NSF report).

4.1.3 Market Analysis for Thermoelectric Device

In district energy plants pressurized steam ranging from 230-370°C is sent into the pipeline distribution system for long distance energy transmission[169]. Depending on the thickness of insulation, close to 15- 20% of heat[170] is lost which can be directly converted into electricity using solid-state TE devices via the Seebeck effect[171]. Also, due to the lack of reliable power sources, district energy plants do not currently have the means to continuously monitor the pressurized steam in pipelines. This has resulted in many incidents causing severe injuries and extensive property damage. For instance, there was a steam pipe explosion on Fifth Avenue, Manhattan, one of the busiest districts in NYC, thousands of people were evacuated from 49 nearby buildings and also subway systems were disrupted[172]. Another one happened in downtown Baltimore, a steam pipe exploded that caused five injuries and damaged city infrastructures[173].

These accidents are avoidable if cost-effective continuously monitoring technology is available. The technology can be extended to the oil & gas industry where the ability to deploy cTEG powered sensors in remote or difficult-to-access pipelines (e.g. underground and in remote locations) will greatly reduce the costs associated with pipeline monitoring and maintenance. This technology is vital to ensure the safety, security, and productivity of our nation's infrastructure operations.

As shown in Table 1, the U.S. has 6000 district energy systems operating over 50,000 miles of steam pipelines[174]. Also, cTEG technology can be easily extended to other pipeline monitoring and service industries such as HVAC in commercial and residential buildings, etc.

Table 4.1 The total length of underground pipes in both markets

	Total underground pipeline (miles)	oil & gas pipeline (miles)	steam plant pipeline (mile)
United States	1,654,214	1,596,214	58,000

4.2 Conformal Thermoelectric Device Fabrication

4.2.1 Concept for Roll-to-roll Prototype Development

Conventional TE devices are plate-like and rigid, and unable to fully exploit thermal gradients (ΔT) from curved or nonplanar surfaces, as most heat sources have non-planar surfaces or spatial restrictions. To overcome the challenge described above, the last part of my thesis is to develop a conformal thermoelectric generator (cTEG) using several micro-deposition processes on a roll-to-roll platform, Figure 4.5.

The specific activities include: (1) depositing top metal contact layers using screen printing techniques; (2) creating micro-porous channels on polymer substrates using pulsed laser irradiation system; (3 & 4) filling of micro-channels with p- and n-type TE materials using pipet dispensing systems or similar technique for nanoparticles depositions; (5) sintering p- and n-type TE materials using pulsed laser or microwave for in-situ crystallization with minimal thermal damage, followed by (6) screen printing the top layer metal contacts to achieve high power output of cTEG as power sources for sensors.

Additionally, using highly insulating polymers (i.e., PDMS, polyamide, etc.) as the substrate and insulating materials between p-n legs, helps to avoid thermal losses. This novel device design will provide high efficiency and good mechanical stability to cTEG during the temperature cycle and mechanical bending process. The number of p-n pairs will be determined by the required power output for specific applications. The length of p- and n- legs, and the width and thickness of contacts will be determined based on the expected power output, the temperature gradient, and the material's thermoelectric performance for specific applications.

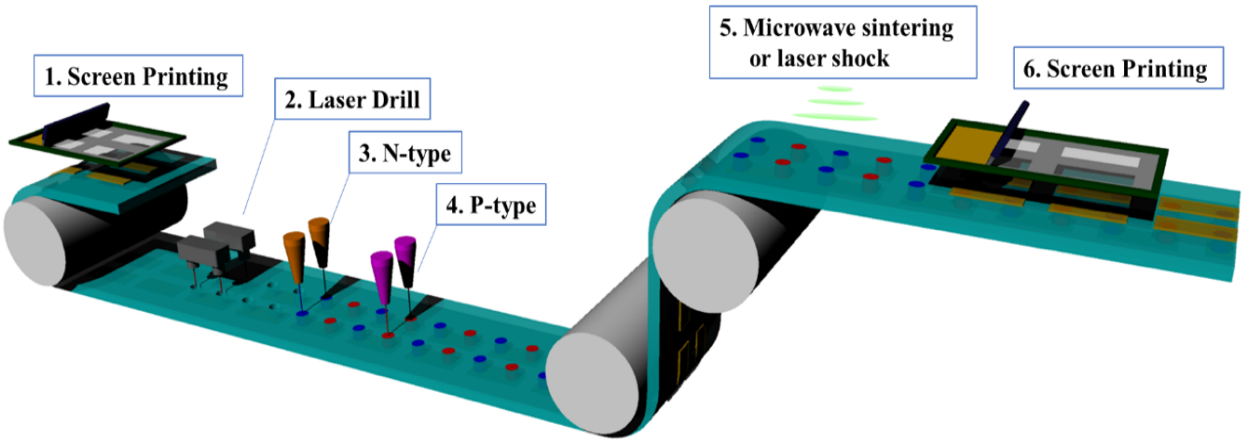

Figure 4.5 Schematic of the proposed roll-to-roll production line of a conformal thermoelectric generator (cTEG) as described in this project.

4.2.2 Prototype Development

Figure 4.6 (a) shows the simplified fabrication process of cTEG prototype development. The cTEG fabricated using conventional TE legs with flexible substrate and PDMS as filling materials. To achieve electrical connections, the flexible printed circuit board (FPCBs) were attached to the top and bottom of cTEG. The silver pattern is printed on the FPCBs by using Inkjet printer with different fill factor design as the metal interconnector between the TE legs. By pouring PDMS into the mold and curing 2 hours at 80˚C to serve as insulating materials. The fabricated TEG included 40 pairs n- and p-type legs on a 40 mm×40 mm area. Figure 4.6 (b) shows the fabricated cTEG and its flexibility.

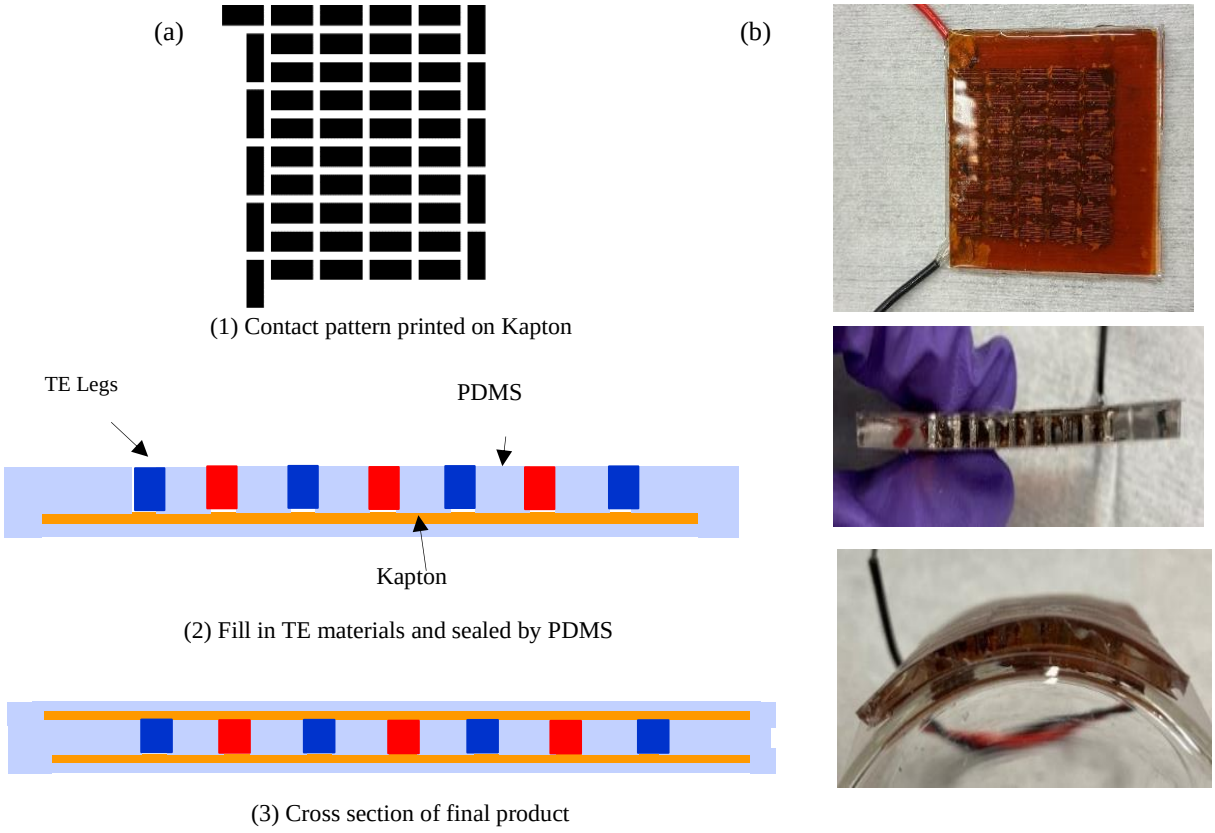

Figure 4.6 Fabrication process and cTEG prototype (a) simplified fabrication process of cTEG; (b) images of cTEG prototype

4.2.3 Device Measurement Setup

The chillers generate water flows to control the cold and hot side temperatures within ±0.1˚C accuracy (Fisher Scientific ISOTEMP 250LCU) [168]. The cold side is mostly fixed to 5 ˚C during this experiment. The hot side increases from 5˚C up to 55˚C. The flow meters (FTB333D, Omega Engineering) measure the water flows from chiller to testing bed with ±6% accuracy for 0.2-2 mL/min range. The amount of the heat extracted is considerably small compared the main heat flow. The overall view of setup as shown in Figure 4.7 (a).

Figure 4.7 (b) shows the side view of sample stage where TE module is placed between copper plates. The thermal interface grease (OMEGA THERM 201) is used on top and bottom sides of TE module to have a better contact. Due to the connections between TE legs, the measured TE modules contains 4 pairs of the TE legs in a 40mm ×40mm area.

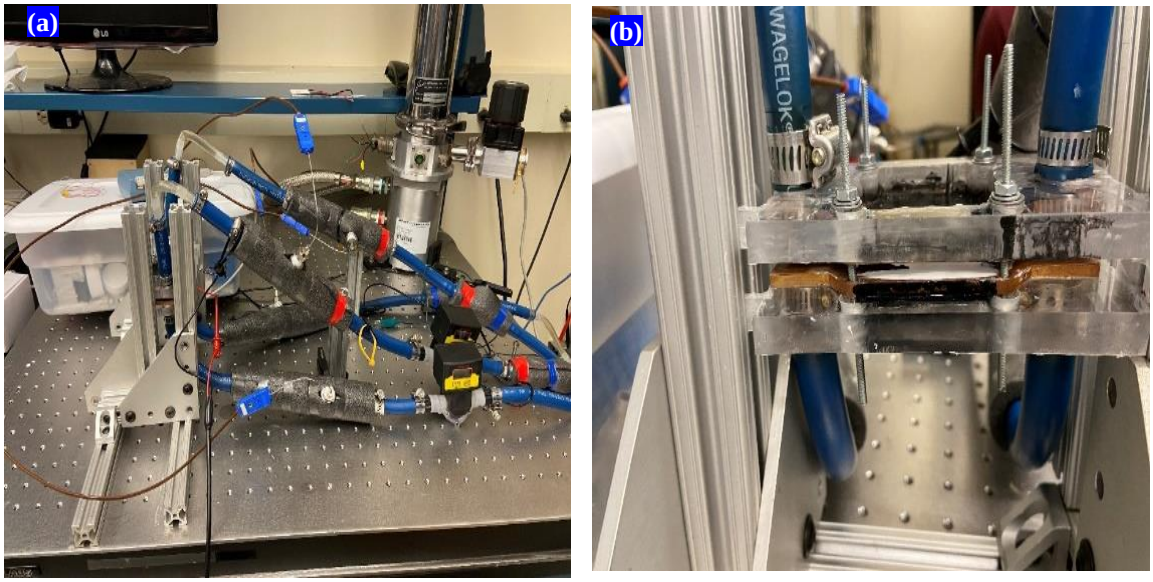

Figure 4.7 (a) overall view of test setup with two water flow controlled by chillers, (b) sample stage for TEG device

4.2.4 Results and Discussion

The chiller controls the temperature on the outside of TEG module. Due to the heat loss from heat reservoirs to cTEG module, the temperature on bottom and top sides of cTEG module drops. In order to better understand temperature range that on cTEG module, we use Finite Element Method (FEM) for temperature simulation.

Figure 4.8 shows the thermal model of cTEG with copper heat on top and bottom sides. The module contains 4 pairs of TE legs with a size of 1 mm x 1mm x 3.5 mm. The uniform heat transfer coefficient is set to 240 W/m^2K and mean water temperature T_{m_hot}=53.3 ˚C and T_{m_cold}=6.7 ˚C. The result shows a uniform distribution of heat on the substrate and the temperature drops from hot to cold side.

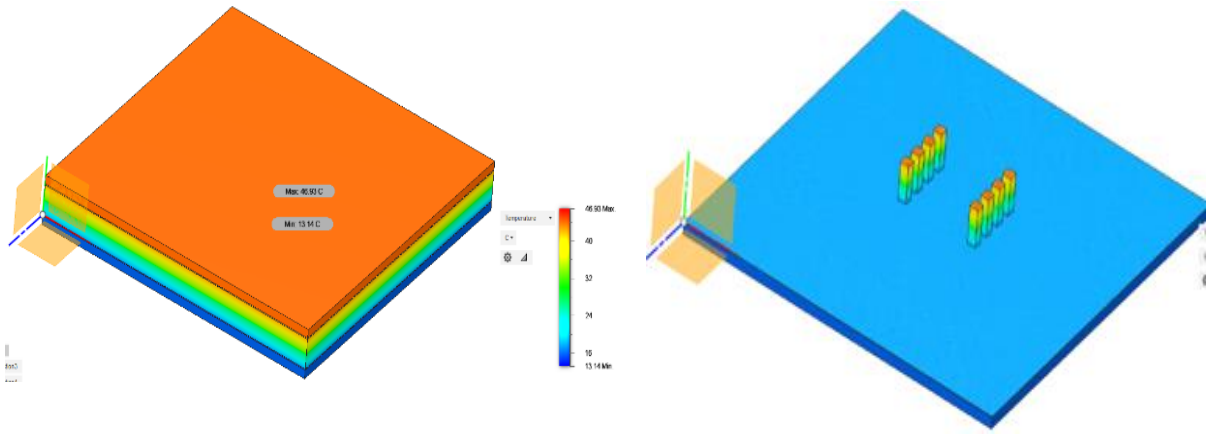

Figure 4.8 FEM simulation for temperature profile for cTEG with copper heat channels on top and bottom sides. Left: Full assembly thermal results with 4 pairs of Bi_2Te_3 legs (1 mm x 1mm x 3.5 mm) in the module. Right: Tempeature profile excluding PDMS gas filler and top (hot) side substrate

As we discussed in previous session on electro-thermal co-optimization of TEG device, it is necessary to match the load resistance with internal resistance of the TEG module. The initial measured internal resistance of the cTEG at room temperature was 77Ω. It was mainly attributed by resistance of printed metal contact and silver paste. As previously discussed, the optimum power output can be achieved when the load resistance matches to the internal resistance with the electro-thermal interaction factor $\sqrt{1+zT}$. In the experiment, the optimum load resistance can be found by manually change the load resistance under the stable heat flow across the device.

The power output *w* at the load resistor is defined as[168]:

$$w = \frac{R_L}{(R_L + R_{int})^2} {V_{oc}}^2 \qquad 4.6$$

where V_{oc} is the open circuit voltage from the TE module. Figure 4.9 shows the measured power output of the cTEG for ΔT=5˚C against various load resistances. The power output of the cTEG increases with the load resistance increases. As the load resistance is near the internal resistance of cTEG, the power output reaches maximum value and then decreases when the load resistance is larger than internal resistance. This corresponds to the simulation results discussed in section 4.1. Thus, a series of experiment was repeatedly conducted for obtaining optimum power output

by changing load resistance. At ΔT=5˚C, the optimized load resistance is found as 56.6Ω. The measured internal resistance at same temperature difference for TE module is 60.1Ω.

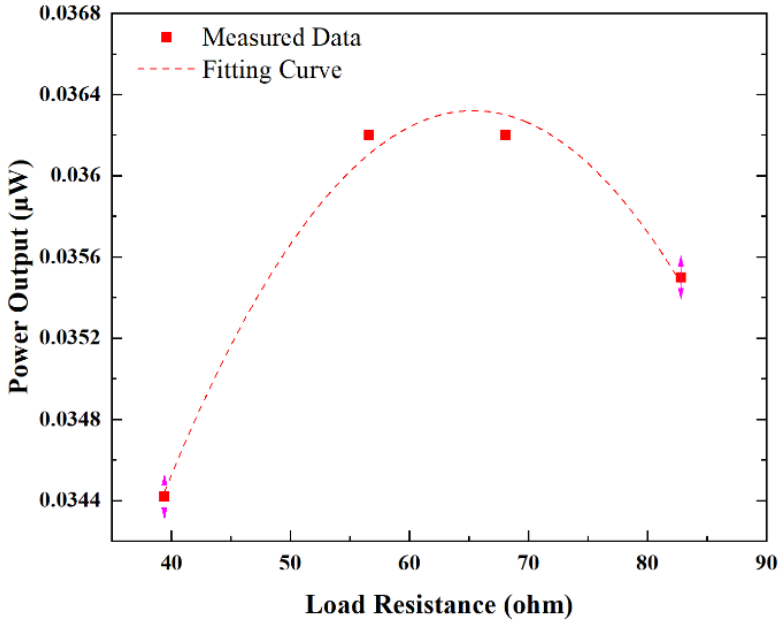

Figure 4.9 Power output vs load resistance at ΔT=5˚C.

Figure 4.10 shows the measured load voltage and power output of cTEG against the temperature difference between the top and bottom sides of the cTEG. The maximum power output at the matched load resistance were measured at various values of ΔT. The power output of TE module increases with the increase of ΔT, and the power output value was 2.02 μW at ΔT =50˚C. Compared to another work[113], the maximum power output density was 1.26 mW/m^2 at ΔT=50 ˚C, as shown in Figure 4.10 (b). At low temperature difference, the power output density is similar between this study and another one. However, we only use 4 pairs of TE legs compared 16 TE legs from another study. Theoretically, the more TE legs we pack in the module, the better power output and voltage will be achieved at certain range of the fill factor.

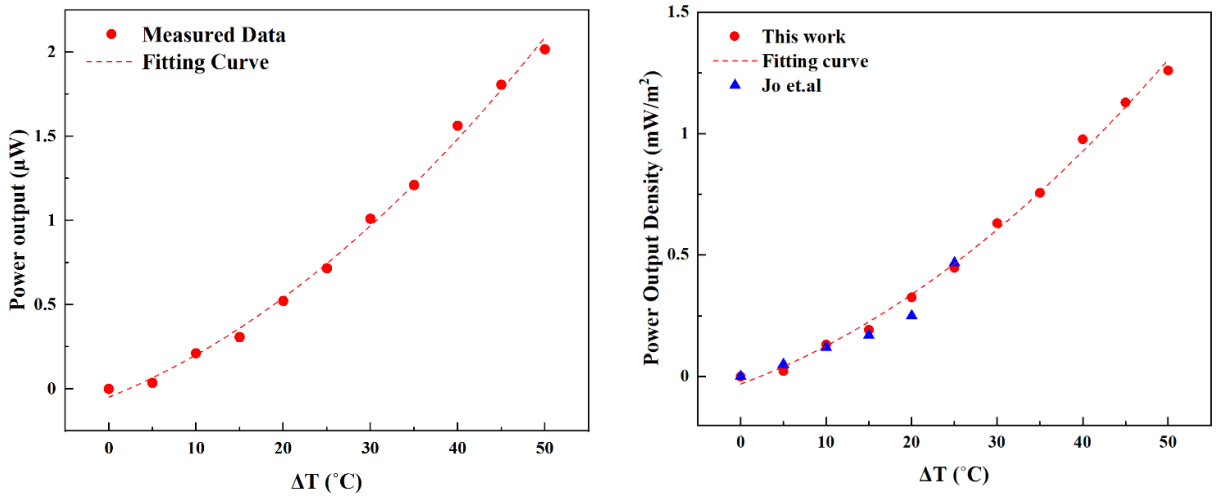

Figure 4.10 (a) Power output vs temperature difference for cTEG module with 4 pairs TE legs in a Cold side is fixed to 5˚C. (b) Comparison of power output density vs temperature difference.

The load voltage is also an important parameter to examine for device performance. Using cTEG for powering sensors needs to meet the voltage requirement for electronics that can boost up for powering. In order to compare the load voltage with expected load voltage $V_{load,exp}$ as represent:

$$V_{load,exp} = m/(1+m) \times N_{leg} \times (S \times \Delta T) \qquad 4.7$$

where $m = \sqrt{1+zT}$ is the ratio of load resistance with internal resistance, N_{leg} is the number of TE elements, ΔT is the temperature across the cTEG module. Figure 4.11 shows the relationship between measured load voltage and expected load voltage. The simulation results are perfectly matched with experimental results. The fitting curve shows linear function with R^2=99.86%, which indicates the measured load voltage is obtained at optimum load resistance at each temperature range. The maximum load voltage is reached at 32mW at 50˚C. To meet the voltage requirement for electronic devices, cTEG can connect with a DC-DC booster as a reliable power source.

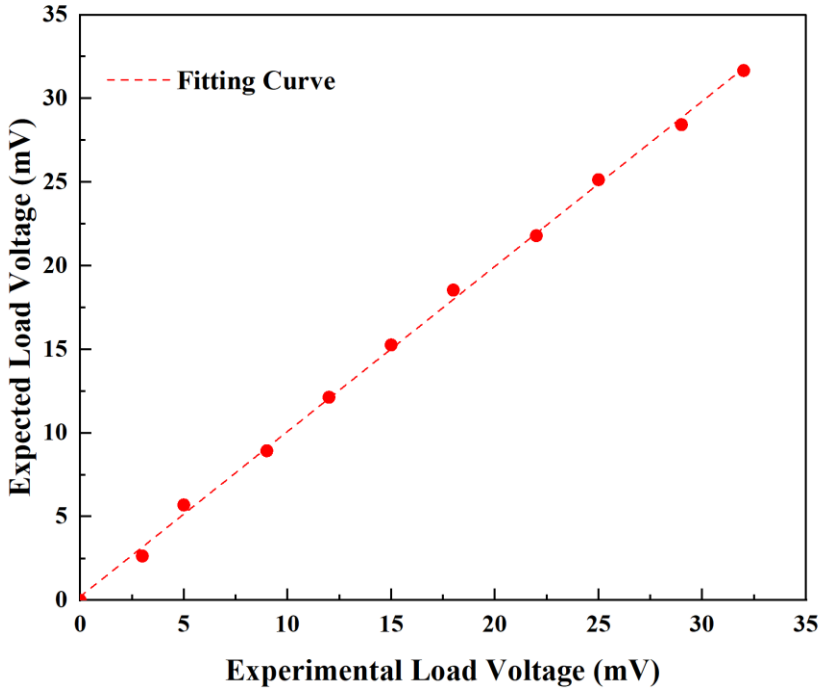

Figure 4.11 Experimental results vs simulation results on load voltage

4.2.5 Conclusions

In this session, a novel roll-to-roll cTEG device fabrication method is proposed. The proposed cTEG comprises TE materials that are inserted in to a PDMS film. The cTEG can be scalable fabricated using roll-to-roll production combined with printing technology. The prototype development is based on the electro-thermal co-optimization results for fill factor and leg thickness. A 4 pairs of the TE legs (1mm×1mm ×3.5mm) on a 40mm × 40mm ×4mm Kapton substrate is produced. The comparison between simulation results and experimental results both on thermal and electrical properties of cTEG. The device generated a maximum power output of 2.02 μW at ΔT =50˚C. The experimental load voltage is perfectly fitted simulated results that reached a 32mV at ΔT =50˚C. The preliminary results of cTEG prototype shows a promising trend for using roll-to-roll production of cTEG as energy sources for powering sensors.

5. SUMMARY AND FUTURE WORK

5.1 Summary of Current work

This thesis has systematically investigated the TE properties of oxides materials and the feasibility of fabricating cTEG on a roll-to-roll platform for powering IoT sensors and their related applications in civil infrastructure. The major research activities have focused on oxides TE materials synthesis (particularly $CuAlO_2$ and $PdBi_2O_4$) and structure-process-property analysis, cTEG device design, and manufacturing methods. We have been trying to answer the question: Is oxide-based TE technology suitable as energy sources for powering IoT sensors in civil infrastructure? This question has answered positivity through a combined theoretical and experimental study of cTEG devices at both materials and device levels.

This study contains two major parts started with synthesis and analysis of oxides TE materials in Chapter 3. The $CuAlO_2$ and $PdBi_2O_4$ based materials have been systematically studied with regards to their structural, electrical, and thermal properties. The aim was to fill the existing knowledge gap of oxide based TE materials and try to expand the TE materials beyond conventionally bismuth telluride-based materials, which are toxic and expensive. The oxides nanomaterials were synthesized using a standard solid-state method. The preliminary results indicated the $CuAlO_2$ and $PdBi_2O_4$ can be promising candidates for TE applications due to their high Seebeck coefficient and low thermal conductivity. However, it is essential to enhance their low electrical conductivity to further increase their zT value. In the existing literature, the studies on transport properties and TE behaviors have still not been addressed thoroughly; and thus, detailed work needs to be taken in these areas. $CuAlO_2$ and $PdBi_2O_4$ show high Seebeck coefficient as the band structure is relatively flat indicating larger density of state effective mass. On the other hand, through the study on process-structure-property relations, $CuAlO_2$ and $PdBi_2O_4$ show low thermal conductivity due to natural layered structure. This structure increases phonon scattering that could cause low thermal conductivity as of 0.776 W/mK at 773K for $CuAl_{0.8}Fe_{0.2}O_2$. Therefore, it is critical to use proper material synthesis techniques with an optimized annealing process and cold pressing to control the particle size in nanoscale. However, due to the natural localizations of holes, the p-type conduction of oxides is very low that causes low electrical conductivity of $CuAlO_2$. In order to enhance their electrical conductivity, the key is to increase

carrier concentration or mobility. Due to the inter-dependence among Seebeck coefficient, electrical and thermal conductivity, high carrier concentration often causes high electrical conductivity, low Seebeck coefficient, and high thermal conductivity. Therefore, a systematical study to discover new strategies of enhancing TE properties of $CuAlO_2$ and $PdBi_2O_4$ is needed. The temperature dependent TE properties also needs to be explored in order to obtain further study on electron and phonon transport. To achieve this goal, this study has utilized a generalized b-factor simulation approach to optimize the TE properties of $CuAlO_2$ and $PdBi_2O_4$ and guide the experimental process. It provided a clear direction on the enhancement of TE properties for current undoped oxides materials. Based on b-factor results, the optimum fermi level should range between 0.55 kT and 0.65 kT above the valence band edge for $CuAlO_2$. To achieve optimum power factor, the optimized carrier concentration was kept at 9.75×10^{16} cm^{-3} at room temperature. In order to further enhance the TE properties of $CuAlO_2$, Fe was selected as an effective dopant to increase electrical conductivity while decrease thermal conductivity. The highest zT value 1.2×10^{-2} was attained for $CuAl_{0.8}Fe_{0.2}O_2$ at 750K. The small zT is predominately due to the low electrical conductivity. Compared to other materials, $CuAl_{0.8}Fe_{0.2}O_2$ still shows the promises of being using as p-type TE material with low cost and earth abundant elements.

This research also investigated cTEG device design and fabrication process in Chapter 4. The conventional TEG fabrication method is mostly designed as rigid device for flat surfaces. However, lots of applications call for TEG with planar surfaces. The underground pipeline monitoring system and human body are just few examples of many. As such, there is a strong need for developing low cost and high durability cTEG with a scalable production process. This study has proposed a novel roll-to-roll fabrication process using unconventional method and printing technique for cTEG manufacturing. The final goal of this study is to explore the potentials of using cTEG to power IoT sensors for underground pipeline monitoring system in civil infrastructure systems. The cTEG electro-thermal co-optimization results indicated the optimized fill factor is 7% with leg thickness set to be 5mm that provided the direction for prototype development. The feasibility of using cTEG device as energy sources for powering sensors was assessed by conducting a series of experiments from device design to prototype development. According to the results, the maximum power output for a cTEG with 4 pairs thermocouples in a 40×40 mm^2 was found to be 2.02 μW at $\Delta T = 50^{\circ}C$ with a load voltage is 32 mV. In contrast, the power output of comparable cTEG devices in current literatures were often reported in the order of nW scale.

The as-produced cTEG module can definitely work as an energy bank to power IoT sensors for underground pipeline monitoring and wearable electronics through a DC-DC booster.

The current work would pave the road for enabling TE technology as energy sources for IoT sensors in civil infrastructure. It also provides a potential solution to fabricate cTEG in a large scale using cost-effective method and eco-friendly materials, such as $CuAlO_2$.

5.2 Future Work

Using TEG device for energy harvesting in civil infrastructure applications is in its infancy, there is still a long way to achieve engineering applications in the real world. The current study has developed a cTEG prototype to proof of concept, and there is a need for further study on large-scale device fabrication. Developing a cost-effective manufacturing method by roll-to-roll production will open up more opportunities to enable TE technology as power sources for IoT sensors. Also, the efficiency of TEG device is still lower than other conventional heat recovery methods, such as heat engines with Rankine cycle, and Brayton cycle etc. It is important to point out that the performance of heat sinks and heat exchangers plays an important role for improving overall TEG system efficiency. As TE technology is a customized technique for different applications, it takes more efforts and time to design and fabricate the device in order to satisfy each requirement. To this end, artificial intelligent (AI) technology can help to determine optimized conditions for TE technology by using big data analysis. For example, AI technology can choose the suitable TE materials and design for specific applications for different heat flow and temperature conditions. AI technology can also assist the device fabrication process to save labors and time. More importantly, TE technology is not only limited to be used as power sources, it can also be used as sensors for monitoring environmental conditions (temperature sensors, gas sensors, etc). With AI-guided design and fabrication process, TE technology may play a critical role in many applications, including energy harvesting and environmental sensing for civil engineering field.

REFERENCES

[1] Y. Feng *et al.*, "Metal oxides for thermoelectric power generation and beyond," *Adv. Compos. Hybrid Mater.*, vol. 1, no. 1, pp. 114–126, Mar. 2018, doi: 10.1007/s42114-017-0011-4.

[2] T. M. Tritt, "Thermoelectric Phenomena, Materials, and Applications," *Annu. Rev. Mater. Res.*, vol. 41, no. 1, pp. 433–448, Aug. 2011, doi: 10.1146/annurev-matsci-062910-100453.

[3] C. Zhou *et al.*, "Review-The Current and Emerging Applications of the III-Nitrides," *ECS J. Solid State Sci. Technol.*, vol. 6, no. 12, pp. 149–156, 2017, doi: 10.1149/2.

[4] H. Alam and S. Ramakrishna, "A review on the enhancement of figure of merit from bulk to nano-thermoelectric materials," *Nano Energy*, vol. 2, no. 2, pp. 190–212, Mar. 2013, doi: 10.1016/J.NANOEN.2012.10.005.

[5] M. Hamid Elsheikh *et al.*, "A review on thermoelectric renewable energy: Principle parameters that affect their performance," *Renew. Sustain. Energy Rev.*, vol. 30, pp. 337–355, Feb. 2014, doi: 10.1016/J.RSER.2013.10.027.

[6] A. Shakouri and J. Baskin, "Recent Developments in Semiconductor Thermoelectric Physics and Materials," *Annu. Rev. Mater. Res*, vol. 41, pp. 399–431, 2011, doi: 10.1146/annurev-matsci-062910-100445.

[7] C. S. Kim *et al.*, "Structural design of a flexible thermoelectric power generator for wearable applications," *Appl. Energy*, vol. 214, no. January, pp. 131–138, 2018, doi: 10.1016/j.apenergy.2018.01.074.

[8] Y. Yang, X.-J. Wei, and J. Liu, "Suitability of a thermoelectric power generator for implantable medical electronic devices," *J. Phys. D. Appl. Phys.*, vol. 40, no. 18, pp. 5790–5800, Sep. 2007, doi: 10.1088/0022-3727/40/18/042.

[9] L. Liu, "Feasibility of large-scale power plants based on thermoelectric effects," *New J. Phys.*, vol. 16, no. 12, p. 123019, Dec. 2014, doi: 10.1088/1367-2630/16/12/123019.

[10] M. S. Dresselhaus *et al.*, "New Directions for Low-Dimensional Thermoelectric Materials," *Adv. Mater.*, vol. 19, no. 8, pp. 1043–1053, Apr. 2007, doi: 10.1002/adma.200600527.

[11] Y. Takagiwa, Y. Pei, G. Pomrehn, and G. J. Snyder, “Dopants effect on the band structure of PbTe thermoelectric material,” *Appl. Phys. Lett.*, vol. 101, no. 9, p. 092102, Aug. 2012, doi: 10.1063/1.4748363.

[12] D. M. Rowe and V. S. Shukla, “The effect of phonon-grain boundary scattering on the lattice thermal conductivity and thermoelectric conversion efficiency of heavily doped fine-grained, hot-pressed silicon germanium alloy,” *J. Appl. Phys.*, vol. 52, no. 12, pp. 7421–7426, Dec. 1981, doi: 10.1063/1.328733.

[13] A. J. Minnich, M. S. Dresselhaus, Z. F. Ren, and G. Chen, “Bulk nanostructured thermoelectric materials: current research and future prospects,” *Energy Environ. Sci.*, vol. 2, no. 5, p. 466, May 2009, doi: 10.1039/b822664b.

[14] W. Liu, X. Yan, G. Chen, and Z. Ren, “Recent advances in thermoelectric nanocomposites,” *Nano Energy*, vol. 1, no. 1, pp. 42–56, Jan. 2012, doi: 10.1016/J.NANOEN.2011.10.001.

[15] Q. Hao, D. Xu, N. Lu, and H. Zhao, “High-throughput Z T predictions of nanoporous bulk materials as next-generation thermoelectric materials: A material genome approach,” *Phys. Rev. B*, vol. 93, no. 20, p. 205206, May 2016, doi: 10.1103/PhysRevB.93.205206.

[16] E. N. Hurwitz *et al.*, “Thermopower Study of GaN-Based Materials for Next-Generation Thermoelectric Devices and Applications,” *J. Electron. Mater.*, vol. 40, no. 5, pp. 513–517, May 2011, doi: 10.1007/s11664-010-1416-9.

[17] N. Lu and I. Ferguson, “III-nitrides for energy production: photovoltaic and thermoelectric applications,” *Semicond. Sci. Technol.*, vol. 28, no. 7, p. 074023, Jul. 2013, doi: 10.1088/0268-1242/28/7/074023.

[18] A. J. Minnich, M. S. Dresselhaus, Z. F. Ren, and G. Chen, “Bulk nanostructured thermoelectric materials: current research and future prospects,” *Energy Environ. Sci.*, vol. 2, no. 5, p. 466, May 2009, doi: 10.1039/b822664b.

[19] K. Rubenis, S. Populoh, P. Thiel, S. Yoon, U. Müller, and J. Locs, “Thermoelectric properties of dense Sb-doped SnO2ceramics,” *J. Alloys Compd.*, vol. 692, pp. 515–521, 2017, doi: 10.1016/j.jallcom.2016.09.062.

[20] T. M. Tritt and M. A. Subramanian, “Thermoelectric Materials, Phenomena, and Applications: A Bird’s Eye View,” *MRS Bull.*, vol. 31, no. 03, pp. 188–198, Mar. 2006, doi: 10.1557/mrs2006.44.

[21] G. S. Nolas, M. Kaeser, R. T. Littleton, and T. M. Tritt, “High figure of merit in partially filled ytterbium skutterudite materials,” *Appl. Phys. Lett.*, vol. 77, no. 12, p. 1855, Sep. 2000, doi: 10.1063/1.1311597.

[22] K. Koumoto, Y. Wang, R. Zhang, A. Kosuga, and R. Funahashi, “Oxide Thermoelectric Materials: A Nanostructuring Approach,” *Annu. Rev. Mater. Res.*, vol. 40, no. 1, pp. 363–394, Jun. 2010, doi: 10.1146/annurev-matsci-070909-104521.

[23] Y. Pei, X. Shi, A. LaLonde, H. Wang, L. Chen, and G. J. Snyder, “Convergence of electronic bands for high performance bulk thermoelectrics,” *Nature*, vol. 473, no. 7345, pp. 66–69, May 2011, doi: 10.1038/nature09996.

[24] L. D. Hicks and M. S. Dresselhaus, “Thermoelectric figure of merit of a one-dimensional conductor,” *Phys. Rev. B*, vol. 47, no. 24, pp. 16631–16634, 1993, doi: 10.1103/PhysRevB.47.16631.

[25] F. P. Zhang, Q. M. Lu, and J. X. Zhang, “Synthesis and high temperature thermoelectric properties of BaxAgyCa3−x−yCo4O9 compounds,” *J. Alloys Compd.*, vol. 484, no. 1–2, pp. 550–554, Sep. 2009, doi: 10.1016/J.JALLCOM.2009.04.144.

[26] Q. Hao, D. Xu, N. Lu, and H. Zhao, “High-throughput ZT predictions of nanoporous bulk materials as next-generation thermoelectric materials: A material genome approach,” *Phys. Rev. B*, vol. 93, no. 20, p. 205206, May 2016, doi: 10.1103/PhysRevB.93.205206.

[27] Z. Guo, Y. Chen, and N. L. Lu, *Multifunctional nanocomposites for energy and environmental applications*. .

[28] Y. Feng *et al.*, “Metal oxides for thermoelectric power generation and beyond,” *Adv. Compos. Hybrid Mater.*, vol. 1, no. 1, pp. 114–126, Mar. 2018, doi: 10.1007/s42114-017-0011-4.

[29] B. Hussain, M. Y. Akhtar Raja, N. Lu, and I. Ferguson, “Applications and synthesis of zinc oxide: An emerging wide bandgap material,” in *2013 High Capacity Optical Networks and Emerging/Enabling Technologies*, Dec. 2013, pp. 88–93, doi: 10.1109/HONET.2013.6729763.

[30] P. Jood *et al.*, “Al-Doped Zinc Oxide Nanocomposites with Enhanced Thermoelectric Properties,” *Nano Lett.*, vol. 11, no. 10, pp. 4337–4342, Oct. 2011, doi: 10.1021/nl202439h.

[31] B. Hussain, B. Kucukgok, M. Y. A. Raja, B. Klein, N. Lu, and I. T. Ferguson, “Is ZnO as a univeral semiconductor material an oxymoron,” in *Oxide-based Materials and Devices V*, Mar. 2014, p. 898718, doi: 10.1117/12.2042926.

[32] B. Kucukgok, B. Wang, A. G. Melton, N. Lu, and I. T. Ferguson, “Comparison of thermoelectric properties of GaN and ZnO samples,” *Phys. status solidi*, vol. 11, no. 3–4, pp. 894–897, Feb. 2014, doi: 10.1002/pssc.201300538.

[33] K. H. Jung, K. Hyoung Lee, W. S. Seo, and S. M. Choi, “An enhancement of a thermoelectric power factor in a Ga-doped ZnO system: A chemical compression by enlarged Ga solubility,” *Appl. Phys. Lett.*, vol. 100, no. 25, pp. 1–5, 2012, doi: 10.1063/1.4729560.

[34] S. Teehan, H. Efstathiadis, and P. Haldar, “Enhanced power factor of Indium co-doped ZnO:Al thin films deposited by RF sputtering for high temperature thermoelectrics,” *J. Alloys Compd.*, vol. 509, no. 3, pp. 1094–1098, 2011, doi: 10.1016/j.jallcom.2010.10.004.

[35] N. Lu *et al.*, “A review of earth abundant ZnO-based materials for thermoelectric and photovoltaic applications,” in *Oxide-based Materials and Devices IX*, Feb. 2018, vol. 10533, p. 53, doi: 10.1117/12.2302467.

[36] S. Chappel and A. Zaban, “Nanoporous SnO 2 electrodes for dye-sensitized solar cells: improved cell performance by the synthesis of 18 nm SnO 2 colloids,” 2002. Accessed: Mar. 13, 2019. [Online]. Available: http://nathan.instras.com/documentDB/paper-170.pdf.

[37] P. OLIVI, E. C. PEREIRA, E. LONGO, J. A. VARELLA, and L. O. D. BULHOES, “Preparation and Characterization of A Dip-coated Sno2 Film For Transparent Electrodes For Transmissive Electrochromic Devices,” *J. Electrochem. Soc.*, vol. 140, no. 5, pp. L81---L82, 1993, doi: 10.1149/1.2221591.

[38] K. Sekizawa, H. Widjaja, S. Maeda, Y. Ozawa, and K. Eguchi, “Low temperature oxidation of methane over Pd/SnO2 catalyst,” *Appl. Catal. A Gen.*, vol. 200, no. 1–2, pp. 211–217, Aug. 2000, doi: 10.1016/S0926-860X(00)00634-7.

[39] P. R. Bueno *et al.*, “Investigation of the electrical properties of SnO 2 varistor system using impedance spectroscopy,” *Cit. J. Appl. Phys.*, vol. 84, p. 3700, 1998, doi: 10.1063/1.368587.

[40] E. R. Leite, I. T. Weber, E. Longo, and J. A. Varela, “A New Method to Control Particle Size and Particle Size Distribution of SnO2 Nanoparticles for Gas Sensor Applications,” *Adv. Mater.*, vol. 12, no. 13, pp. 965–968, Jun. 2000, doi: 10.1002/1521-4095(200006)12:13<965::AID-ADMA965>3.0.CO;2-7.

[41] K. Rubenis, S. Populoh, P. Thiel, S. Yoon, U. Müller, and J. Locs, “Thermoelectric properties of dense Sb-doped SnO2 ceramics,” *J. Alloys Compd.*, vol. 692, pp. 515–521, Jan. 2017, doi: 10.1016/J.JALLCOM.2016.09.062.

[42] S. Yanagiya, N. V Nong, J. Xu, M. Sonne, and N. Pryds, “Thermoelectric Properties of SnO2 Ceramics Doped with Sb and Zn,” *J. Electron. Mater.*, vol. 40, no. 5, pp. 674–677, 2011, doi: 10.1007/s11664-010-1506-8.

[43] S. Yanagiya, N. V Nong, M. Sonne, and N. Pryds, “Thermoelectric properties of SnO 2-based ceramics doped with Nd, Hf or Bi,” vol. 1449, p. 327, 2012, doi: 10.1063/1.4731563.

[44] T. Tsubota, S. Kobayashi, N. Murakami, and T. Ohno, “Improvement of thermoelectric performance for Sb-doped SnO2 ceramics material by addition of Cu as sintering additive,” *J. Electron. Mater.*, vol. 43, no. 9, pp. 3567–3573, 2014, doi: 10.1007/s11664-014-3227-x.

[45] T. Tsubota, T. Ohno, N. Shiraishi, and Y. Miyazaki, “Thermoelectric properties of Sn1-x-yTiySbxO2 ceramics,” *J. Alloys Compd.*, vol. 463, no. 1–2, pp. 288–293, 2008, doi: 10.1016/j.jallcom.2007.09.001.

[46] D. Bérardan, E. Guilmeau, A. Maignan, and B. Raveau, “In2O3:Ge, a promising n-type thermoelectric oxide composite,” *Solid State Commun.*, vol. 146, no. 1–2, pp. 97–101, Apr. 2008, doi: 10.1016/J.SSC.2007.12.033.

[47] M. F. A. M. van Hest, M. S. Dabney, and J. D. Perkins, “High-mobility molybdenum doped indium oxide,” *Thin Solid Films*, vol. 496, no. 1, pp. 70–74, Feb. 2006, doi: 10.1016/J.TSF.2005.08.314.

[48] Y. Meng *et al.*, “A new transparent conductive thin film In2O3 : Mo.,” *Thin Solid Films*, vol. 394, no. 1–2, pp. 218–222, Aug. 2001, doi: 10.1016/S0040-6090(01)01142-7.

[49] T. Koida and M. Kondo, “Comparative studies of transparent conductive Ti-, Zr-, and Sn-doped In2O3 using a combinatorial approach,” *J. Appl. Phys.*, vol. 101, no. 6, p. 063713, Mar. 2007, doi: 10.1063/1.2712161.

[50] M. F. A. M. van Hest, M. S. Dabney, J. D. Perkins, D. S. Ginley, and M. P. Taylor, "Titanium-doped indium oxide: A high-mobility transparent conductor," *Appl. Phys. Lett.*, vol. 87, no. 3, p. 032111, Jul. 2005, doi: 10.1063/1.1995957.

[51] X. Li, Q. Zhang, W. Miao, L. Huang, and Z. Zhang, "Transparent conductive oxide thin films of tungsten-doped indium oxide," *Thin Solid Films*, vol. 515, no. 4, pp. 2471–2474, Dec. 2006, doi: 10.1016/J.TSF.2006.07.014.

[52] J. Lan, Y.-H. Lin, Y. Liu, S. Xu, and C.-W. Nan, "High Thermoelectric Performance of Nanostructured In2O3-Based Ceramics," *J. Am. Ceram. Soc.*, vol. 95, no. 8, pp. 2465–2469, Aug. 2012, doi: 10.1111/j.1551-2916.2012.05284.x.

[53] Y. Liu *et al.*, "Effect of Transition-Metal Cobalt Doping on the Thermoelectric Performance of In2O3 Ceramics," *J. Am. Ceram. Soc.*, vol. 93, no. 10, pp. 2938–2941, Oct. 2010, doi: 10.1111/j.1551-2916.2010.03904.x.

[54] Y. Liu, W. Xu, D.-B. Liu, M. Yu, Y.-H. Lin, and C.-W. Nan, "Enhanced thermoelectric properties of Ga-doped In_2O_3 ceramics via synergistic band gap engineering and phonon suppression," *Phys. Chem. Chem. Phys.*, vol. 17, no. 17, pp. 11229–11233, Apr. 2015, doi: 10.1039/C5CP00739A.

[55] K. Koumoto *et al.*, "Thermoelectric Ceramics for Energy Harvesting," *J. Am. Ceram. Soc.*, vol. 96, no. 1, pp. 1–23, Jan. 2013, doi: 10.1111/jace.12076.

[56] A. Nag and V. Shubha, "Oxide Thermoelectric Materials: A Structure–Property Relationship," *J. Electron. Mater.*, vol. 43, no. 4, pp. 962–977, Apr. 2014, doi: 10.1007/s11664-014-3024-6.

[57] M. Ahrens, R. Merkle, B. Rahmati, and J. Maier, "Effective masses of electrons in n-type SrTiO3 determined from low-temperature specific heat capacities," *Phys. B Condens. Matter*, vol. 393, no. 1–2, pp. 239–248, Apr. 2007, doi: 10.1016/J.PHYSB.2007.01.008.

[58] A. Mehdizadeh Dehkordi *et al.*, "Large Thermoelectric Power Factor in Pr-Doped $SrTiO_{3-\delta}$ Ceramics via Grain-Boundary-Induced Mobility Enhancement," *Chem. Mater.*, vol. 26, no. 7, pp. 2478–2485, Apr. 2014, doi: 10.1021/cm4040853.

[59] S. Ohta, T. Nomura, H. Ohta, and K. Koumoto, "High-temperature carrier transport and thermoelectric properties of heavily La- Or Nb-doped SrTiO 3 single crystals," *J. Appl. Phys.*, vol. 97, no. 3, p. 034106, Feb. 2005, doi: 10.1063/1.1847723.

[60] T. Okuda, K. Nakanishi, S. Miyasaka, and Y. Tokura, “Large thermoelectric response of metallic perovskites: Sr 1 − x La x TiO 3 (0 <~ x <~ 0 . 1),” *Phys. Rev. B*, vol. 63, no. 11, p. 113104, Mar. 2001, doi: 10.1103/PhysRevB.63.113104.

[61] S. Walia *et al.*, “Transition metal oxides – Thermoelectric properties,” *Prog. Mater. Sci.*, vol. 58, no. 8, pp. 1443–1489, Oct. 2013, doi: 10.1016/J.PMATSCI.2013.06.003.

[62] H. Ohta, “Thermoelectrics based on strontium titanate,” *Mater. Today*, vol. 10, no. 10, pp. 44–49, Oct. 2007, doi: 10.1016/S1369-7021(07)70244-4.

[63] S. Sr, R. X. Tio, L. Zhang, T. Tosho, N. Okinaka, and T. Akiyama, “Thermoelectric Properties of Combustion Synthesized and Spark Plasma,” *Mater. Trans.*, vol. 48, no. 8, pp. 2088–2093, 2007, doi: 10.2320/matertrans.E-MRA2007836.

[64] H. C. Wang *et al.*, “Doping Effect of La and Dy on the Thermoelectric Properties of SrTiO3,” *J. Am. Ceram. Soc.*, vol. 94, no. 3, pp. 838–842, Mar. 2011, doi: 10.1111/j.1551-2916.2010.04185.x.

[65] I. Terasaki, Y. Sasago, and K. Uchinokura, “Large thermoelectric power in NaCo 2O4 single crystals,” *Phys. Rev. B*, vol. 56, no. 20, pp. R12685–R12687, Nov. 1997, doi: 10.1103/PhysRevB.56.R12685.

[66] X. C. Tong, *Advanced materials for thermal management of electronic packaging*. Springer, 2011.

[67] M. Lee *et al.*, “Large enhancement of the thermopower in Na x CoO2 at high Na doping,” *Nat. Mater.*, vol. 5, no. 7, pp. 537–540, Jul. 2006, doi: 10.1038/nmat1669.

[68] N. Li, Y. Jiang, G. Li, C. Wang, J. Shi, and D. Yu, “Self-ignition route to Ag-doped Na1.7Co2O4 and its thermoelectric properties,” *J. Alloys Compd.*, vol. 467, no. 1–2, pp. 444–449, Jan. 2009, doi: 10.1016/J.JALLCOM.2007.12.012.

[69] A. Bhaskar, C.-J. Liu, J. J. Yuan, and C.-L. Chang, “Thermoelectric properties of n-type Ca1−xBixMn1−ySiyO3−δ (x=y=0.00, 0.02, 0.03, 0.04, and 0.05) system,” *J. Alloys Compd.*, vol. 552, pp. 236–239, Mar. 2013, doi: 10.1016/j.jallcom.2012.10.078.

[70] G. Xu, R. Funahashi, M. Shikano, I. Matsubara, and Y. Zhou, “Thermoelectric properties of the Bi- and Na-substituted Ca3Co4O9 system,” *Appl. Phys. Lett.*, vol. 80, no. 20, pp. 3760–3762, May 2002, doi: 10.1063/1.1480115.

[71] R. Tian *et al.*, “Ga Substitution and Oxygen Diffusion Kinetics in $Ca_3Co_4O_{9+\delta}$ -Based Thermoelectric Oxides,” *J. Phys. Chem. C*, vol. 117, no. 26, pp. 13382–13387, Jul. 2013, doi: 10.1021/jp403592s.

[72] A. Bhaskar, Z.-R. Yang, and C.-J. Liu, “High temperature thermoelectric properties of co-doped Ca3−xAgxCo3.95Fe0.05O9+δ (0≤x≤0.3),” *Ceram. Int.*, vol. 41, no. 9, pp. 10456–10460, Nov. 2015, doi: 10.1016/j.ceramint.2015.04.121.

[73] Y. Wang, Y. Sui, J. Cheng, X. Wang, and W. Su, “The thermal-transport properties of the $Ca_{3-x}Ag_xCo_4O_9$ system ($0 \leq x \leq 0.3$),” *J. Phys. Condens. Matter*, vol. 19, no. 35, p. 356216, Sep. 2007, doi: 10.1088/0953-8984/19/35/356216.

[74] H. Ohta, K. Sugiura, and K. Koumoto, “Recent Progress in Oxide Thermoelectric Materials: p-Type $Ca_3Co_4O_9$ and n-Type $SrTiO_3$,” *Inorg. Chem.*, vol. 47, no. 19, pp. 8429–8436, Oct. 2008, doi: 10.1021/ic800644x.

[75] N. Van, N.; Liu, and C.-J.; Ohtaki, “Improvement on the High temperature Thermoelectric Performance of Ga-doped Misfit-layered Ca3Co4-xGaxO9+ (x = 0, 0.05, 0.1, and 0.2),” *J. Alloys Compd.*, vol. 491, pp. 53–56, 2018, doi: 10.1016/j.jallcom.2009.11.009.

[76] Y. Wang, Y. Sui, X. Wang, W. Su, and X. Liu, “Enhanced high temperature thermoelectric characteristics of transition metals doped Ca3Co4O9+δ by cold high-pressure fabrication,” *J. Appl. Phys.*, vol. 107, no. 3, p. 033708, Feb. 2010, doi: 10.1063/1.3291125.

[77] T. Tsubota, M. Ohtaki, K. Eguchi, and H. Arai, “Thermoelectric properties of Al-doped ZnO as a promising oxide material for high-temperature thermoelectric conversion,” *J. Mater. Chem.*, vol. 7, no. 1, pp. 85–90, Jan. 1997, doi: 10.1039/a602506d.

[78] M. Ohtaki, K. Araki, and K. Yamamoto, “High thermoelectric performance of dually doped ZnO ceramics,” in *Journal of Electronic Materials*, Jul. 2009, vol. 38, no. 7, pp. 1234–1238, doi: 10.1007/s11664-009-0816-1.

[79] K. Park, H. K. Hwang, J. W. Seo, and W. S. Seo, “Enhanced high-temperature thermoelectric properties of Ce- and Dy-doped ZnO for power generation,” *Energy*, vol. 54, pp. 139–145, Jun. 2013, doi: 10.1016/j.energy.2013.03.023.

[80] T. Tsubota, T. Ohno, N. Shiraishi, and Y. Miyazaki, “Thermoelectric properties of Sn1−x−yTiySbxO2 ceramics,” *J. Alloys Compd.*, vol. 463, no. 1–2, pp. 288–293, Sep. 2008, doi: 10.1016/J.JALLCOM.2007.09.001.

[81] S. Yanagiya, N. V. Nong, M. Sonne, and N. Pryds, “Thermoelectric properties of SnO2-based ceramics doped with Nd, Hf or Bi,” in *AIP Conference Proceedings*, Jun. 2012, vol. 1449, no. 1, pp. 327–330, doi: 10.1063/1.4731563.

[82] Y. Liu, W. Xu, D. B. Liu, M. Yu, Y. H. Lin, and C. W. Nan, “Enhanced thermoelectric properties of Ga-doped In2O3 ceramics via synergistic band gap engineering and phonon suppression,” *Phys. Chem. Chem. Phys.*, vol. 17, no. 17, pp. 11229–11233, May 2015, doi: 10.1039/c5cp00739a.

[83] T. Nagira, M. Ito, S. Katsuyama, K. Majima, and H. Nagai, “Thermoelectric properties of (Na1−yMy)xCo2O4 (M=K, Sr, Y, Nd, Sm and Yb; y=0.01∼0.35),” *J. Alloys Compd.*, vol. 348, no. 1–2, pp. 263–269, Jan. 2003, doi: 10.1016/S0925-8388(02)00799-5.

[84] M. Ito and D. Furumoto, “Microstructure and thermoelectric properties of NaxCo2O4/Ag composite synthesized by the polymerized complex method,” *J. Alloys Compd.*, vol. 450, no. 1–2, pp. 517–520, Feb. 2008, doi: 10.1016/J.JALLCOM.2006.12.081.

[85] J. Y. Cho *et al.*, “Effect of Trivalent Bi Doping on the Seebeck Coefficient and Electrical Resistivity of Ca3Co4O9,” *J. Electron. Mater.*, vol. 44, no. 10, pp. 3621–3626, Oct. 2015, doi: 10.1007/s11664-015-3924-0.

[86] N. V. Nong, C. J. Liu, and M. Ohtaki, “Improvement on the high temperature thermoelectric performance of Ga-doped misfit-layered Ca3Co4-xGaxO9+δ (x = 0, 0.05, 0.1, and 0.2),” *J. Alloys Compd.*, vol. 491, no. 1–2, pp. 53–56, Feb. 2010, doi: 10.1016/j.jallcom.2009.11.009.

[87] N. Okinaka, L. Zhang, and T. Akiyama, “Thermoelectric properties of rare earth-doped SrTiO3 using combination of combustion synthesis (CS) and spark plasma sintering (SPS),” *ISIJ Int.*, vol. 50, no. 9, pp. 1300–1304, 2010, doi: 10.2355/isijinternational.50.1300.

[88] H. C. Wang *et al.*, “Doping Effect of La and Dy on the Thermoelectric Properties of SrTiO3,” *J. Am. Ceram. Soc.*, vol. 94, no. 3, pp. 838–842, Mar. 2011, doi: 10.1111/j.1551-2916.2010.04185.x.

[89] W. Glatz, E. Schwyter, L. Durrer, and C. Hierold, “Bi2Te3-based flexible micro thermoelectric generator with optimized design,” *J. Microelectromechanical Syst.*, vol. 18, no. 3, pp. 763–772, 2009, doi: 10.1109/JMEMS.2009.2021104.

[90] W. Qu, M. Plötner, and W. J. Fischer, “Microfabrication of thermoelectric generators on flexible foil substrates as a power source for autonomous microsystems,” *J. Micromechanics Microengineering*, vol. 11, no. 2, pp. 146–152, Mar. 2001, doi: 10.1088/0960-1317/11/2/310.

[91] S. Hasebe, J. Ogawa, T. Toriyama, S. Sugiyama, H. Ueno, and K. Itoigawa, “Design and fabrication of flexible thermopile for power generation,” in *MHS 2003 - Proceedings of 2003 International Symposium on Micromechatronics and Human Science*, 2003, pp. 287–291, doi: 10.1109/MHS.2003.1249950.

[92] K. Itoigawa, H. Ueno, M. Shiozaki, T. Toriyama, and S. Sugiyama, “Fabrication of flexible thermopile generator,” *J. Micromechanics Microengineering*, vol. 15, no. 9, p. S233, Sep. 2005, doi: 10.1088/0960-1317/15/9/S10.

[93] M. Takashiri, T. Shirakawa, K. Miyazaki, and H. Tsukamoto, “Fabrication and characterization of bismuth-telluride-based alloy thin film thermoelectric generators by flash evaporation method,” *Sensors Actuators, A Phys.*, vol. 138, no. 2, pp. 329–334, Aug. 2007, doi: 10.1016/j.sna.2007.05.030.

[94] A. Yadav, K. P. Pipe, and M. Shtein, “Fiber-based flexible thermoelectric power generator,” *J. Power Sources*, vol. 175, no. 2, pp. 909–913, Jan. 2008, doi: 10.1016/j.jpowsour.2007.09.096.

[95] E. Schwyter, W. Glatz, L. Durrer, and C. Hierold, “Flexible micro thermoelectric generator based on electroplated B1 2+xTe3-x,” in *DTIP of MEMS and MOEMS - Symposium on Design, Test, Integration and Packaging of MEMS/MOEMS*, 2008, pp. 46–48, doi: 10.1109/DTIP.2008.4752949.

[96] S. Khan, R. S. Dahiya, and L. Lorenzelli, “Flexible thermoelectric generator based on transfer printed Si microwires,” in *European Solid-State Device Research Conference*, Nov. 2014, pp. 86–89, doi: 10.1109/ESSDERC.2014.6948764.

[97] C. C. Hsiao and Y. S. Wu, “Fabrication of flexible thin-film thermoelectric generators,” *J. Chinese Inst. Eng. Trans. Chinese Inst. Eng. A*, vol. 34, no. 6, pp. 809–816, 2011, doi: 10.1080/02533839.2011.591552.

[98] G. Delaizir *et al.*, "A new generation of high performance large-scale and flexible thermo-generators based on (Bi,Sb) 2 (Te,Se) 3 nano-powders using the Spark Plasma Sintering technique," *Sensors Actuators, A Phys.*, vol. 174, no. 1, pp. 115–122, Feb. 2012, doi: 10.1016/j.sna.2011.11.011.

[99] Y. Yang, Z. H. Lin, T. Hou, F. Zhang, and Z. L. Wang, "Nanowire-composite based flexible thermoelectric nanogenerators and self-powered temperature sensors," *Nano Res.*, vol. 5, no. 12, pp. 888–895, Nov. 2012, doi: 10.1007/s12274-012-0272-8.

[100] H. Im, H. G. Moon, J. S. Lee, I. Y. Chung, T. J. Kang, and Y. H. Kim, "Flexible thermocells for utilization of body heat," *Nano Res.*, vol. 7, no. 4, pp. 1–10, Jan. 2014, doi: 10.1007/s12274-014-0410-6.

[101] K. Suemori, Y. Watanabe, and S. Hoshino, "Carbon nanotube bundles/polystyrene composites as high-performance flexible thermoelectric materials," *Appl. Phys. Lett.*, vol. 106, no. 11, p. 113902, Mar. 2015, doi: 10.1063/1.4915622.

[102] L. Francioso *et al.*, "Thin film technology flexible thermoelectric generator and dedicated ASIC for energy harvesting applications," in *Proceedings of the 2013 5th IEEE International Workshop on Advances in Sensors and Interfaces, IWASI 2013*, 2013, pp. 104–107, doi: 10.1109/IWASI.2013.6576100.

[103] G. A. T. Sevilla, S. Bin Inayat, J. P. Rojas, A. M. Hussain, and M. M. Hussain, "Flexible and Semi-Transparent Thermoelectric Energy Harvesters from Low Cost Bulk Silicon (100)," *Small*, vol. 9, no. 23, pp. 3916–3921, Dec. 2013, doi: 10.1002/smll.201301025.

[104] P. Fan *et al.*, "Low-cost flexible thin film thermoelectric generator on zinc based thermoelectric materials," *Appl. Phys. Lett.*, vol. 106, no. 7, p. 073901, Feb. 2015, doi: 10.1063/1.4909531.

[105] C. Navone, M. Soulier, M. Plissonnier, and A. L. Seiler, "Development of (Bi,Sb) 2(Te,Se) 3-based thermoelectric modules by a screen-printing process," *J. Electron. Mater.*, vol. 39, no. 9, pp. 1755–1759, Sep. 2010, doi: 10.1007/s11664-010-1187-3.

[106] H. B. Lee, J. H. We, H. J. Yang, K. Kim, K. C. Choi, and B. J. Cho, "Thermoelectric properties of screen-printed ZnSb film," *Thin Solid Films*, vol. 519, no. 16, pp. 5441–5443, Jun. 2011, doi: 10.1016/j.tsf.2011.03.031.

[107] Z. Cao, E. Koukharenko, M. J. Tudor, R. N. Torah, and S. P. Beeby, “Screen printed flexible Bi2Te3-Sb2Te 3 based thermoelectric generator,” in *Journal of Physics: Conference Series*, Dec. 2013, vol. 476, no. 1, p. 012031, doi: 10.1088/1742-6596/476/1/012031.

[108] Z. Cao, E. Koukharenko, R. N. Torah, J. Tudor, and S. P. Beeby, “Flexible screen printed thick film thermoelectric generator with reduced material resistivity,” in *Journal of Physics: Conference Series*, Nov. 2014, vol. 557, no. 1, p. 012016, doi: 10.1088/1742-6596/557/1/012016.

[109] S. J. Kim, J. H. We, and B. J. Cho, “A wearable thermoelectric generator fabricated on a glass fabric,” *Energy Environ. Sci.*, vol. 7, no. 6, pp. 1959–1965, May 2014, doi: 10.1039/c4ee00242c.

[110] M. K. Kim, M. S. Kim, S. E. Jo, H. L. Kim, S. M. Lee, and Y. J. Kim, “Wearable thermoelectric generator for human clothing applications,” in *2013 Transducers and Eurosensors XXVII: The 17th International Conference on Solid-State Sensors, Actuators and Microsystems, TRANSDUCERS and EUROSENSORS 2013*, 2013, pp. 1376–1379, doi: 10.1109/Transducers.2013.6627034.

[111] M. K. Kim, M. S. Kim, S. Lee, C. Kim, and Y. J. Kim, “Wearable thermoelectric generator for harvesting human body heat energy,” *Smart Mater. Struct.*, vol. 23, no. 10, p. 105002, Oct. 2014, doi: 10.1088/0964-1726/23/10/105002.

[112] D. Madan, Z. Wang, A. Chen, P. K. Wright, and J. W. Evans, “High-performance dispenser printed MA p-type Bi0.5Sb 1.5Te3 flexible thermoelectric generators for powering wireless sensor networks,” *ACS Appl. Mater. Interfaces*, vol. 5, no. 22, pp. 11872–11876, Nov. 2013, doi: 10.1021/am403568t.

[113] S. E. Jo, M. K. Kim, M. S. Kim, and Y. J. Kim, “Flexible thermoelectric generator for human body heat energy harvesting,” *Electron. Lett.*, vol. 48, no. 16, pp. 1015–1017, Aug. 2012, doi: 10.1049/el.2012.1566.

[114] Z. Lu *et al.*, “Fabrication of flexible thermoelectric thin film devices by inkjet printing,” *Small*, vol. 10, no. 17. Wiley-VCH Verlag, pp. 3551–3554, Sep. 10, 2014, doi: 10.1002/smll.201303126.

[115] F. Jiao, C. -a. Di, Y. Sun, P. Sheng, W. Xu, and D. Zhu, “Inkjet-printed flexible organic thin-film thermoelectric devices based on p- and n-type poly(metal 1,1,2,2-ethenetetrathiolate)s/polymer composites through ball-milling,” *Philos. Trans. R. Soc. A Math. Phys. Eng. Sci.*, vol. 372, no. 2013, pp. 20130008–20130008, Mar. 2014, doi: 10.1098/rsta.2013.0008.

[116] A. Besganz, V. Zöllmer, R. Kun, E. Pál, L. Walder, and M. Busse, “Inkjet Printing as a Flexible Technology for the Deposition of Thermoelectric Composite Structures,” *Procedia Technol.*, vol. 15, pp. 99–106, Jan. 2014, doi: 10.1016/j.protcy.2014.09.043.

[117] O. Bubnova *et al.*, “Optimization of the thermoelectric figure of merit in the conducting polymer poly(3,4-ethylenedioxythiophene),” *Nat. Mater.*, vol. 10, no. 6, pp. 429–433, May 2011, doi: 10.1038/nmat3012.

[118] Z. Cao, E. Koukharenko, M. J. Tudor, R. N. Torah, and S. P. Beeby, “Flexible screen printed thermoelectric generator with enhanced processes and materials,” *Sensors Actuators A Phys.*, vol. 238, pp. 196–206, Feb. 2016, doi: 10.1016/J.SNA.2015.12.016.

[119] Z. Cao, E. Koukharenko, M. J. Tudor, R. N. Torah, and S. P. Beeby, “Flexible screen printed thermoelectric generator with enhanced processes and materials,” *Sensors Actuators, A Phys.*, vol. 238, pp. 196–206, Feb. 2016, doi: 10.1016/j.sna.2015.12.016.

[120] S. J. Kim, J. H. We, J. S. Kim, G. S. Kim, and B. J. Cho, “Thermoelectric properties of P-type Sb2Te3 thick film processed by a screen-printing technique and a subsequent annealing process,” *J. Alloys Compd.*, vol. 582, pp. 177–180, Jan. 2014, doi: 10.1016/j.jallcom.2013.07.195.

[121] J. H. We, S. J. Kim, G. S. Kim, and B. J. Cho, “Improvement of thermoelectric properties of screen-printed Bi 2Te3 thick film by optimization of the annealing process,” *J. Alloys Compd.*, vol. 552, pp. 107–110, Mar. 2013, doi: 10.1016/j.jallcom.2012.10.085.

[122] R. Rudež, P. Markowski, M. Presečnik, M. Košir, A. Dziedzic, and S. Bernik, “Development of thick-film thermoelectric microgenerators based on p-type Ca3Co4O9 and n-type (ZnO)5In2O3 legs,” *Ceram. Int.*, vol. 41, no. 10, pp. 13201–13209, Dec. 2015, doi: 10.1016/j.ceramint.2015.07.097.

[123] O. A. Basaran, H. Gao, and P. P. Bhat, “Nonstandard Inkjets,” 2012, doi: 10.1146/annurev-fluid-120710-101148.

[124] L. J. Hoong, Y. C. Keat, A. Chik, and T. P. Leng, “Band structure and thermoelectric properties of inkjet printed ZnO and ZnFe2O4 thin films,” *Ceram. Int.*, vol. 42, no. 10, pp. 12064–12073, Aug. 2016, doi: 10.1016/j.ceramint.2016.04.135.

[125] A. Chen, D. Madan, P. K. Wright, and J. W. Evans, “Dispenser-printed planar thick-film thermoelectric energy generators,” *J. Micromechanics Microengineering*, vol. 21, no. 10, p. 104006, Oct. 2011, doi: 10.1088/0960-1317/21/10/104006.

[126] J. A. Lewis, “Direct ink writing of 3D functional materials,” *Adv. Funct. Mater.*, vol. 16, no. 17, pp. 2193–2204, Nov. 2006, doi: 10.1002/adfm.200600434.

[127] A. Chen, D. Madan, M. Koplow, P. K. Wright, and J. W. Evans, “DISPENSER PRINTED THERMOELECTRIC ENERGY GENERATORS,” in *PowerMEMS*, Dec. 2009, p. 277.

[128] Y. J. Kim *et al.*, “High-performance self-powered wireless sensor node driven by a flexible thermoelectric generator,” *Energy*, vol. 162, pp. 526–533, Nov. 2018, doi: 10.1016/j.energy.2018.08.064.

[129] B. Iezzi, K. Ankireddy, J. Twiddy, M. D. Losego, and J. S. Jur, “Printed, metallic thermoelectric generators integrated with pipe insulation for powering wireless sensors,” *Appl. Energy*, vol. 208, pp. 758–765, Dec. 2017, doi: 10.1016/j.apenergy.2017.09.073.

[130] H. Kawazoe, M. Yasukawa, H. Hyodo, M. Kurita, H. Yanagi, and H. Hosono, “P-type electrical conduction in transparent thin films of CuAlO2,” *Nature*, vol. 389, no. 6654, pp. 939–942, Oct. 1997, doi: 10.1038/40087.

[131] R. Gillen and J. Robertson, “Band structure calculations of CuAlO 2 , CuGaO 2 , CuInO 2 , and CuCrO 2 by screened exchange,” *Phys. Rev. B*, vol. 84, no. 3, p. 035125, Jul. 2011, doi: 10.1103/PhysRevB.84.035125.

[132] T. Ishiguro, A. Kitazawa, N. Mizutani, and M. Kato, “Single-crystal growth and crystal structure refinement of CuAlO2,” *J. Solid State Chem.*, vol. 40, no. 2, pp. 170–174, Nov. 1981, doi: 10.1016/0022-4596(81)90377-7.

[133] L. D. Hicks and M. S. Dresselhaus, “Use of Quantum-Well Superlattices to Obtain a High Figure of Merit from Nonconventional Thermoelectric Materials,” *MRS Proc.*, vol. 326, p. 413, Jan. 1993, doi: 10.1557/PROC-326-413.

[134] K. Koumoto, Y. Wang, R. Zhang, A. Kosuga, and R. Funahashi, “Oxide Thermoelectric Materials: A Nanostructuring Approach,” *Annu. Rev. Mater. Res.*, vol. 40, no. 1, pp. 363–394, Jun. 2010, doi: 10.1146/annurev-matsci-070909-104521.

[135] T. C. Harman, P. J. Taylor, M. P. Walsh, and B. E. LaForge, “Quantum dot superlattice thermoelectric materials and devices.,” *Science*, vol. 297, no. 5590, pp. 2229–32, Sep. 2002, doi: 10.1126/science.1072886.

[136] N. Lu and S. Oza, “Thermal stability and thermo-mechanical properties of hemp-high density polyethylene composites: Effect of two different chemical modifications,” *Compos. Part B Eng.*, vol. 44, no. 1, pp. 484–490, Jan. 2013, doi: 10.1016/J.COMPOSITESB.2012.03.024.

[137] B. Hussain, M. Y. Akhtar Raja, N. Lu, and I. Ferguson, “Applications and synthesis of zinc oxide: An emerging wide bandgap material,” in *2013 High Capacity Optical Networks and Emerging/Enabling Technologies*, Dec. 2013, pp. 88–93, doi: 10.1109/HONET.2013.6729763.

[138] N. Lu *et al.*, “A review of earth abundant ZnO-based materials for thermoelectric and photovoltaic applications,” in *Oxide-based Materials and Devices IX*, Feb. 2018, vol. 10533, p. 53, doi: 10.1117/12.2302467.

[139] Y. Lu, T. Nozue, N. Feng, K. Sagara, H. Yoshida, and Y. Jin, “Fabrication of thermoelectric CuAlO2 and performance enhancement by high density,” *J. Alloys Compd.*, vol. 650, pp. 558–563, Nov. 2015, doi: 10.1016/J.JALLCOM.2015.08.013.

[140] M. S. Dresselhaus *et al.*, “New Directions for Low-Dimensional Thermoelectric Materials,” *Adv. Mater.*, vol. 19, no. 8, pp. 1043–1053, Apr. 2007, doi: 10.1002/adma.200600527.

[141] K. H. L. Zhang, K. Xi, M. G. Blamire, and R. G. Egdell, “*P* -type transparent conducting oxides,” *J. Phys. Condens. Matter*, vol. 28, no. 38, p. 383002, Sep. 2016, doi: 10.1088/0953-8984/28/38/383002.

[142] S. F. Wang and Y. F. Hsu, “Electrical conductivity and thermal expansion coefficient of internal phases occurring in multilayer ceramic structures,” *Ceram. Int.*, vol. 26, no. 6, pp. 669–671, Jul. 2000, doi: 10.1016/S0272-8842(00)00002-X.

[143] N. Bettahar, P. Conflant, J. C. Boivin, F. Abraham, and D. Thomas, “Electrical conductivity of (Bi,Pb)2MO4 (M = Pd,Pt) linear chain compounds,” *J. Phys. Chem. Solids*, vol. 46, no. 3, pp. 297–299, Jan. 1985, doi: 10.1016/0022-3697(85)90169-6.

[144] J. He, S. Hao, Y. Xia, S. S. Naghavi, V. Ozoliņš, and C. Wolverton, "Bi_2PdO_4: A Promising Thermoelectric Oxide with High Power Factor and Low Lattice Thermal Conductivity," *Chem. Mater.*, vol. 29, no. 6, pp. 2529–2534, Mar. 2017, doi: 10.1021/acs.chemmater.6b04230.

[145] K. Fujita, T. Mochida, and K. Nakamura, "High-Temperature Thermoelectric Properties of $Na_xCoO_{2-\delta}$ Single Crystals," *Jpn. J. Appl. Phys.*, vol. 40, no. Part 1, No. 7, pp. 4644–4647, Jul. 2001, doi: 10.1143/JJAP.40.4644.

[146] N. Bettahar, P. Conflant, J. C. Boivin, F. Abraham, and D. Thomas, "ELECTRICAL CONDUCTIVITY OF (Bi,PbhM04 (M = Pd,Pt) LINEAR CHAIN COMPOUNDS," 1985. Accessed: Mar. 18, 2019. [Online]. Available: https://ac.els-cdn.com/0022369785901696/1-s2.0-0022369785901696-main.pdf?_tid=57b3991a-74de-4418-a25e 79fd182131e9&acdnat=1552944455_3b5c6dd2e04c804cba68977d642eccb6.

[147] E. Witkoske, X. Wang, J. Maassen, and M. Lundstrom, "Universal behavior of the thermoelectric fi gure of merit , zT , vs . quality factor," *Mater. Today Phys.*, vol. 8, pp. 43–48, 2019, doi: 10.1016/j.mtphys.2018.12.005.

[148] E. Witkoske, X. Wang, M. Lundstrom, V. Askarpour, and J. Maassen, "Thermoelectric band engineering: The role of carrier scattering," *J. Appl. Phys.*, vol. 122, no. 175102, 2017, doi: 10.1063/1.4994696.

[149] Q. Xu, Y. Li, L. Zhang, W. Zheng, D. J. Singh, and Y. Ma, "Sn(II)-containing phosphates as optoelectronic materials," 2016. Accessed: Mar. 19, 2019. [Online]. Available: https://arxiv.org/pdf/1612.01372.pdf.

[150] E. Witkoske, Z. Tong, Y. Feng, X. Ruan, M. Lundstrom, and N. Lu, "The use of strain and grain boundaries to tailor phonon transport properties: A first-principles study of 2H-phase CuAlO2. II," *J. Appl. Phys.*, vol. 127, no. 11, p. 115108, Mar. 2020, doi: 10.1063/1.5142485.

[151] N. Daichakomphu, R. Sakdanuphab, A. Harnwunggmoung, Y. Puarporn, N. Chanlek, and A. Sakulkalavek, "Enhanced carrier concentration of Fe doped delafossite CuAlO2 by double-effect: Divalent metal ions doping and excess oxygen," *Solid State Ionics*, vol. 328, pp. 17–24, Dec. 2018, doi: 10.1016/j.ssi.2018.11.007.

[152] H. Wang, A. D. LaLonde, Y. Pei, and G. J. Snyder, “The Criteria for Beneficial Disorder in Thermoelectric Solid Solutions,” *Adv. Funct. Mater.*, vol. 23, no. 12, pp. 1586–1596, Mar. 2013, doi: 10.1002/adfm.201201576.

[153] Z. Liu *et al.*, “Co-doping of magnesium with indium in nitrides: first principle calculation and experiment,” *RSC Adv.*, vol. 6, no. 6, pp. 5111–5115, Jan. 2016, doi: 10.1039/C5RA24642C.

[154] C. Liu and D. T. Morelli, “Thermoelectric Properties of Hot-Pressed and PECS-Sintered Magnesium-Doped Copper Aluminum Oxide,” *J. Electron. Mater.*, vol. 40, no. 5, pp. 678–681, May 2011, doi: 10.1007/s11664-011-1508-1.

[155] S. Pantian, R. Sakdanuphab, and A. Sakulkalavek, “Enhancing the electrical conductivity and thermoelectric figure of merit of the p-type delafossite CuAlO2 by Ag2O addition,” *Curr. Appl. Phys.*, vol. 17, no. 10, pp. 1264–1270, Oct. 2017, doi: 10.1016/j.cap.2017.06.011.

[156] K. Park, K. Y. Ko, and W. S. Seo, “Effect of partial substitution of Ca for Al on the microstructure and high-temperature thermoelectric properties of CuAlO2,” *Mater. Sci. Eng. B Solid-State Mater. Adv. Technol.*, vol. 129, no. 1–3, pp. 1–7, Apr. 2006, doi: 10.1016/j.mseb.2005.10.035.

[157] D. O. Scanlon, A. Walsh, B. J. Morgan, G. W. Watson, D. J. Payne, and R. G. Egdell, “Effect of Cr substitution on the electronic structure of CuAl 1-xCrxO2,” *Phys. Rev. B - Condens. Matter Mater. Phys.*, vol. 79, no. 3, p. 035101, Jan. 2009, doi: 10.1103/PhysRevB.79.035101.

[158] S. Yanagiya, N. Van Nong, J. Xu, and N. Pryds, “The Effect of (Ag, Ni, Zn)-Addition on the Thermoelectric Properties of Copper Aluminate,” *Materials (Basel).*, vol. 3, no. 1, pp. 318–328, Jan. 2010, doi: 10.3390/ma3010318.

[159] K. Park, K. Y. Ko, H. C. Kwon, and S. Nahm, “Improvement in thermoelectric properties of CuAlO2 by adding Fe2O3,” *J. Alloys Compd.*, vol. 437, no. 1–2, pp. 1–6, Jun. 2007, doi: 10.1016/j.jallcom.2006.07.067.

[160] Y. C. Liou, L. S. Chang, Y. M. Lu, H. C. Tsai, and U. R. Lee, “Effects of mechanical milling on preparation and properties of CuAl 1-xFe xO 2 thermoelectric ceramics,” *Ceram. Int.*, vol. 38, no. 5, pp. 3619–3624, Jul. 2012, doi: 10.1016/j.ceramint.2011.12.079.

[161] D. Huang, J. Lin, M. J. Nilges, and Y. Pan, “Local structures and roles of Fe3+ and Cr3+ in p-type semiconductor CuAlO2,” *Phys. status solidi*, vol. 249, no. 8, pp. 1559–1565, Aug. 2012, doi: 10.1002/pssb.201147466.

[162] V. Siriwongrungson, A. Sakulkalavek, and R. Sakdanuphab, “Optimum sintering temperature for thermoelectric properties of low-cost CuAl0.90Fe0.10O2 material,” *J. Mater. Sci. Mater. Electron.*, vol. 27, no. 10, pp. 11102–11109, Oct. 2016, doi: 10.1007/s10854-016-5227-5.

[163] E. N. Hurwitz *et al.*, “Thermopower Study of GaN-Based Materials for Next-Generation Thermoelectric Devices and Applications,” *J. Electron. Mater.*, vol. 40, no. 5, pp. 513–517, May 2011, doi: 10.1007/s11664-010-1416-9.

[164] Y. Feng *et al.*, “Temperature dependent thermoelectric properties of cuprous delafossite oxides,” *Compos. Part B Eng.*, vol. 156, pp. 108–112, Jan. 2019, doi: 10.1016/j.compositesb.2018.08.070.

[165] D. M. Rowe and C. M. Bhandari, *CRC Handbook of Thermoelectrics*. Boca Raton: CRC Press, 1995.

[166] B. Poudel *et al.*, “High-Thermoelectric Performance of Nanostructured Bismuth Antimony Telluride Bulk Alloys,” *Science*, vol. 320, no. 5876, pp. 634–638, 2008.

[167] K. Yazawa and A. Shakouri, “Optimization of power and efficiency of thermoelectric devices with asymmetric thermal contacts,” *J. Appl. Phys.*, vol. 111, no. 2, p. 024509, Jan. 2012, doi: 10.1063/1.3679544.

[168] T. Yajima, K. Tanaka, and K. Yazawa, “Thermoelectric On-Spot Energy Harvesting for Diagnostics of Water Service Pipelines,” in *Proceedings of the 17th InterSociety Conference on Thermal and Thermomechanical Phenomena in Electronic Systems, ITherm 2018*, Jul. 2018, pp. 881–888, doi: 10.1109/ITHERM.2018.8419582.

[169] M. King, R. Shaw, and V. Badali, “PLANNING, DEVELOPMENT AND DELIVERY,” 2012. Accessed: Mar. 07, 2019. [Online]. Available: www.districtenergy.org.

[170] K. C. Kavvadias and S. Quoilin, “Exploiting waste heat potential by long distance heat transmission: Design considerations and techno-economic assessment,” *Appl. Energy*, vol. 216, pp. 452–465, Apr. 2018, doi: 10.1016/J.APENERGY.2018.02.080.

[171] S. LeBlanc, “Thermoelectric generators: Linking material properties and systems engineering for waste heat recovery applications,” *Sustain. Mater. Technol.*, vol. 1–2, pp. 26–35, Dec. 2014, doi: 10.1016/J.SUSMAT.2014.11.002.

[172] “New York Today: The Morning After a Steam Pipe Explosion - The New York Times.” https://www.nytimes.com/2018/07/20/nyregion/new-york-today-steam-pipe-explosion.html (accessed Mar. 15, 2019).

[173] “Baltimore steam pipe explosion damaged 33 vehicles, leaving frustrated car owners - Baltimore Sun.” https://www.baltimoresun.com/news/maryland/baltimore-city/bs-md-steam-pipe-clean-up-20170630-story.html (accessed Mar. 15, 2019).

[174] “Gas Distribution, Gas Gathering, Gas Transmission, Hazardous Liquids, Liquefied Natural Gas (LNG), and Underground Natural Gas Storage (UNGS) Annual Report Data | PHMSA.” https://www.phmsa.dot.gov/data-and-statistics/pipeline/gas-distribution-gas-gathering-gas-transmission-hazardous-liquids (accessed Mar. 07, 2019).

PUBLICATIONS

Book Chapter

1. E. Ghafari, **Y. Feng**, S.A. Ghahari, F. Severgnini, B. Kucukgok, I. Ferguson, and N. Lu "Chapter 9: Nanocomposites for Thermoelectricity", in Multifunctional Nanocomposites for Energy and Environmental Applications, ed. Z. Guo, Y. Chen and N. Lu, ISBN: 978-3-527-34213-6 Publisher: Wiley-VCH Inc.

Journal Publications (In preparation)

2. **Y. Feng**, J. Joo, N. Lu. "The Effects of Fe Addition for Enhanced Thermoelectric performance in p-type $CuAlO_2$", 2020.
3. **Y. Feng**, K. Yazawa, and N. Lu. "Thin-Film Conformal Energy Harvester for Powering IoT Sensors on Steam Pipelines", 2020. In preparation
4. E. Ghafari, **Y. Feng**, and N. Lu. "Core-shell Structured PVDF-Graphene Oxide with a Giant Piezoelectric Coefficient", Composites Part B: Engineering, 2020. Submitted

Journal Publications (Published)

5. E. Witkoske, Z. Tong, **Y. Feng**, X. Ruan, M. Lundstrom, and N. Lu. "The use of strain and grain boundaries to tailor phonon transport properties: A first principles study of 2H-phase $CuAlO_2$ (Part II)", Journal of Applied Physics, 127 (11), 115108, 2020.
6. **Y. Feng,** YF. Su, N. Lu, and S. Shah. "Meta Concrete: Exploring Novel Functionality of Concrete Using Nanotechnology", Engineered Science, 8, 01-10, 2019. (Featured as Cover Page for Dec 2019 Issue)
7. **Y. Feng**, V. Saravade, T. Chung, Y. Dong, H. Zhou, B. Kucukgok, I.T. Ferguson, and N. Lu, "Strain-Stress Study of AlxGa1-xN/AlN Heterostructures on c-Plane Sapphire and Related Optical Properties", Scientific Reports, 9, 10172, 2019.
8. **Y. Feng**, A. Elquist, Y. Zhang, K. Gao, I. Ferguson, A. Tzempelikos, and N. Lu, "Temperature Dependent Thermoelectric Properties of Cuprous Delafossite Oxides", Composites Part B: Engineering, 156, 108-112, 2019.
9. **Y. Feng**, X. Jiang, E. Ghafari, B. Kucukgok, C. Zhang, I. Ferguson, and N. Lu, "Metal Oxides for Thermoelectric Power Generation and Beyond", Advanced Composites and Hybrid Materials, 1 (1), 114-126, 2018.

10. **Y. Feng,** E. Witkoske, E. Bell, Y. Wang, A. Tzempelikos, I.T. Ferguson, and N. Lu, "Advanced Metal Oxides and Nitrites Thermoelectric Materials for Energy Harvesting" ES Materials & Manufacturing, 1, 13-20, 2018.
11. E. Witkoske, D. Guzman, **Y. Feng**, A. Strachan, M. Lundstrom, and N. Lu, "2H phase $CuAlO_2$ Thermoelectric Transport Properties from First Principles Band Structure Calculations", Journal of Applied Physics, 125, 082531, 2019.
12. E. Ghahari, **Y. Feng**, Y. Liu, I. Ferguson, and N. Lu, "Investigating Process-Structure Relations of ZnO nanofiber via Electrospinning Method", Composites Part B: Engineering, 116, pp 40-45, 2017.
13. Y. Liu, X. Jiang, **Y. Feng**, Z. Feng, I. Ferguson, and N. Lu, "Temperature-dependent Optical Properties of AlN Thin Films for High-Temperature Power Electronics", MRS advances, 2 (5), pp 323-328, 2017.
14. E. Ghafari, S.A. Ghahari, **Y. Feng**, F. Severgnini**,** and N. Lu**, "**Effect of nano Zinc Oxide and Al-Zinc oxide addition on the rheological properties of cement pastes" Composites part B: Engineering, 105, pp 160-166, 2016.
15. M. Idrees, S. Batool, J. Kong, Q. Zhuang, H. Liu, Q. Shao, N. Lu, **Y. Feng**, E. Wujcik, Q. Gao, T. Ding, R. Wei, and Z. Guo, "Polyborosilazane Derived Ceramics-Nitrogen Sulfur Dual Doped Graphene Nanocomposite Anode for Enhanced Lithium Ion Batteries", Electrochimica Acta, 296, 925-937, 2019.
16. Y. Ma, M. Ma, X. Yin, Q. Shao, N. Lu, **Y. Feng**, Y. Lu, E. Wujcik, X. Mai, C. Wang, and Z. Guo, " Tuning Polyaniline Nanostructures via End Group Substitutions and their Morphology Dependent Electrochemical Performances", Polymer, 156, 128-135, 2018.
17. J. Zhang, Y. Liang, X. Wang, H. Zhou, S. Li, J. Zhang, **Y. Feng**, N. Lu, Q. Wang, and Z. Guo, "Strengthened Epoxy Resin with Hyperbranched Polyamine-ester Anchored Graphene Oxide via Novel Phase Transfer Approach", Advanced Composites and Hybrid Materials, 1(2), 300-309, 2018.
18. C. Zhou, A. Ghods, V. G. Saravade, P. V. Patel, K. L. Yunghans, C. Ferguson, **Y. Feng**, B. Kucukgok, N. Lu, and I. Ferguson, "The Current and Emerging Applications of the III-Nitrites", ECS Journal of Solid State Science and Technology, 6(12), Q146-Q156, 2017.

Conference Proceedings

19. **Y. Feng**, and N. Lu, "Cuprous Delafossite Oxides for High Temperature Thermoelectric Application", The Proceeding of 2018 International Conference on Composites and Nano Engineering, 263-264, 2018.
20. C. Zhou, A. Ghods, V. G. Saravade, P. V. Patel, K. L. Yunghans, C. Ferguson, **Y. Feng**, X. Jiang, B. Kucukgok, N. Lu, and I. Ferguson, "(Invited) The III-Nitrides as a Universal Compound Semiconductor Material: A Review", ECS Transactions, 77(6), pp 3-21, 2017.

21. E. Ghafari, **Y. Feng**, S. A Ghahari, A. Bukowski, and N. Lu, "Investigating Process-Structure Relations of ZnO Nanofiber via Electrospinning Process for Piezoelectricity", the Proceeding of 2016 International Conference on Composites and Nano Engineering, pp. 355-356, 2016.

Technical Reports

22. N. Lu, T. Tzempelikos, Y. Feng, and J. Xiong, "Multifunctional Thermoelectric Facades for Power Generation (through Waste Heat Harvesting in Building Envelopes)." Technical report to Arconic Corporation, Lafayette, IN 47906. July 2018.

Proposal Written

Major contributions to NSF Partnerships for Innovation-Technology Transfer (PFI-TT) program proposal writing on title "Prototyping Thermoelectric Devices for Power Sensors in Pipeline Monitoring". Granted on June 3rd, 2019 IIP-1919191

Conference Presentations

23. **Y. Feng**, I. Ferguson, and N. Lu, "Nanostructured Oxides for Next Generation Thermoelectrics", 2020 SPIE Photonic West, San Francisco, CA, Feb 03-06, 2020. **(Invited Talk)**
24. K. Weideman, SD Deshmukh, **Y. Feng**, N. Lu, and R. Agrawal, "Facile Fabrication of Lead Chalcogenide Thin Films with Controlled Structure and Composition", 2019 AlChE Annual Meeting, Orlando, FL, Nov 10-15, 2019.
25. **Y. Feng**, Z. Bagban, and N. Lu, "Roll-to-Roll Fabrication of High Performance Conformal Thermoelectric Generators", 2018 Materials Research Society (MRS) Fall Technical Conference, Boston, MA, Nov 25- Nov 29, 2018.
26. **Y. Feng**, and N. Lu, "Cuprous Delafossite Oxide for High Temperature Thermoelectric Application", the 26th International Conference on Composites and Nano Engineering, Paris, France, July 15-21, 2018.
27. **Y. Feng**, and N. Lu, I. Ferguson, "ZnO Based Materials for Energy Harvesting: Thermoelectric and Photovoltaics", 2018 SPIE Photonic West, San Francisco, CA, Jan 29- Feb 02, 2018. **(Invited Talk)**
28. **Y. Feng**, I. Ferguson, and N. Lu, "Delafossite Oxides for High Temperature Thermoelectric Applications", 2017 Materials Research Society (MRS) Fall Technical Conference, Boston, MA, Nov 26- Dec. 1, 2017.
29. **Y. Feng**, S. Ghahari, E. Ghafari, and N. Lu, "Effects of Oxide Nanoparticles on Thermoelectric Behavior of Cement Composites for Energy Harvesting Applications", 2017 TRB Session 382-Nanotechnology, Washington DC, Jan 8 – 12, 2017. **(Invited Talk)**

30. E. Ghafari, S. Ghahari, **Y. Feng**, and N. Lu, "Nanomaterials for Energy Harvesting in Civil Infrastructures", Anna Maria Workshop XVII, Tampa, FL, Nov 16 – 18, 2016.
31. E. Ghafari, **Y. Feng**, S. A Ghahari, A. Bukowski, and N. Lu, "Investigating process-structure relations of ZnO nanofiber via electrospinning process for piezoelectricity", the 2016 International Conference on Composites and Nano Engineering, Haikou, China. July 18-22, 2016. **(Keynote Talk)**
32. E. Ghafari, S. A Ghahari, L. Castano, **Y. Feng**, and N. Lu, "Poster: Thermoelectric concrete for energy harvesting in civil infrastructures", the 7th Advances in Cement-Based Materials, Northwestern University, Evanston, Illinois. July 10-13, 2016.

Patents

33. "Bendable On-Site Thermo Energy Harvester", K. Yazawa, **Y. Feng**, N. Lu, Invention disclosure submitted on May 13, 2020.
34. "Roll to Roll Fabrication of High Performance Flexible Thermoelectric Generators", N. Lu, **Y. Feng**, Approved by PRF for Provisional Patent Filing, 2018-Lu-68096.
35. Patent No.CN103173882A, "Preparation Method of Graphene/ Silk Complex Fiber", CW. Song, JK. Xiao, **Y. Feng,** 2012.